Li-Induced Oxygen Activation in Li-Rich Materials for Designing High Energy Li-Ion Battery Systems

September 2019

LI XIANG

Li-Induced Oxygen Activation in Li-Rich Materials for Designing High Energy Li-Ion Battery Systems

Graduate School of Systems and Information Engineering

University of Tsukuba

September 2019

LI XIANG

ABSTRACT

Rechargeable lithium-ion batteries (LIBs) have high power density with long cycling life and robust structural stability. Consequently, lithium-ion batteries have obtained increasing widespread applications in our daily lives. As the energy storage devices, they are indispensable in the fields of portable devices, such as cellphone and laptop. The state-of-the-art positive electrodes, however, fail to meet our increasing demand for high capacity. For instance, typical layered cathodes $LiTMO_2$ (TM = transition metals) are restricted to the relatively low energy density (less than 200 mAh g^{-1}). These cathodes will not be able to meet the increasing requirements. Therefore, a lot of efforts have been made in improving the electrochemical performance of the current materials and searching for better electrode materials with high capacity and good cyclic ability. Herein, Li-rich layered materials attract widespread attention as the potential candidates, aiming to solve the capacity issues of the cathodes because of their beyond-capacity performance and property of cathodic and anionic redox mechanism. Being one embodiment, Li_2MnO_3 delivers a high standard of capacity (more than 400 mAh g^{-1}) in initial cycles, providing more possibility for large-capacity cathodes.

Insertion-extraction of Li-ions accounts for the charge-discharge processes for most conventional cathodes of Li-ion accompanied by the redox process of cationic transition metal. However, the mechanism based on cationic redox process is unable to explain the anomalous capacities exhibited by Li-rich materials because they can deliver excess capacity beyond the theoretical capacity based on cationic redox process. To explain this phenomenon, oxygen activation, then, has been proposed. Nevertheless, an in-depth understanding of the evolution of crystal and explicit oxygen behavior exhibited by Li-rich layered oxides is insufficient. Herein, to probe the relationship between structural evolution and detailed pathway of oxygen activation of Li-rich cathodes, a typical layered Li-rich material $Li_{1.2}Ni_{0.2}Mn_{0.6}O_2$ is investigated by various in situ technologies, as one representation. The reversible phenomenon of O^{-}–O^{-} (peroxo oxygen dimers) bonds forming mostly along the c-axis is directly visualized.

Additionally, the formation of the peroxo O^{-}–O^{-} bond is calculated *via* density functional theory, and the results coincide well with that of in situ Raman and X-ray diffraction (XRD). These findings enrich the understandings about oxygen activation in layered Li-rich oxides and pave a way to design high capacity positive electrodes with more reversible oxygen activations for lithium-ion batteries.

We know that layered Li-rich oxide cathodes are of prime importance for the development of high-energy lithium-ion batteries. The oxides, however, always suffer from detrimental phase transition, resulting in irreversible capacity fade and voltage fade. Li-rich cation-disordered rock-salt oxides are of firm structure and stable voltage output. Unfortunately, they usually exhibit sluggish kinetics and inferior cycling stability. Herein, a new rock-salt Li-rich oxide $Li_2Ni_{1/3}Ru_{2/3}O_3$ with Fd-3m space group, where partial cation-ordering arrangement exists in cationic sites, is reported. Results demonstrate that $Li_2Ni_{1/3}Ru_{2/3}O_3$ delivers a large capacity, outstanding rate capability as well as good cycling performance with negligible voltage decay, which is superior compared with common Li-rich layered oxides and cations disordered oxides with space group Fm-3m. Oxygen activation is also confirmed by first principle calculations. Moreover, the cathode owns good kinetics with more 0-TM percolation networks. In situ Raman results confirm the reversible oxygen activation as O^{2-}/O^{-} evolution during cycles in this type cathode for the first time.

Our findings highlight new evidence for the reversible anionic redox process in Li-rich cathode materials and provide a deep understanding of intercalation chemistry and new insights into the design of high-performance Li-rich layered oxides. Moreover, we enrich the field of view for Li-rich based cathodes and pave a new way to design the stable high rate performance materials with rock-salt structure for the next generation of Li-ion batteries.

TABLE OF CONTENTS

LIST OF FIGURES

LIST OF TABLES

Chapter 1. General introduction

1.1 Urgent demand for energy storage and applications of Li-ion batteries

Our varied life cannot exist without energy. Original energy requires a complicated process for energy conversion, energy storage and energy transfer until we can use in our home. Nature contains some inexhaustible resources which we can exploit from, such as solar energy converted from the sun, wind energy converted from the wind. [1-2] Then we should consider how to store the energy after converting. Thus, a storage device is indispensable to our home applications. Whenever we want to apply, the energy storage device will supply, as shown in **Figure 1.1**.

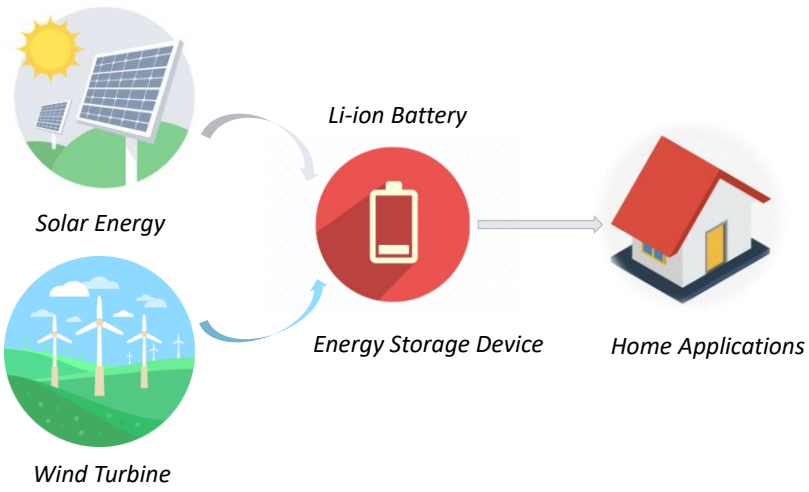

Figure 1. 1 Energy exploited from nature for home applications. Pictures are from www.google.com/imghp?hl=zh-cn.

Li-ion batteries are used widely in our electronic applications, as one kind of popular energy storage device, such as smartphone, portable computer, camera. These applications are common-used devices and have a wide variety in our daily lives, consisting an essential part for daily activities.[3] In addition, there are many other applications utilizing Li-ion batteries, telecommunications, electrical vehicles, railways,

space applications, etc., as shown in **Figure 1.2**, which will be simplify introduced in the following part.[4]

Figure 1. 2 Applications of Li-ion batteries [4]

As described above, solar and wind energy are well-known for energy conversion from nature, as renewable energy systems. However, the systems can only produce the energy without storage or accumulation of energy. That means we can utilize the energy from solar and wind for a short time. It, therefore, requires a stable and efficient device for storing the energy. A battery is needed. Compared with other battery technologies, Li-ion batteries own the properties of a highly efficient of quick charging process, a large energy density for long time use, a lighter weight for portable devices. With these reasons, Li-ion batteries are widely accepted in the field of energy storage combing a large scale of devices.

With the excessive consumption of petroleum, electrical vehicles are becoming a better alternative for the typical automobile as modern transportation.[5] Recent years,

many battery technologies are proposed for electric vehicles. Considering the properties of the electrical vehicles, which related to speed and distance, we need to adopt a new battery system. As it turned out, Li-ion battery are the batter choice. Recently, more and more automobile brands launched their electrical vehicles. Tesla is one representative employing $LiNi_{0.8}Co_{0.15}Al_{0.05}O_2$ (NCA) as cathode for Li-ion battery, having a powerful influence in the world. [6-7] And in China, BYD also has designed excellent electrical vehicles utilizing $LiFePO_4$ as cathode for Li-ion battery.[8]

Except for the vehicles, the subway is another essential public transport. As for subway and extended railways systems, they have a giant network of transportation crossing the cities and operations.[9] As a result, they require a large of energy storage and they may back up the data at any time. Meanwhile, the systems also need auxiliary power for any eventuality. Li-ion batteries own large power density and safety, which is the optimized option for energy storage and backup for this equipment with large networks and operations.

Similar to subways and railways with a vast supply system, telecommunications also possess enormous networks. With mobile phones being used on a large scale over the past decades, telecommunications gain remarkable growth. Almost everyone owns a mobile phone and the phone should work at any time we want. Thus, telecom companies should supply power at any time for a whole year with their equipment and systems, ensuring our normal requirement. So, it is important for them to possess a high-power storage device for support. Similarly, as mentioned characteristics of Li-ion batteries, telecommunications turn to lithium battery technology.[10]

Some applications should be operating in extreme conditions, like a harsh temperature environment. For instance, the transportation system in the area of equator and North Poles, the mining activities should be supplied steadily by stable and safe energy back up. Li-ion batteries are highly recommended for these applications because they are reliable and safe, and they are not restricted to operated temperature, which means they can be suitable even in extreme conditions.

For defense and military systems, they require a high level of accuracy and security more, such as radars and detection devices, etc.[11] Li-ion batteries are highly preferred for their safety, stability, high performance, long cycling life, etc., resulting in they are a suitable choice for a powerful energy back up.

We summarize some applications which require a satisfying battery technology. Then, we can conclude that the battery technologies should possess the properties of safety, stability, high rates performance and power density, long cycling life, etc., to match complicated situations. Thus, Lithium-ion batteries have a very prospective and they are the optimized option.

1.2 Li-ion batteries for large energy storage

1.2.1 Comparison of Li-ion batteries with other batteries

Besides Li-ion batteries, there are other rechargeable battery technologies: lead-acid battery, nickel-cadmium (Ni-Cd) battery, and nickel-metal hydride (NiMH) battery.

Lead-acid battery was invented by Gaston Planté et al. and then commercialized for practical use in 1859.[12] The battery is the earliest application of battery technology, which is common in an electric bicycle. The battery produces less pollution with low cost and well recyclability. However, the capacity is unsatisfactory which means the battery should have large weight and large volume if we want more capacity. It is inconvenient and has security implications. Moreover, the battery is not suitable for rapid charge and discharge with the undesirable cycling life. Ni-Cd battery is another battery technology without low cost. Unfortunately, the battery is environmentally unfriendly because of Cd. Also, the battery has low capacity and unfavorable cycling life of 500 times. Moreover, the battery has a memory effect, which means the battery in not suitable for varied charge/discharge models.[13] NiMH battery is the next generation of Ni-Cd battery, with improved ~ 30% capacity storage compared with Ni-Cd battery.[14] The battery has a longer cycling life of 1000 times and no memory effect. However, for this battery, the price is high, and the electrochemical performance is worse than Li-ion batteries. Lithium-ion batteries possess distinct advantages such as

long cycling life (over 2000 times for $LiFePO_4$), lightweight, rapid charge and discharge, no memory effect, high energy density, etc. [15] Thus, Li-ion battery is the best battery technology among these battery technologies.

1.2.2 Typical working mechanism of Li-ion batteries

It is better to understand the working mechanism of Li-ion batteries before optimizing the performance. The typical working mechanism is based on the insertion/extraction of lithium ions. As displayed in **Figure 1.3a**, a cell mainly consists of four parts: cathode, anode, separator and electrolyte. For cathodes, we are familiar with the commercialized $LiCoO_2$, NCA, $LiMn_2O_4$, $LiFePO_4$ and ternary cathodes. All of the cathodes are based on lithium intercalation/extraction mechanism. And here $LiCoO_2$ is the cathode in **Figure 1.3a**. For anodes, graphite and $Li_4Ti_5O_{12}$ are well-known based on lithium intercalation/extraction mechanism during cycling.[16] In addition, there are two more mechanisms. The one is conversion mechanism, such as the anode of Si, Ge, Sn.[17-20] The other is the alloying mechanism, such as MX (M = Fe, Co, Cu, etc., X = S, O, F, etc.).[21] And here graphite is the anode in **Figure 1.3a**. For separator, the most famous productor is Celgard. Glassfiber also can be used as the separator. The separator isolates the cathode and anode. Meanwhile, it allows lithium-ions to transfer from one side to another side. For electrolyte, lithium ions swim in the electrolyte from one side to another. We choice the electrolyte with high ionic conductivity but without electronic conductivity. The typical electrolytes are based on carbonates. There also have other types of electrolytes for other lithium-ion batteries.

The processes of LIBs during charging/discharge are discussed as below:

(1) during charging, Li-ions are extracted from $LiCO_2$ and then insert into graphite accompanied by electrons through external circuit, with the equations:

$$\text{Cathode: } LiCoO_2 \rightarrow xLi^+ + xe^- + Li_{1-x}CoO_2 \quad (1.1)$$

$$\text{Anode: } xLi^+ + xe^- + C_6 \rightarrow Li_xC_6 \quad (1.2)$$

(2) during discharging, Li-ions are extracted from graphite and then insert into $LiCoO_2$

accompanied by electrons through external circuit, with the equations:

$$\text{Anode: } Li_xC_6 \rightarrow xLi^+ + xe^- + C_6 \quad (1.3)$$

$$\text{Cathode: } xLi^+ + xe^- + Li_{1-x}CoO_2 \rightarrow LiCoO_2 \quad (1.4)$$

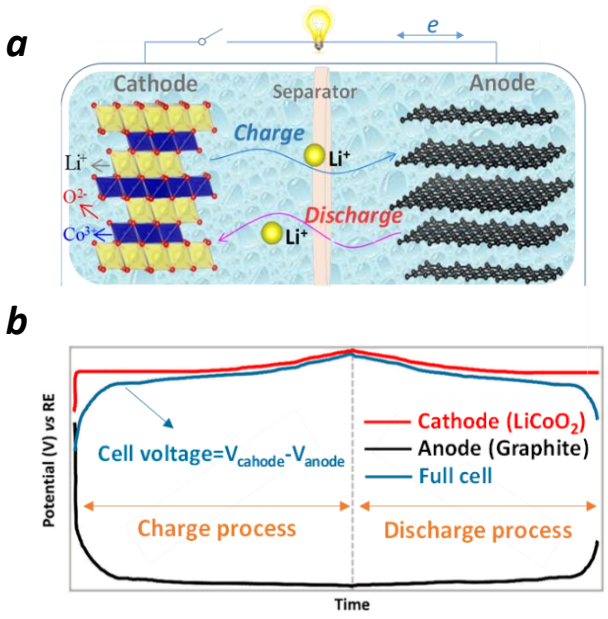

Figure 1. 3 a) Typical working mechanism of Li-ion battery. b) Charge-discharge curves of $LiCoO_2$ (cathode), graphite (anode) and the corresponding full cell.[22]

The reactions are reversible during charging and discharging with reversible migration of Li-ions and redox process, thus we also call lithium-ion batteries as rocking chair batteries.

The charge and discharge profiles of $LiCoO_2$, graphite and corresponding full cell are shown in **Figure 1.3b**. Here we focus on the curve of the full cell, which can be obtained by subtracting the curve of the anode from the curve of the cathode. Output energy (Wh kg^{-1}) of the full cell is calculated by:

$$\text{Output Energy (Wh kg}^{-1}\text{)} = \text{Cell voltage (V)} \times \text{Capacity (mAh g}^{-1}\text{)} \quad (1.5)$$

Here the cell voltage is also obtained by subtracting the voltage of anode from the voltage of cathode.

1.3 Strategies for improving the energy density of Li-ion batteries

The capacity of anodes is always multiplied several times as large as the cathodes. For instance, the reversible specific capacity of commercial graphite (anode) is ~ 360 mAh g^{-1} while the value of commercial $LiCoO_2$ (cathode) is ~ 140 mAh g^{-1}. Thus, the cathodes are very important for the full cell.

It is easy to imagine the strategies for improving the energy density of lithium-ion batteries according to **equation 1.5**: increasing the cell voltage and/or increasing the capacity. Considering that the cell voltage is obtained by subtracting the voltage of anode from the voltage of cathode, we can only concern to improve the voltage of the cathode and consider the anode as constant (the cathode is the research focus in this dissertation). As for the capacity, we know that the capacity has a relationship with the content of extracted lithium ions, which means the more extracted lithium ions, the more capacity the cathode delivers. Considering both voltage and capacity, Li-rich cathodes are highly preferred because they have high potential and more extracted lithium ions, making more specific capacity and higher energy density.

1.4 Li-rich cathodes for Li-ion battery with high energy density

1.4.1 Comparison of Li-rich cathodes and other common cathodes

To intuitive understand the difference between Li-rich cathodes and other typical cathodes, **Figure 1.4a** and **1.4b** exhibit the difference of specific capacity and energy density between them, respectively. The distinct difference in **Figure 1.4a** comes from capacity. Li-rich layered oxides show more than 300 mAh g^{-1} which is obviously larger than others. The capacity can be comparable with the that of graphite (anode). The voltages of them are similar.

The energy density is derived by integrating the areas of the shade, and the results are shown in **Figure 1.4b**.[23] The cell $LiFePO_4$/graphite can be used as the battery of electric vehicles such as BYD. Likewise, the cell NCA/graphite is well-known as the battery of Tesla electrical vehicles, provided by Panasonic Corporation. And the cell

$LiCoO_2$/graphite is widely employed for mobile phone, portable computer, camera and other consumer electronics. However, the energy densities of these commercial batteries are far less than the battery of Li-rich oxides/graphite. Thus, Li-rich oxides are a suitable choice for designing high power density Li-ion battery system. And then we should know the characteristics of Li-rich oxides.

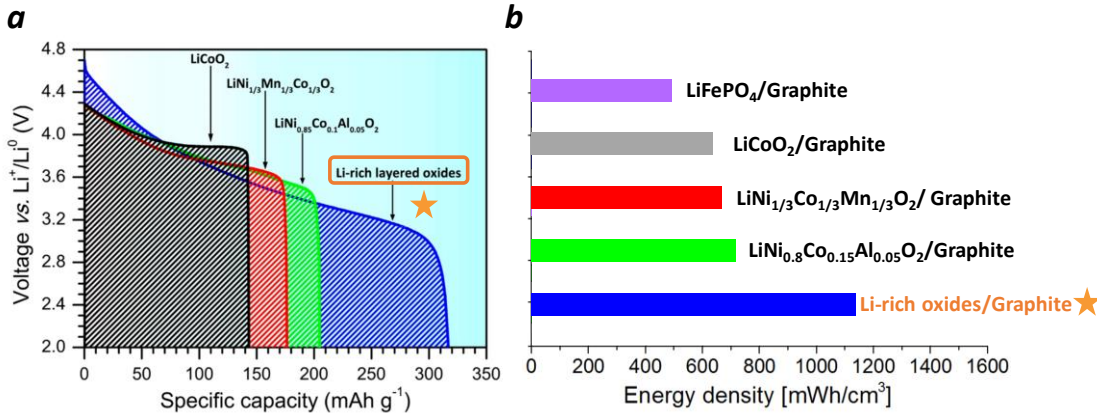

Figure 1. 4 a) Comparison of discharge curves between Li-rich cathodes with some state-of-the-art cathodes. [24] b) Comparison of energy density for full cells based on Li-rich cathodes and some state-of-the-art cathodes with graphite anode. Copyright © 2017, American Chemical Society

1.4.2 The difference between typical layered and Li-rich cathodes

Firstly, a typical layered cathode $LiNi_{0.5}Mn_{0.5}O_2$ and layered Li-rich cathode $Li_{1.2}Ni_{0.2}Mn_{0.6}O_2$ are compared. The difference comes from charge-discharge curves, as displayed in **Figure 1.5**. For $LiNi_{0.5}Mn_{0.5}O_2$, the valences of Ni and Mn are +2 and +4, respectively. During the charging process, lithium ions are extracted from $LiNi_{0.5}Mn_{0.5}O_2$, with the oxidation process of Ni from +2 to +4. The content of Ni in $LiNi_{0.5}Mn_{0.5}O_2$ is 0.5. There is just one electron transport after oxidizing the whole Ni^{2+} to Ni^{4+}. In the meantime, there is just one lithium ions extracted from $LiNi_{0.5}Mn_{0.5}O_2$. And here Mn is inactive because the oxidation process of Ni antedates Mn, after the oxidation process of Ni, there is no more lithium ions can be extracted. For $Li_{1.2}Ni_{0.2}Mn_{0.6}O_2$, the valences of Ni and Mn are also +2 and +4, respectively. Lithium ions are extracted from $Li_{1.2}Ni_{0.2}Mn_{0.6}O_2$ with the oxidation process of Ni from +2 to

+4 during the charging process. The content of Ni in $Li_{1.2}Ni_{0.2}Mn_{0.6}O_2$ is 0.2. That means there is only 0.4 electron transport after oxidizing the whole Ni^{2+} to Ni^{4+}. In the meantime, there is just 0.4 lithium ions extracted from $Li_{1.2}Ni_{0.2}Mn_{0.6}O_2$ with a corresponding chemical formula of $Li_{0.8}Ni_{0.2}Mn_{0.6}O_2$. Then lithium ions continue to be extracted from $Li_{0.8}Ni_{0.2}Mn_{0.6}O_2$. Note that Ni^{4+} is in its highest valence and cannot be oxidized further. Mn^{4+} also cannot be oxidized further in the octahedral site. And then it must be the oxygen to participate in the oxidation process.

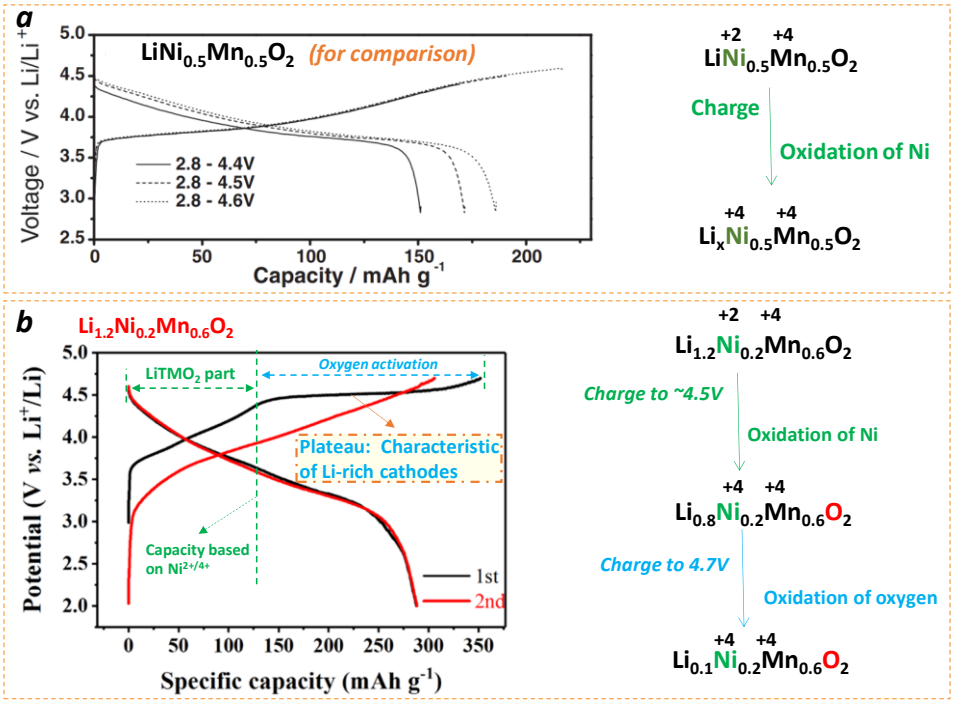

Figure 1. 5 a) Charge-discharge curves of typical layered cathode $LiNi_{0.5}Mn_{0.5}O_2$.[25] b) Charge-discharge curves of layered Li-rich cathode $Li_{1.2}Ni_{0.2}Mn_{0.6}O_2$. Copyright © 2004, The Chemical Society of Japan.

The first charging curve is separated by the green dot line for two parts, as shown in **Figure 1.5b**. The shape of the first part before the line is similar to the layered $LiNi_{0.5}Mn_{0.5}O_2$, named as $LiTMO_2$ part. During this part, the oxidation process is based on typical transition metal oxidation. Then there appears one long plateau in the second part, named as oxygen activation part. During this part, oxygen participates the charge compensation based on anionic redox process. And this long plateau is the characteristic of layered Li-rich cathodes, which is strikingly different from typical layered cathodes such as $LiNi_{0.5}Mn_{0.5}O_2$. The capacity based on the oxidation of transition metal is ~ 130

mAh g^{-1} (extracted 0.4 Li^+) while the capacity based on the oxidation of oxygen is ~ 220 mAh g^{-1} (extracted 0.7 Li^+). The proportion of capacity based on oxygen oxidation is ~ 63%, which is considerable.

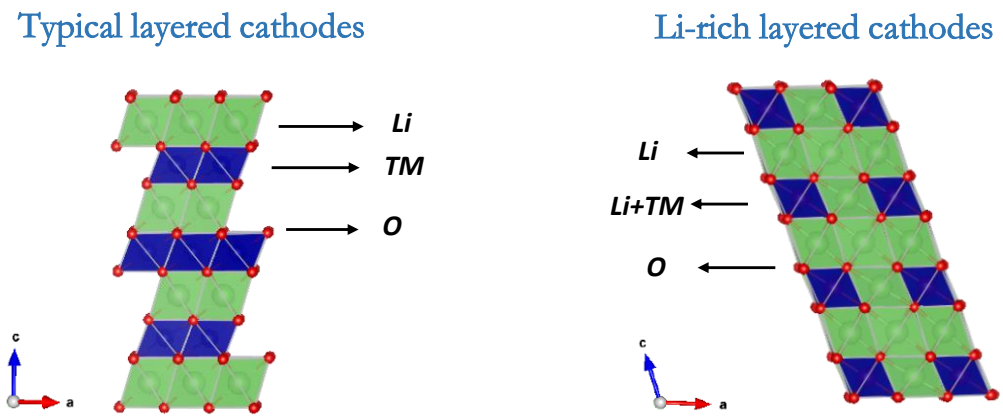

Figure 1. 6 Crystalline structure of a) typical layered cathodes and b) Li-rich layered cathodes. The diagrams are drawn by VESTA software.[26]

Both the two oxides in **Figure 1.5** are layered structure. The electrochemical performance, however, is distinctly different. To understand the difference, the structural difference between them should be cleared. **Figure 1.6** shows the crystalline structure of typical layered cathodes and Li-rich layered cathodes. There are more lithium ions (green) of Li-rich layered cathodes than typical layered cathodes. For typical layered cathodes, their chemical formula can be written as $LiTMO_2$. The content of lithium is one. For layered Li-rich cathodes, the chemical formula can be written as $Li[Li_yTM_{1-y}]O_2$. The content of lithium is 1+y which is larger than one in typical layered cathodes. And this is why we call "rich".

Oxygen, transition metals and lithium arrange layer by layer in sequence for typical layered cathodes, as shown in **Figure 1.6a**. For layered Li-rich oxides, the additional lithium ions occupy the TM layers ideally, as displayed in **Figure 1.6b**. The structure of layered Li-rich cathode is similar to layered structure, with difference just replacing some transition metals in TM layers of typical layered cathodes by lithium ions.

The capacity of cathode/anodes has a direct relationship with the number of transferred electrons in one process. And the theoretical capacity of one electrode is obtained as follows:

(1) Relationship between Charge (Q, in coulombs) and mAh

$$Q = It \quad (1.6)$$

Where Q, I, t are charge, current and time with the unit of coulombs (C), amperes (A), and seconds (s), respectively.

$$\text{then, } 1C = 1A{\cdot}s = (1000mA){\cdot}(\frac{1}{3600}h) = \frac{1}{3.6}mAh \quad (1.7)$$

(2) Relationship between theoretical capacity (C, in mAh g^{-1}) and transferred electrons (n, in mole)

Here we need Faraday constant (F ≈ 96485 C·mol^{-1}), which represents the charge (C) based on one mole (N_A) electrons. When there is n mole transferred electrons during charge-discharge process,

$$C_{theoretical} = \frac{nF}{3.6M} = \frac{26801 \times n}{M} \quad (1.8)$$

Where M is the molecular weight (in g mol^{-1}) of the active material used in the electrode. And transferred electrons are equal to the extracted lithium ions. Li-rich cathodes contain more extracted lithium ions. From **equation 1.8**, it could conclude that n is larger in Li-rich cathodes than in typical layered cathodes. Thus Li-rich cathodes will deliver larger capacity.

The typical layered cathodes have a similar layered structure with Li-rich layered cathodes. What the influence after replacing some transition metals by lithium ions besides the charge-discharge profiles? Also, they display similarity on XRD patterns, as displayed in **Figure 1.7**. $LiCoO_2$ and Li_2MnO_3 here as examples represent the typical layered cathode and layered Li-rich cathode, respectively. Li_2MnO_3 is equivalent to $Li[Li_{1/3}Mn_{2/3}]O_2$, which means 1/3 lithium occupies and 2/3 transition metal occupies TM layers according to **Figure 1.6**. Actually, Li and Mn arrange as a series of …LiMnMn…in the TM layers, resulting in a honeycomb structure as shown in

Figure 1.7b. As for $LiCoO_2$, only Co occupies TM layers, as shown in **Figure 1.6a**. Their XRD patterns are calculated by VESTA [26] software with a range of 2θ from 10° to 40°. there are only four peaks at this range in $LiCoO_2$ with no peaks between 20° and 35°. However, there are five more peaks between 20° and 35° in Li_2MnO_3 (marked by the green rectangle) in addition to the same four peaks in $LiCoO_2$. The additional peaks are known as superlattice peaks resulting from an additional superlattice cell caused by the ordered [$LiMn_2$] arrays. And these additional peaks are the characteristic of Li-rich cathodes, which can be distinguished from the typical layered cathodes.

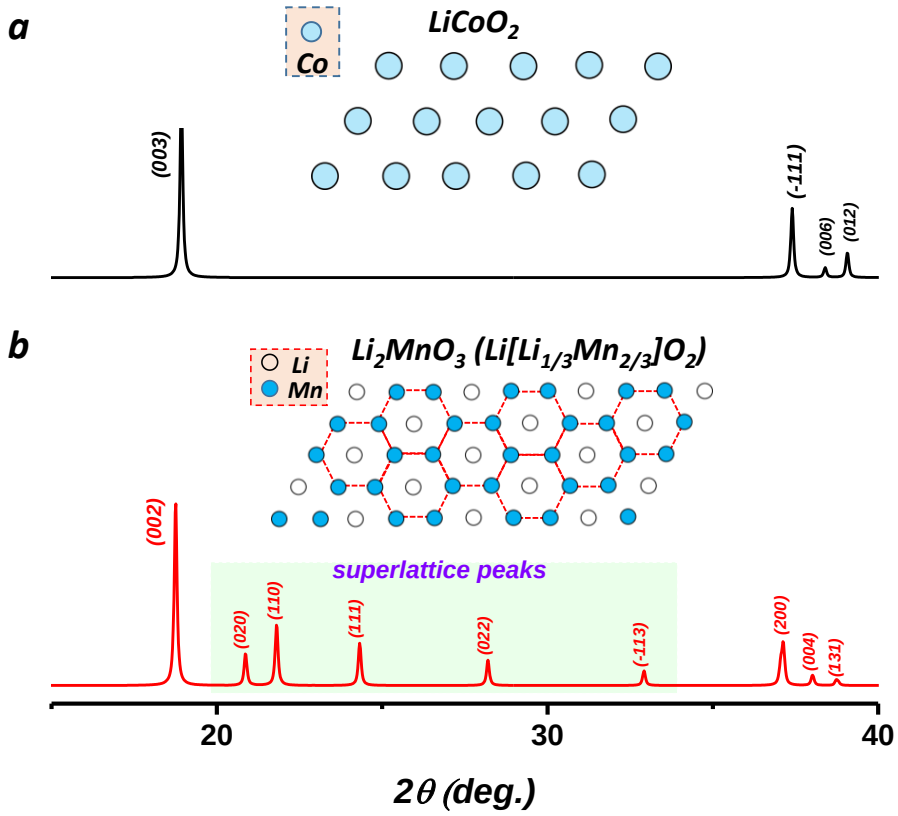

Figure 1. 7 Calculated XRD patterns of a) typical layered cathode $LiCoO_2$ and b) Li-rich layered cathode Li_2MnO_3.

1.4.3 Mechanism of oxygen activation in Li-rich cathodes

After discussing the difference of charge-discharge profile and XRD pattern caused by additional lithium substitution, it is also unclear why oxygen in Li-rich cathodes can be activated while cannot in the typical layered cathode. First-principles calculations

are helpful to reveal oxygen activation in Li-rich cathodes. As shown in **Figure 1.8**, the structural configuration around oxygen and corresponding schematic band structure of typical layered cathode (such as $LiCoO_2$) and layered Li-rich cathode (such as Li_2MnO_3) are compared. For typical layered cathodes, on the sides of oxygen layer, there are TM and lithium layer, respectively, as shown in the red dotted rectangle (TM layer) and purple dotted rectangle (Li layer) in **Figure 1.8a**. Thus, the environments around oxygen are the same, consisting of three Li-O-TM configurations. And for this type stoichiometric layered $LiTMO_2$ oxide, the energy band of transition metal is higher than that of oxygen. An obvious gap separates TM bands and oxygen bands, which means it is difficult for oxygen to participate in the oxidation process (poor electron donors) when all the transition metals are oxidized.

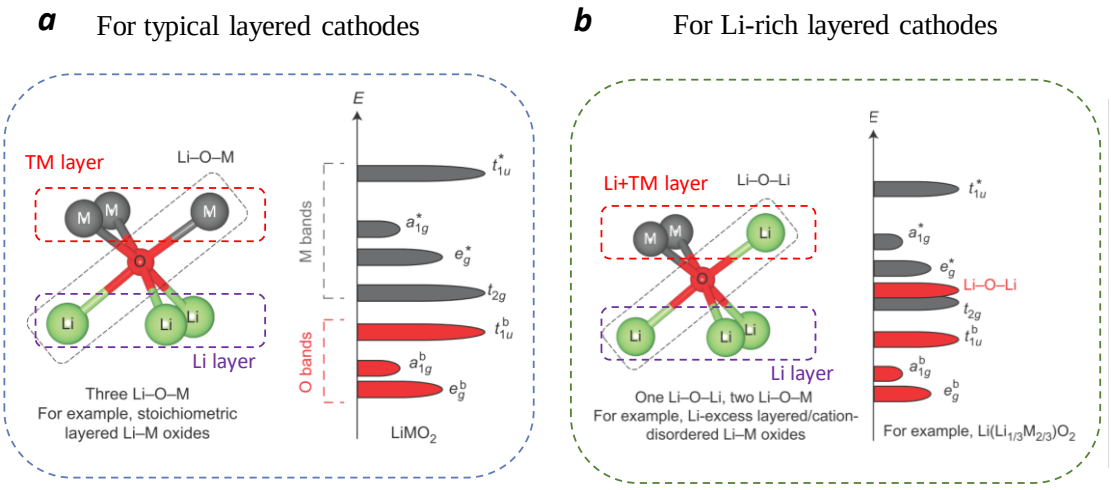

Figure 1. 8 Structural configurations around oxygen and corresponding schematic band structure. a) For typical layered cathodes and b) for Li-rich layered cathodes. [27] Copyright © 2016, Springer Nature.

For Li-rich cathodes, the lithium layer is the same as stoichiometric layered $LiTMO_2$ oxide. TM layer, however, is different because some lithium also occupies this layer, as shown in the red dotted rectangle (Li+TM layer) and purple dotted rectangle (Li layer) in **Figure 1.8b**. For a typical example of Li-rich oxide Li_2MnO_3, the environments around oxygen are different, consisting of both Li-O-Li and Li-O-TM configurations. The difference is caused by the additional lithium at TM layers and then influences the energy band of oxygen. For this Li-rich layered Li_2MnO_3 oxide, the energy band of

transition metal is mixed with one band of oxygen. The increased oxygen band results from the special Li-O-Li configuration. And for this cause, it will be possible for oxygen to participate in the oxidation process (potential electron donors) because the energy of oxygen is similar to the transition metals.

Here should be a brief summary of the influence after Li substitution in Li-rich oxides. There are mainly four points. The first, charge-discharge profile is changed in Li-rich oxides compared with stoichiometric layered oxides, represented by a long plateau at high potential, which is a symbol of oxygen activation. The second, it is a little bit different from the structure because there are both lithium and transition metal in the TM layers in Li-rich oxides while only transition metal occupies TM layers in stoichiometric layered oxides, although both types oxides own layered structure. The third, XRD pattern shows additional peaks in Li-rich oxides, named as superlattice peaks, resulting from the ordered arrangements of [$LiMn_2$] arrays in TM layers. However, there are no superlattice peaks in stoichiometric layered oxides. The fourth, the energy of oxygen in Li-rich oxides is raised due to Li-O-Li configuration, making the oxygen more easily oxidized. While in stoichiometric layered oxides, the oxygen cannot be oxidized based on three same Li-O-TM configurations. And this is the reason why oxygen can be activated and then the oxides deliver more capacity.

1.4.4 The problems and challenge in Li-rich cathodes

1.4.4.1 Lack of direct observation of oxygen behavior

As shown in **Figure 1.9a**, we have already known oxygen activation appears at high potential with a long plateau till the end of the charging process. And oxygen gas is always released from the lattice, evidenced by gas evolution test from **Figure 1.9b**, which can be found at the end of charge process in some works. [29-31] Also, the oxygen in the lattice can be the source forming CO_2 and Li_2CO_3 besides O_2. [29] There are diverse ways for oxygen from O^{2-} to other types of oxygen, as shown below:

$$O^{2-} \rightarrow O^{-} \rightarrow O_2^{-} \rightarrow O_2 \uparrow \quad (1.9)$$

$$O^{2-} \rightarrow O^{-} \rightarrow O_2^{-} \rightarrow Li_2CO_3 \quad (1.10)$$

$$O^{2-} \rightarrow O^{-} \rightarrow O_2^{-} \rightarrow CO_2 \uparrow \quad (1.11)$$

$$O^{2-} \rightarrow O^{-} \rightarrow O_2^{2-} \quad (1.12)$$

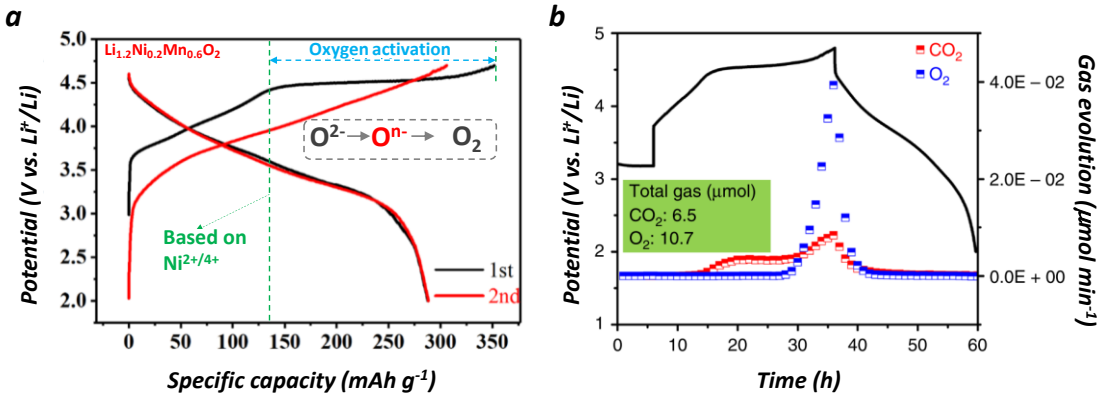

Figure 1. 9 a) Typical charge-discharge profiles of Li-rich oxide $Li_{1.2}Ni_{0.2}Mn_{0.6}O_2$ for the first two cycles. b) Gas evolution of $Li_{1.2}Ni_{0.2}Mn_{0.6}O_2$ by operando differential electrochemical spectrometry (DEMS) for the first cycle. [28] Copyright © 2018, Springer Nature.

The formed O_2^- can attack the electrolyte and then generate to Li_2CO_3. These pathways are the possibilities for the evolution of lattice oxygen in Li-rich oxides. However, we don't ensure which is the main pathway. Confirmation of its pathway is important because oxygen activation is very significant for designing large capacity Li-ion battery systems. And we can pertinently bring forward corresponding methods to stabilize the oxygen activation.

Many researchers have reported the evidence of oxygen activation in Li-rich cathodes by utilizing technologies of DEMS, X-ray photoelectron spectroscopy (XPS), and other synchrotron radiation devices. [32-33] However, they only confirm the oxygen activation and the detailed pathways of oxygen are still unknown. Thus, the first challenge for developing Li-rich oxides is lacking direct observation of oxygen behavior.

1.4.4.2 Severe capacity fade and voltage fade

The first challenge is about the mechanism, the second is about electrochemical

performance. For Li-rich oxides, there are additional lithium ions in TM layers, resulting in the oxygen activation and large capacity. For the same reason, however, the additional lithium ions will be extracted from TM layers. Then, the problems appear. The stability of the structure is weakened because the small number of transition metals cannot maintain the stability of the whole structure after additional lithium-ion extracted from TM layers. Meanwhile, a crystal defect is caused by the absence of a lithium ion. Then transition metals near the crystal defect migrate easily from their sites to Li layers through the defect. The migration is irreversible because transition metal is stable when occupies the octahedral site in Li layers. The fixed TMs hinders the migration of lithium ions, resulting in the capacity decay. The inevitable oxygen loss after charging in layered Li-rich oxides results in a phase transition, accounting for the capacity decay and voltage decay further, as shown in **Figure 1.10**.

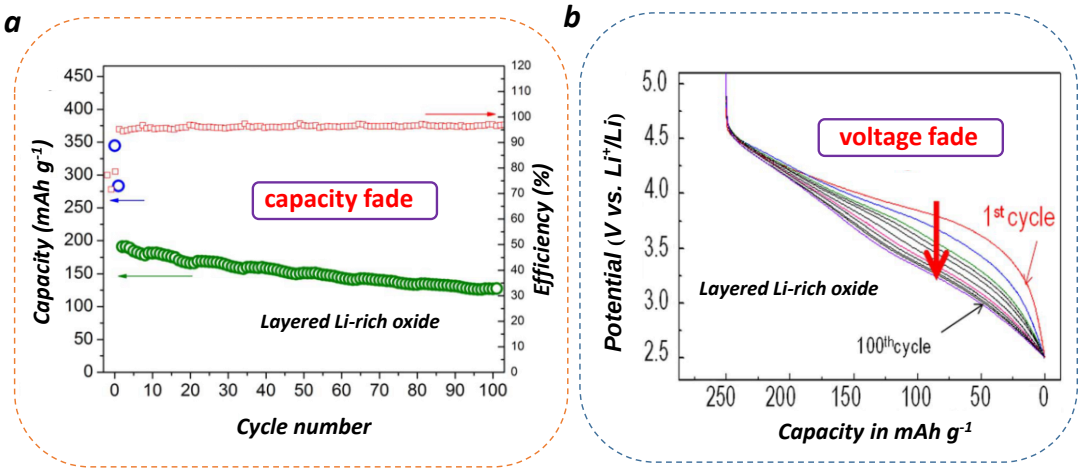

Figure 1. 10 Typical cycling performance of Li-rich oxide with a) severe capacity fade ($Li(Li_{0.2}Mn_{0.6}Ni_{0.1}Co_{0.1})O_2$) and b) voltage fade ($Li(Li_{0.17}Ni_{0.29}Mn_{0.58})O_2$). [34-35] Copyright 2019 Copyright Clearance Center.

1.5 Motivation and targets of this dissertation

1.5.1 Motivation of this dissertation

Energy storage devices are very important for storing energy from nature. There are many battery technologies as the rule of energy storage device. Among these battery

technologies, lithium-ion battery is the best choice because it possesses enormous advantages such as long cycling life, lightweight, friendly to the environment, rapid charge and discharge, high energy density, etc. While other battery technologies have disadvantages more or less.

Cathodes are the key points of the full cell. Most of the cathodes base on intercalation/extraction mechanism during cycling. The capacity delivered by the cathode has a direct relationship with the number of extracted lithium ions (transferred electrons). Li-rich cathodes contain more lithium ions than other types of cathodes. It could conclude that Li-rich cathodes will deliver higher capacity compared with other cathodes according to **equation 1.8**. Meanwhile, the special structure of Li-rich oxide makes the energy oxygen increased due to Li-O-Li configuration. Then the oxygen with higher energy is more easily oxidized. And this is the reason why oxygen can be activated and then more capacity is delivered in Li-rich oxides. Thus, Li-rich oxides are the focus of this dissertation.

However, the mechanism of the detailed pathways of oxygen activation is still unknown. And after most lithium ions extracted from TM layers, the stability of the structure is weakened. Then irreversible migration of transition metals appears, leading to the capacity fade and voltage fade. So, to solve or alleviate the problems or challenges in layered Li-rich oxide is our motivation for this dissertation.

1.5.2 Targets of this dissertation

The targets of this dissertation on layered Li-rich oxides are as follows:

The first target is to obtain direct observation about the detailed pathways of oxygen activation. Raman spectroscopy has been employed due to the sensitivity to covalent bonds. And many researchers applied Raman spectra to detect oxygen behavior. However, they failed to obtain the signals because the signal of covalent oxygen bonds is too weak to detect. In this work, surface-enhanced Raman spectroscopy (SERS) is employed by gold nanoparticles (NPs) to improve the signal. To obtain more details of oxygen activation, in-situ test companied with charge-discharge profiles are utilized.

And the in-situ Raman cell in our research is shown in **Figure 1.11**.

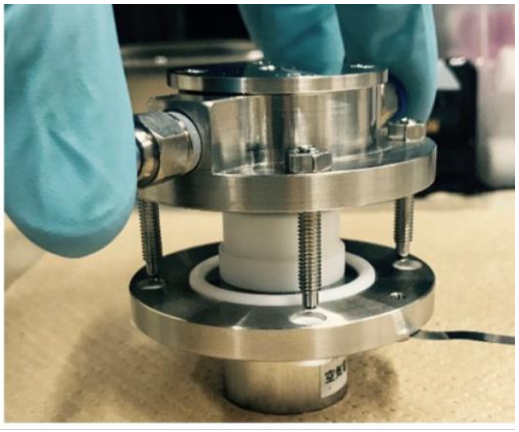

Figure 1. 11 In-situ Raman cell utilized in this dissertation

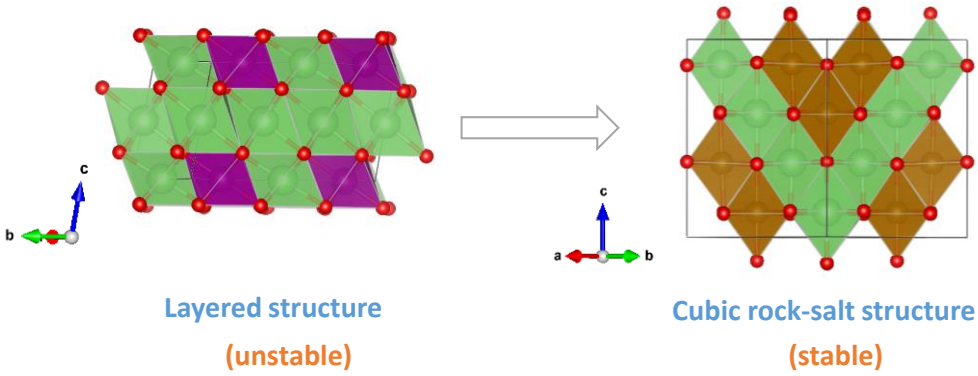

Figure 1. 12 Schematic of layered Li-rich oxides and cubic rock-salt Li-rich oxides. The diagrams are drawn by VESTA software.

The second target is to alleviate the capacity fade and voltage fade in layered Li-rich oxides. Phase transition is very common in a layered structure, especially for layered Li-rich oxides. Structural stability is the key factor to maintain capacity stability and voltage stability. Cubic rock-salt oxides always own stable structure with firm oxygen network. This guides us the direction and gives us inspiration. It may be feasible to design the cubic rock-salt Li-rich oxides with a stable structure to alleviate the capacity fade and voltage fade. The schematic comparison of the layered structure and cubic rock-salt structure is shown in **Figure 1.12**.

1.5.3 Outline of this dissertation

This dissertation contains five chapters illustrated as following:

Chapter 1 is a general instruction for the whole dissertation. In this chapter, the background of the urgent demand for high energy storage is discussed. Some battery technologies are compared, indicating that Li-ion battery is the best choice. Then, layered Li-rich oxides are introduced compared with typical layered oxides. Moreover, we also exhibit their problems. Finally, we present our motivation and provide our method of how to deal with the problems in layered Li-rich oxides.

Chapter 2 is the experimental section of Chapter 3 and Chapter 4. In this chapter, the synthesized method, testing condition, main operation steps and highlights of this dissertation are introduced.

Chapter 3 is the work about the direct observation of oxygen behavior. In this chapter, various in situ technologies such as XRD and Raman spectroscopy are employed for a typical Li-rich material $Li_{1.2}Ni_{0.2}Mn_{0.6}O_2$ to investigate the structural evolution and oxygen behavior. The reversible phenomenon of O^{-}–O^{-} (peroxo oxygen dimers) bonds forming mostly along the c-axis is directly visualized. Moreover, density functional theory was employed to calculate the peroxo bond. Results are consistent well with our experimental observation.

Chapter 4 is the work about improving the capacity stability and voltage stability of Li-rich oxides by designing a cubic rock-salt structure. In this chapter, a new rock-salt Li-rich oxide $Li_2Ni_{1/3}Ru_{2/3}O_3$ is reported. The oxide has advantages of high capacity with stable cycling stability and neglectable voltage fade. Of course, oxygen behavior was observed in this oxide during cycling for the first time, as a type of peroxo O^{-}–O^{-} bonds, which is similar to the typical layered Li-rich oxides. Moreover, first principle calculations were employed to confirm the oxygen behavior and high kinetics in this oxide.

Chapter 5 is the general conclusions and perspective for future research in this field.

Chapter 2. Experimental section

2.1 Experimental section of Chapter 3

2.1.1 Synthesis of $Li_{1.2}Ni_{0.2}Mn_{0.6}O_2$

We choose the typical layered $Li_{1.2}Ni_{0.2}Mn_{0.6}O_2$ as our target material because the oxide has the common characteristics of layered Li-rich oxides. At first, the precursor Ni_xMn_yOH (x:y=1:3) was synthesized by using the co-precipitation method which is very common for synthesizing this material. Reagents include $LiOH{\cdot}H_2O$ (AR, Sinopharm Chemical Reagent Co., Ltd.), NH_4OH (AR, Nanjing Chemical Reagent Co., Ltd.), $NiSO_4{\cdot}6H_2O$ (AR, Enox), $MnSO_4{\cdot}H_2O$ (AR, Xilong Chemical Industry Co., Ltd.), and sodium hydroxide (AR, Nanjing Chemical Reagent Co., Ltd.). All the chemicals are not purified further. Briefly, a base solution was prepared by adding 500 mL 1 M NH_3 (aq) into a vessel. After heating the base solution to 60 ^oC, the deoxidized aqueous solution of metal sulfates (the ratio of Ni and Mn was controlled by 1:3) were slowly dropped into the base solution controlled by peristaltic pumps, with a stable pH value of ~ 9.8 maintained by NaOH (aq). The whole processes were in a protective gas of N_2. After filtering and washing adequately, a black precursor was obtained and then dried in a drying oven at 80 ^oC for 10 h.

To synthesize the target $Li_{1.2}Ni_{0.2}Mn_{0.6}O_2$, the as-prepared precursor Ni_xMn_yOH (x:y = 1:3) was grinded with $LiOH{\cdot}H_2O$ (3 wt% excess) powders thoroughly by hands for half an hour. The target oxide was obtained by calcining the mixtures at 750 ^oC for 12 h in air.

2.1.2 Characterizations

Powder XRD (Ultima III, Rigaku Corporation) was employed to confirm the structure of $Li_{1.2}Ni_{0.2}Mn_{0.6}O_2$ with radiation from Cu Kα (λ = 1.5406 Å). The data was collected between diffraction angles (2θ) from 10 ^{o} to 80 ^{o} at a scan rate of 2 ^{o} per min.

General Structure Analysis System (GSAS) + EXPGUI suite is utilized for Rietveld refinements.

For in-situ XRD test, a home-made cell was employed which will be introduced in the following part. The cell was also connected to an electrochemical workstation to the corresponding charge/discharge profiles. During test, the current density of charge/discharge was controlled to 10 mA g^{-1}. The data of every XRD pattern was collected between diffraction angles (2θ) from 12 ° to 50 ° with a test time of one hour and an interval of 5 min till the end of the charge/discharge test for the first two cycles. GSAS + EXPGUI suite is employed for Rietveld refinements for all the in-situ XRD patterns.

The morphologies of the materials were characterized by SEM (scanning electron microscopy) (JSM-7000F). For SEM samples, a grain of the precursor was dropped into 1 mL ethanol in a glass bottle with a volume of 2 mL. Then the solution was treated with an ultrasonic processing. After ~ 10 min, the solution was dropped onto an Al film by a dropper and dried in an oven at 60 °C. Then the sample was prepared by attaching the Al film (with a trace of material) on a conductive adhesive. The sample of $Li_{1.2}Ni_{0.2}Mn_{0.6}O_2$ was treated the same as the precursor. The conductive adhesive was placed onto a SEM sample holder and then the holder was shifted to the SEM sample loading chamber.

XPS was characterized by a Thermo Fisher Scientific Model Kα spectrometer equipped with Al Kα radiation (1486.6 eV). Before XPS test, the sample was transferred into an Ar glove box and sealed in an airtight container to avoid the exposure with the humidity. Exposure of the sample in air is inevitable when transferring the sample. We assumed that the characteristics of the oxide would not be influenced within such a short exposure time.

2.1.3 Electrochemical tests

2032 coin-type cells were employed for electrochemical measurements. The electrodes consisted of active material, acetylene black, and polytetrafluoroethene

(PTFE, 12 wt.%) binder with a weight ratio of 85:10:5. The electrodes were dried at 80 ^{o}C overnight after pressed onto an Al mesh. And then the electrodes were transferred into the glovebox and assembled into the coin cells. 1 M (1 mol L^{-1}) $LiClO_4$ in propylene carbonate (PC) was prepared as the electrolyte. LAND 2001A Battery Testing Systems (Wuhan LAND electronics Co., Ltd, P.R. China) were employed for galvanostatic testing. The current density was different according to the test conditions. The potential window was set between 2.0 V ~ 4.8 V. The open circuit potential (OCP) was ~ 3.0 V.

2.1.4 Device for in-situ XRD tests

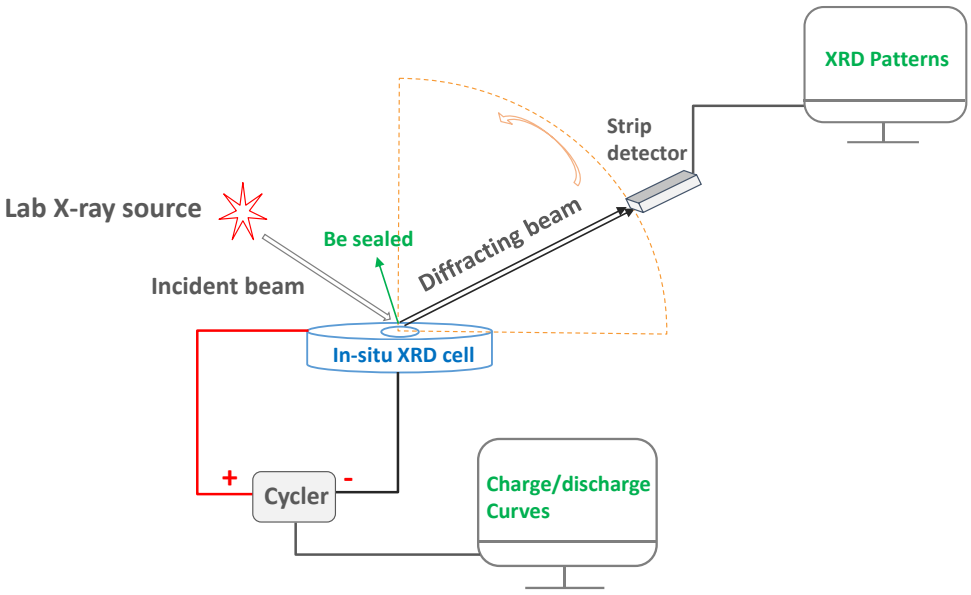

Figure 2. 1 Schematic of device for in-situ XRD test companied with charge/discharge test

Li-ions migrate from the cathode during cycling, inducing the structural evolution. XRD test is sensitive to the crystal structure, giving us important information about phase transition. To obtain more details of the phase transition, in-situ XRD test was employed. The schematic of the device for in-situ XRD test is shown in **Figure 2.1**. The cell is tested for in-situ XRD and charge/discharge performance simultaneous. The in-situ cell is homemade, with a window sealed by Be metal. The window allows X-ray to through into the cathode and Be metal has a good permeability for X-ray. Meanwhile, the in-situ cell is connected to one electrochemical workstation for charge/discharge

test. Thus, we can obtain the results of a series of XRD patterns and charge/discharge curves at the same time. To test more precise XRD patterns, each pattern was test about one hour. And details of testing conditions can be seen in section 2.1.2.

2.1.5 Device for in-situ Raman tests

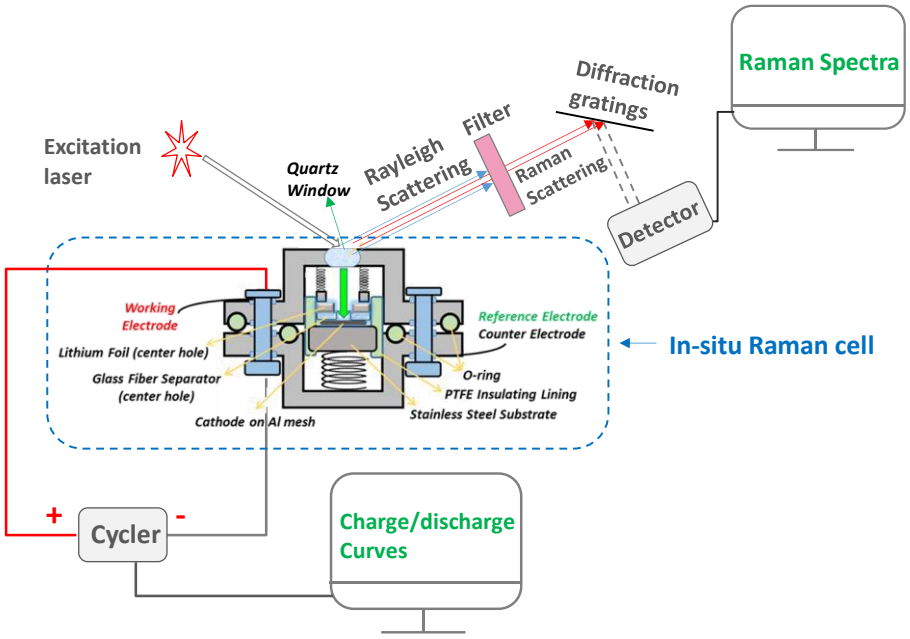

Figure 2. 2 Schematic of device for in-situ Raman test companied with charge/discharge test

Oxygen behaviors can be detected by Raman spectroscopy because of its sensitivity to covalent bonds. To detect a more accurate data, in-situ method is employed. The schematic of the device for in-situ Raman test is shown in **Figure 2.2**. The cell is tested for in-situ Raman and charge/discharge performance simultaneous. The in-situ cell is homemade, with a window sealed by quartz. The window allows the laser to through into the cathode, then the information of the cathode is obtained, and the in-situ Raman spectra of the materials are obtained by using JASCO microscope spectrometer (NRS-1000DT). The modified in-situ Raman cell used in this study is designed by us and made by one corporation (Hohsen Corp., Osaka, Japan) for the Li-ion battery. Briefly, a thin quartz window allows the Raman laser go through, fixing on the top of the cell. Meanwhile, the in-situ cell is connected at one charge/discharge machine for

galvanostatic test. Thus, we can obtain the results of a series of Raman patterns and charge/discharge curves at the same time.

2.1.6 Experiment for Raman test

In this work, Surface-enhanced Raman spectroscopy (SERS) is employed by gold nanoparticles (NPs) because the covalent bonds of oxygen are too weak to detect. In order to collect shell-isolated nanoparticle-enhanced Raman (SHINER) signal, NPs approximately 40 nm in diameter with a SiO_2 coating shell (~ 5 nm) were synthesized. Au@SiO_2 NPs were washed and ultrasonic treated uniformly before dropped onto the working electrodes. Then the electrodes were dried at oven before assembly. During assembling in the glove box, the working electrode was firstly put at the bottom of in-situ cell. Then a glass fiber was used as the separator, with a hole (diameter of 2mm) in the middle, covering on the working electrode. The limited electrolyte of ~ 60 μL was dropped on the separator. In the end, a lithium foil was put on the top of the separator, with a same hole in the center as displayed in separator. The hole allows the laser reach working electrode and obtain the Raman singal. The cell remains at rest overnight to reach a stationary state. The OCP of the cell was ~ 3 V before subsequent tests.

A JASCO microscope spectrometer (NRS-1000DT) was employed to record Raman spectra. The laser was focused on working electrode with 632.8 nm wavelength. A 50 × lens was chosen (Olympus America Inc.). The power of laser was controlled with a ~ 10% of the maximum 30 mW laser intensity to keep a stable Raman signal and no damage on the working electrode. The collection time of one spectrum was ~ 10 min with two accumulations. To obtain a reproducible and credible result, we checked at least three places of working electrode. The spectral resolution was ca. 1.0 cm^{-1}.

The Raman signal and electrochemical curves were tested at the same time. A machine (Potentiostat/Galvanostat PGSTAT30, Autolab Co. Ltd., Netherlands) was controlled for galvanostatic model, companied by a software (General Purpose Electrochemical Software, GPES) for collecting electrochemical data. The current was controlled at a density of 5 mA g^{-1}., with a potential window of 2 V~ 4.8 V.

2.1.7 Highlights of Chapter 3

As mentioned in chapter 1, oxygen behavior accounts for the high capacity beyond the traditional calculated capacity based on redox process of transition metal in Li-rich oxides. Oxygen loss as a type of O_2 can be detected in charging process. Thus, we can conclude that oxygen changes to O_2 after oxidized process. However, we don't know more about oxygen behavior because there are many pathways from O^{2-} to O_2 (with the possible intermediate states such as types of O_2^{2-} and O_2^{-}). It's important to know the substantial oxygen behavior as it can help us stabilize the oxygen behavior and improve the electrochemical performance. Raman spectroscopy is a powerful tool to investigate covalent bonds. Herein it can detect the states of oxygen during charging. However, the Raman signals of covalent O-O bonds are usually too weak to obtain, which is the reason why other researches can obtain anything. In this work, we employed in-situ surface-enhanced Raman spectra to rise the signal remarkably and obtain more details of oxygen behavior. As a result, oxygen behavior was directly confirmed as a type of peroxo O-O bond, indicating that the valence of oxygen is changed from -2 to -1. More importantly, the evolution of O^{2-} to O^{-1} is reversible not only for the first cycle, but also for the subsequent cycles. The findings help us to understand deeply on the oxygen behavior in Li-rich oxides.

2.2 Experimental section of Chapter 4

2.2.1 Synthesis of $Li_2Ni_{1/3}Ru_{2/3}O_3$

It is better to synthesize the cathode based on Ni and Mn so that it can be easily compared with $Li_{1.2}Ni_{0.2}Mn_{0.6}O_2$ in Chapter 3. At first, I tried to synthesize cubic rock-salt Li-rich cathode ($Li[Li_xNi_yM_{1-x-y}]O_2$) based on Mn (M = Mn). However, layered structure always be obtained rather than the cubic rock-salt structure. Then, other *3d* transition metals such as Cr and V were attamped, with a different component, ratios of elements and sintering temperature. However, I still failed. *4d* transition metals (Ru, Nb et al.) were then considered. After repeated failure, $Li_2Ni_{1/3}Ru_{2/3}O_3$ heaves in sight, with

Fd-3m space group, having the partial cation-ordering arrangement.

$Li_2Ni_{1/3}Ru_{2/3}O_3$ powder was synthesized by solid-state reactions with Li_2CO_3 (Wako), NiO (Wako) and RuO_2 (Wako). All the chemicals are not purified further. The starting materials were weighed and mixed at a ratio of Li:Ni:Ru=6.12:1:2 and grinded for half an hour with hands. Then the mixed powder was pelleted and calcined at 750 ºC in air for 15 h, subsequently followed by calcined at 950 ºC for 20 h in air.

2.2.2 Characterizations

Powder XRD (Ultima III, Rigaku Corporation) was employed to confirm the structure of LNRO with radiation from Cu Kα (λ = 1.5406 Å). The data was collected between diffraction angles (2θ) from 10 º to 80 º with an increment of 0.02 º at a scan rate of one second per data. The working voltage was 40 kV and working current was 40 mA. General Structure GSAS + EXPGUI suite is employed for Rietveld refinements.

For in-situ XRD test, a home-made cell was employed which will be introduced in the following part. The cell was also connected to an electrochemical workstation to the corresponding charge/discharge profiles. During test, the current density of charge/discharge was controlled to 10 mA g^{-1}. The data of every XRD pattern was collected between 2θ from 15 º to 65 º with a test time of 40 min and an interval of 5 min till the end of the charge/discharge test.

The morphologies of the oxide were confirmed by SEM (JSM-7000F). For SEM samples, a grain of the LNRO was dropped into 1 mL ethanol in a glass bottle with a volume of 2 mL. Then the solution was treated with an ultrasonic processing. After ~ 10 min, the solution was dropped onto an Al film by a dropper and dried in an oven at 60 ºC. Then the sample was prepared by attaching the Al film (with a trace of material) on a conductive adhesive. The conductive adhesive was placed onto a SEM sample holder and then the holder was shifted to the SEM sample loading chamber.

XPS was characterized by a Thermo Fisher Scientific Model Kα spectrometer equipped with Al Kα radiation (1486.6 eV). Before XPS test, the sample was transferred into an Ar glove box and sealed in an airtight container to avoid the exposure

with the humidity. Exposure of the sample in air is inevitable when transferring the sample. We assumed that the characteristics of the oxide would not be influenced within such a short exposure time.

In situ GC-MS (gas chromatography mass spectrometry) measurements were carried out using a homemade cell linked to one machine from Perkin-Elmer (Clarus 680 and SQ 8S). The machine is very sensitive to the gas (CO_2 and O_2) generated during cycling. And we can collect evolution of gas while charging the cell.

2.2.3 Electrochemical tests

2032 coin-type cells were used for electrochemical measurements. LNRO electrode consisted of active material, acetylene black, and PTFE (12 wt.%) binder with a weight ratio of 85:10:5. After pressing the electrodes onto an Al mesh, they should be dried at 80 ^{o}C overnight. And then the electrodes were transferred into the glovebox and assembled into the coin cells. The electrolyte used in this study is 1 M $LiPF_6$ in EC/DEC (ethylene carbonate/diethyl carbonate). And a glass fiber film was employed as separator. The electrochemical performances were performed by employing a Hokuto Denko HJ1001SD8 battery tester with galvanostatic model. The potential window was set between 2.0 V ~ 4.2 V. The current density was different according to the test conditions. The OCP was ~ 3.0 V.

2.2.4 Device for in-situ XRD tests

The schematic of the device for in-situ XRD test is similar to that which is shown in **Figure 2.1**. The cell is tested for in-situ XRD and charge/discharge performance simultaneous. The coin cell with a window was employed for in-situ test. A Kapton film was annealed with a thermoplastic for sealing the coin cell. Meanwhile, the in-situ cell is connected to one electrochemical workstation for charge/discharge test. Thus, we can obtain the results of a series of XRD patterns and charge/discharge curves at the same time. To test more precise XRD patterns, each pattern was test about 40 min. And details of testing conditions can be seen in section 2.2.2.

2.2.5 Device for in-situ Raman tests

The schematic of devices for in-situ Raman test is shown in **Figure 2.3**. The cell is tested for in-situ Raman, charge/discharge performance and gas evolution simultaneous. The in-situ cell is homemade, with a window sealed by quartz. The window allows laser to through into the cathode, then the information of the cathode is obtained, and the in-situ Raman spectra of the materials are obtained by using JASCO microscope spectrometer (NRS-1000DT). Briefly, a thin quartz window allows the Raman laser go through, fixing on the top of the cell. Meanwhile, the in-situ cell is connected at one charge/discharge machine for galvanostatic test. And also, the homemade cell was linked to one machine (Perkin-Elmer, Clarus 680 and SQ 8S) for gas collection. Thus, we can obtain the results of a series of Raman patterns companied with charge/discharge curves and gas evolution at the same time.

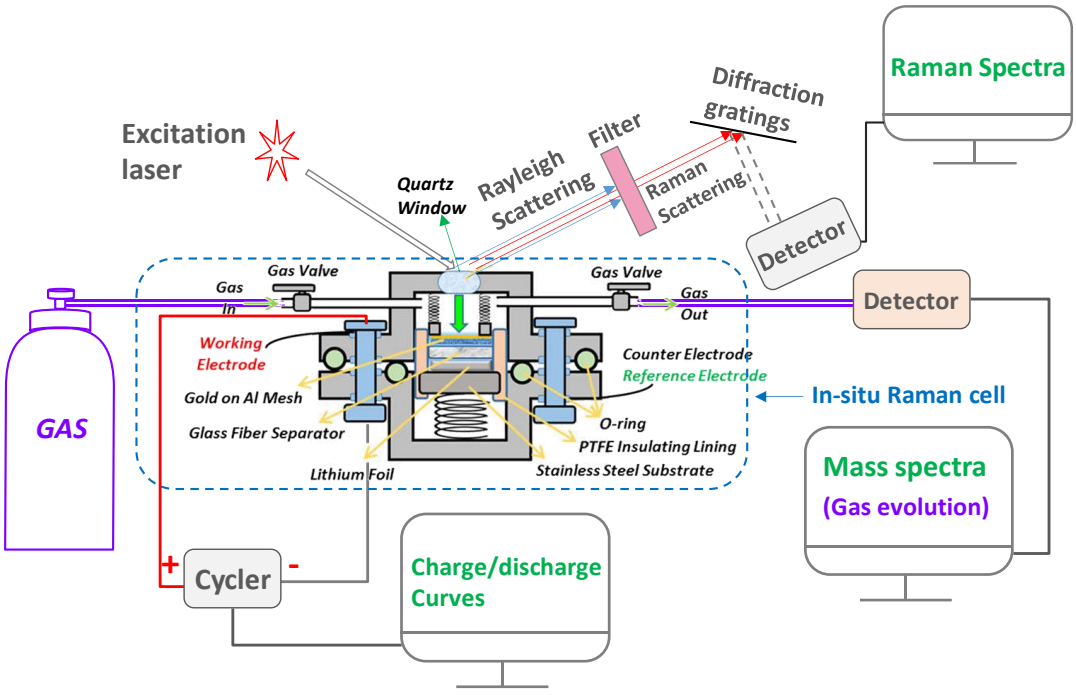

Figure 2. 3 Schematic of device for in-situ Raman test companied with charge/discharge test and gas evolution.

2.2.6 Experiment for Raman test

In this work, surface-enhanced Raman spectroscopy (SERS) is still employed by gold nanoparticles (NPs) because the covalent bonds of oxygen are too weak to detect. Details can be found in section 2.1.6.

2.2.7 Highlights of Chapter 4

As mentioned in chapter 1, typical layered Li-rich oxides often suffer from the phase transition caused by oxygen loss, leading to a serious capacity fade and voltage fade, which hinders the development of Li-rich oxides. Thus, structural stability is the key point to stabilize the oxygen behavior and electrochemical performance of Li-rich oxides. As is known, cubic rock-salt structure is more stable than layered structure. It is reasonable to apply the stable cubic rock-salt structure with Li-rich environment to improve the oxygen behavior. And as a result, the electrochemical performance is improved, which is our purpose in chapter 4. After lots of trials, a cubic rock-salt Li-rich oxide was successfully synthesized. As a result, the oxide has an obvious improvement on capacity stability and voltage stability. More importantly, oxygen behavior is stable and well reversible in this cubic rock-salt structure oxide as a type of peroxo O-O bonds. The oxide expands our sight to design high energy Li-ion battery systems.

Chapter 3. Direct visualization of peroxo O-O bond as the oxygen behavior in typical layered Li-rich cathode $Li_{1.2}Ni_{0.2}Mn_{0.6}O_2$

3.1 Introduction

The applications of LIBs are very common in our daily lives, such as mobile phone and electric vehicles.[36-40] With our increasing demand of large energy density, the common LIBs are can't match our requirements.[41-44] Generally, the mechanism of most popular positive electrodes is based on an insertion-extraction process of Li-ion, accompanied by the redox processes of transition metal, such as $LiCoO_2$, $LiFePO_4$, and $LiMn_2O_4$. Their capacity, however, are still limited to no more than 200 mA h g^{-1}, hindering the development of LIBs.[45] To make a balance between supply and demand, the capacity issue should be concerned. Therefore, many researches are focus on searching for a better material which owns high capacity, long cycling life and stable structure.[46]

Recently, $Li_{1.2}Ni_{0.166}Co_{0.067}Mn_{0.567}O_2$ was reported as one typical lithium-rich layered oxides, with higher capacities of more than 250 mA h g^{-1}.[47] The Li-rich materials are well known for their excess capacity beyond the theoretical capacity based on cationic redox process, which have attracted many researcher's attention. There are series of famous compound combing traditional $LiNi_{0.5}Mn_{0.5}O_2$ and typical Li-rich oxide Li_2MnO_3, written as $(1-x)LiNi_{0.5}Mn_{0.5}O_2 \cdot xLi_2MnO_3$, with an equivalent formula $Li[Li_{(1-2x)/3}Ni_xMn_{(2-x)/3}O_2]$ after normalization.[48-50] For these Li-rich oxides, the typical explanation based on cationic redox process is defective. To account for the abnormal phenomenon, a new mechanism based on oxygen activation, therefore, has been proposed. Luo *et al.* pointed out that localized electron holes are formed on oxygen ions with the configuration surrounding by Mn^{4+} and Li^+ in $Li_{1.2}[Ni_{0.13}Co_{0.13}Mn_{0.54}]O_2$.[29] Seo *et al.* depicted that oxygens are easily oxidized due to the Li-O-Li configuration.[27] Sathiya *et al.* observed the reversible peroxo-like species formed in $Li_2Ru_{1-y}Sn_yO_3$.[51]

The researchers provided their observation of oxygen behavior. However, they have no direct especially in-situ evidence to explain the detail pathway of oxygen. McCalla *et al.* visualized the O-O dimers via neutron powder diffraction and transmission electron microscope (TEM) by using Li_2IrO_3 as a model compound and determined the possible limits on the value of *n* for peroxo-like O_2^{n-} dimers (the lower bound $n = 3$ and the upper $n = 3.3$), leading to a further understanding of anionic redox process.[52] Nevertheless, there are also lacking in an in-depth understanding of oxygen evolution and the relationship between the structural and excess capacity in Li-rich layered oxides. Herein, a typical layered Li-rich oxide $Li_{1.2}Ni_{0.2}Mn_{0.6}O_2$ is our target oxide in this chapter. The relationship between charge and discharge curves and structural evolution of this oxide was investigated by in-situ XRD. More importantly, the oxygen activation process was evidenced by in-situ Raman spectroscopy. Results show that the inverse shift of (003) peak during charging has a relationship with oxygen activation, which is confirmed as a type of peroxo O-O bond. What's more, the peroxo O-O bond not only appears in the first cycle, but also clearly emerges in subsequent cycles. Moreover, the peroxo O-O bonds are speculated formed along *c*-axis because the inverse evolution of *c*-axis accompany with the emergence of oxygen activation. Additionally, the density functional theory (DFT) was employed to confirm the possibility of oxygen activation and structural evolution in this case. DFT results are consistent well with our experimental data. Our findings propose a direct evidence of pathway of oxygen evolution, as a type of reversible process of O^{2-}/O^{-}. It helps us to understand the oxygen behavior in Li-rich oxide deeply and provide a guideline for designing the next generation of cathode materials with both cationic and anionic reversible redox process which can deliver substantially high energy density.

3.2 Electrochemical performance of $Li_{1.2}Ni_{0.2}Mn_{0.6}O_2$

3.2.1 Morphology and structure of $Li_{1.2}Ni_{0.2}Mn_{0.6}O_2$

The compound of $Li_{1.2}Ni_{0.2}Mn_{0.6}O_2$ was firstly characterized by SEM companied by its precursor materials, as shown in **Figure 3.1**. SEM images in **Figure 3.1c** reveal that

spheroidal particles with a diameter of around 8 µm are secondary particles formed from primary nanocrystals. [53] The morphology of the particles is inherited from their hydroxide precursors, which can be traced from the same sphere-shape precursors in **Figure 3.1a** and **3.1b**.

To identify the structure of $Li_{1.2}Ni_{0.2}Mn_{0.6}O_2$, powder XRD was performed, as shown in **Figure 3.2a**. The cathode is derived from Li_2MnO_3 by using Ni^{2+} to replace partial Li^+ and Mn^{4+} in TM layers. The XRD pattern coincides well with a monoclinic Li_2MnO_3-like structure with space group C2/m, except some small peaks at ~ 21°. [54]

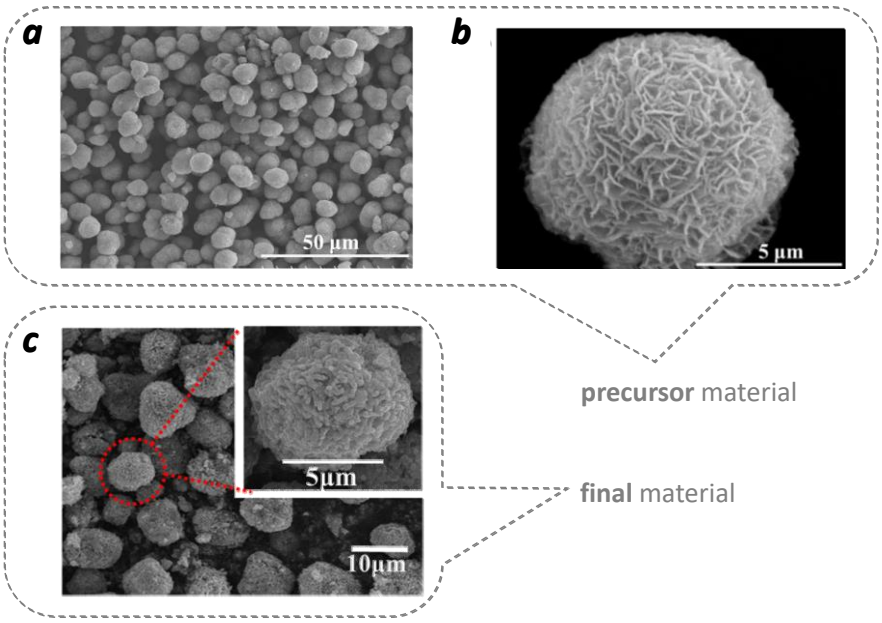

Figure 3. 1 SEM images of precursor in different magnification. a) × 1.0 k and b) × 10.0 k. c) SEM images of final $Li_{1.2}Ni_{0.2}Mn_{0.6}O_2$. The inset shows zoom in image of the particle in red dotted line.

Rietveld refinements of the XRD pattern obtained by GSAS + EXPGUI suite [55-56] successfully give reasonably low χ^2 (2.72) value based on Li_2MnO_3 model. The calculated XRD patterns have a good match with experimental data. The detailed refinement results of lattice parameters are shown in **Table 3.1**. Moreover, there are some additional peaks at ~ 21°, which are the symbol of Li-rich materials, named as superlattice peaks. Speaking simply, the additional peaks caused by the ordered arrangement between Li and TM, as mentioned in **Chapter 1**. In the structure of layered

Li-rich materials, the excess lithium ions occupy the position of transition metals in TM layers, as displayed in **Figure 3.2b**, resulting in the additional peaks in XRD pattern.

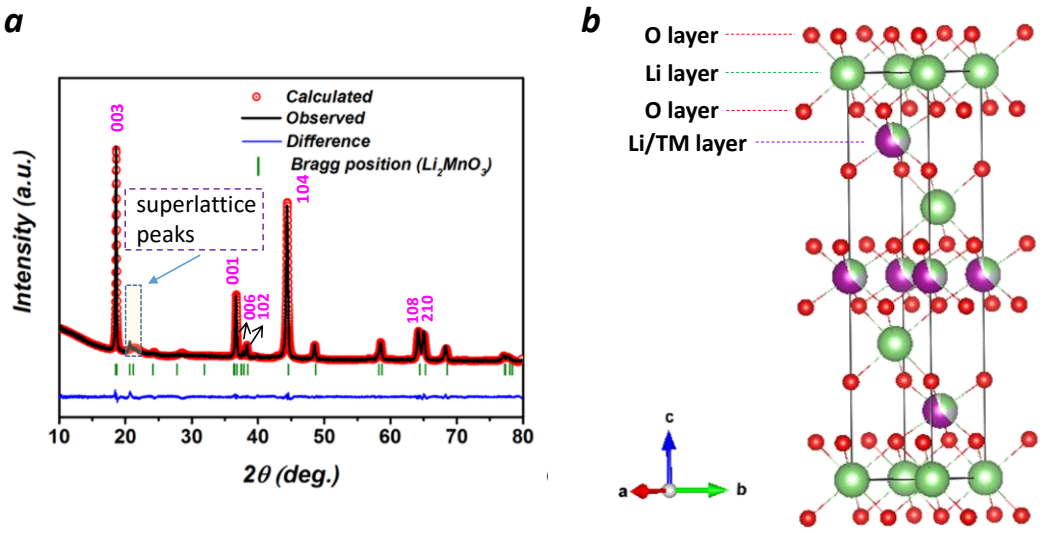

Figure 3. 2 a) XRD pattern of $Li_{1.2}Ni_{0.2}Mn_{0.6}O_2$ with Rietveld refinement. b) The diagram of the crystal $Li_{1.2}Ni_{0.2}Mn_{0.6}O_2$.

Table 3. 1 Crystallographic parameters obtained from the Rietveld refinement for the Li_2MnO_3 (C2/m) phase of $Li_{1.2}Ni_{0.2}Mn_{0.6}O_2$.

Li_2MO_3 (C2/m) Rwp=0.023 Rp=0.017						
a = 4.959 Å, b = 8.284 Å c = 5.037 Å β = 109.07°						
Atom	site	x	y	z	$Occ._{theo}$	$Occ._{refined}$
Mn	4g	0	0.165	0	0.9	0.9
Ni	4g	0	0.165	0	0.1	0.0948
Li	4g	0	0.165	0	0	0.0052
Ni	2c	0	0	0.5	0	0.0020
Li	2c	0	0	0.5	1	0.9980
Ni	4h	0	0.66	0.5	0	0.0036
Li	4h	0	0.66	0.5	1	0.9964
Li	2b	0	0.5	0	0.6	0.5988
Ni	2b	0	0.5	0	0.4	0.4012
O	4i	0.178	0	0.208	1	1
O	8j	0.253	0.320	0.231	1	1

3.2.2 Electrochemical performance of $Li_{1.2}Ni_{0.2}Mn_{0.6}O_2$

The electrochemical tests of as-prepared cathode were performed galvanostatically within the potential window (vs Li/Li^+) of 2.0 V ~ 4.7 V with the current density of 5 mA g^{-1}. **Figure 3.3a** shows the charge-discharge profiles during the first two cycles. The corresponding dQ/dV curves of the first two cycles are also drawn, which can be seen in **Figure 3.4**.

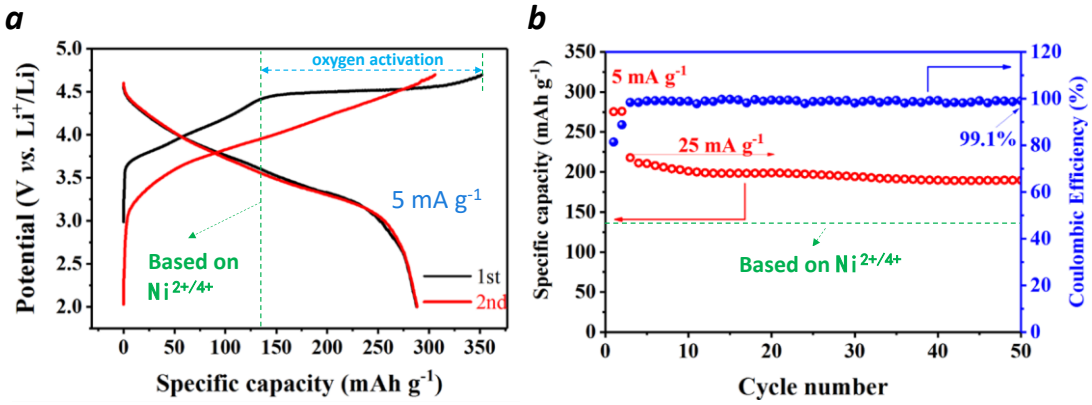

Figure 3. 3 a) Typical charge-discharge profiles for the first two cycles between 2.0 and 4.7 V at 5 mA g^{-1}. b) The cycling performance with coulombic efficiency at 5 mA g^{-1}(first two cycles) and 25 mA g^{-1}(subsequent cycles).

During the first charging process, the peaks in dQ/dV curve located at ~ 3.75 V and 4.2 V are ascribed to the separate oxidation of nickel (from Ni^{2+} to Ni^{3+} and from Ni^{3+} to Ni^{4+}), corresponding to a slope profile in charging curve. A sharp peak appears at ~ 4.5 V, indicating the oxygen activation and corresponding to a plateau in the charging curve. It is reasonable to assume that there have two different processes in initial charging, evidencing by the different slope and plateau curves. The oxide delivers a specific capacity of 350 mA h g^{-1}, corresponding to more than 1.1 extracted Li^+ per formula according to **equation 1.8**. Note that the capacity based on oxidization process of Ni^{2+} to Ni^{4+} is calculated to ~ 130 mA h g^{-1} (corresponding to 0.4 extracted Li^+) which is far less than 350.[50, 57-58] Similarly, the capacity of first discharging is ~ 287 mA h g^{-1}, corresponding to more than 0.9 reinserted Li^+ per formula, leading to about 0.2 Li^+ loss.

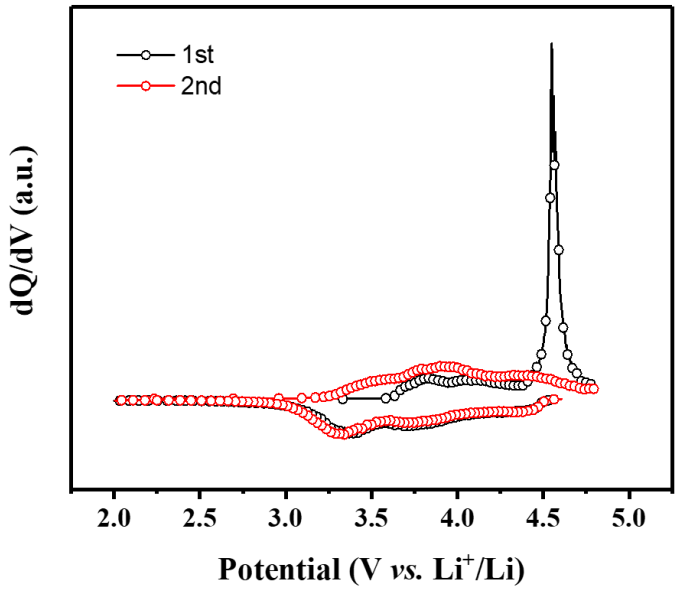

Figure 3. 4 dQ/dV curves for initial two cycles of $Li_{1.2}Ni_{0.2}Mn_{0.6}O_2$ at 5 mA g^{-1}. The black dotted line represents the first cycle and the red dotted line represents the second cycle

Figure 3.3b exhibits cycling performance and coulombic efficiency of this oxide. The capacity retention after 50 cycles is 90.90% at a current density of 25 mA g^{-1} with limited capacity decay. As we mentioned above, the total capacity is far more than that based on Ni-induced redox process. And Mn^{4+} is in its highest valence in the octahedral site and cannot be oxidized further.[45] Herein, to figure out this contradiction, we should firstly understand the relationship between the excess capacity and the evolution of the structure.

3.3 Phase transition in $Li_{1.2}Ni_{0.2}Mn_{0.6}O_2$ during cycling

To unveil the lithiation-delithiation mechanism in $Li_{1.2}Ni_{0.2}Mn_{0.6}O_2$ during cycling processes, in-situ XRD patterns for the first two cycles were performed, as displayed in **Figure 3.5**. The XRD pattern of cathode material assembled in the in-situ cell before the test is also shown in **Figure 3.6**. Most of strong the peaks are belonged to Be and BeO marked by *. However, we only concern the peaks of $Li_{1.2}Ni_{0.2}Mn_{0.6}O_2$. According to Bragg's Law depicted in **Figure 3.7**, an equation is shown as **equation 3.1**,

$$2d\sin\theta = n\lambda \quad (3.1)$$

where d is the interplanar spacing, θ the scattering angle, n an integer number and λ the wavelength. Then we conclude that d has a direct relationship with θ when λ is constant.

$$d = n\lambda/2\sin\theta \quad (3.2)$$

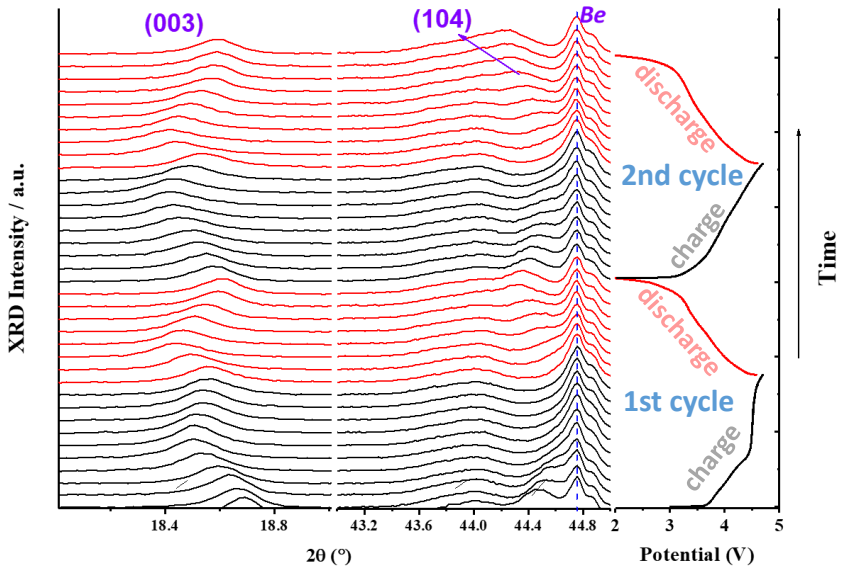

Figure 3. 5 The in-situ XRD patterns of the evolution for the peaks (003) and (104), combined with corresponding electrochemical testing result during the first two cycles for the material $Li_{1.2}Ni_{0.2}Mn_{0.6}O_2$. The black line represents the charge process and the red line represents the discharge process.

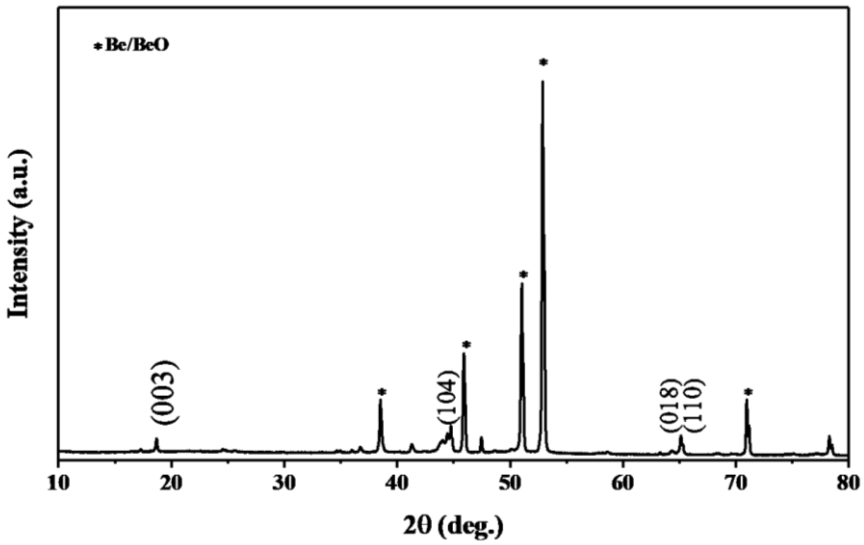

Figure 3. 6 XRD pattern of $Li_{1.2}Ni_{0.2}Mn_{0.6}O_2$ in the in-situ mold. Peaks marked by * belong to Be/BeO.

Note that (003) peak directly reflects the evolution of *c* lattice parameter of the layered oxide. Therefore, it can be used for further understanding of the phase transformation mechanism in the system.

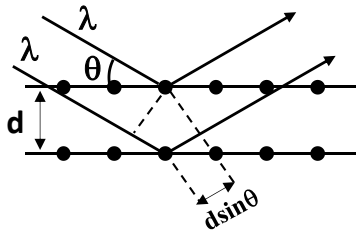

Figure 3. 7 Diagram of Bragg reflection

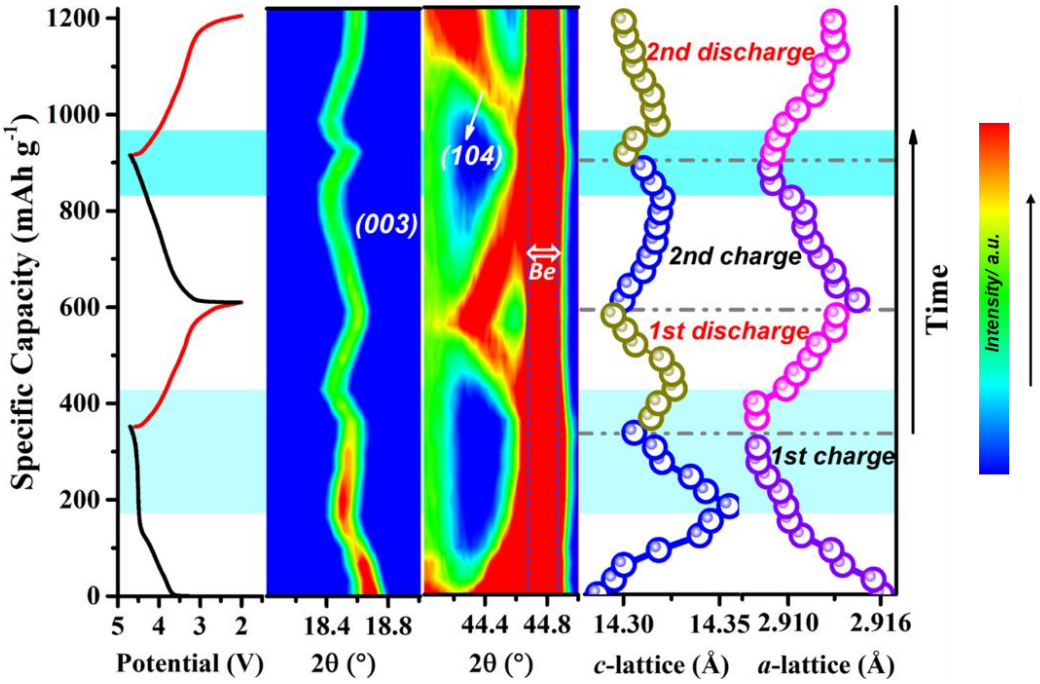

Figure 3. 8 Color-coded images of the peak (003) and (104), refined *c*-lattice, and *a*-lattice parameters during initial two cycles. The range of intensity distribution plots with reference color bar is from 3000 to 5000.

As it can be seen, the evolution of peaks in **Figure 3.7** has a reversible shift during the first two cycles, such as (003) and (104), indicating the reversible electrochemical processer. **Figure 3.8** shows a clearer evolution of XRD patterns companied with charge-discharge curves and refined *a* and *c* lattice parameters for the first two cycles.

As seen clearly, (003) peak shifts to the left continuously during the charging process before 4.5 V (the slope part). The peak then gradually shifts back to the high angle when the charging potential is larger than 4.5 V (the plateau part). The key charging potential here is 4.5 V. The results indicate that *c* lattice value increases at first until the voltage reaches to 4.5 V according to the **equation 3.2**, followed by a sequential decrease. The evolution of peak shift is inverse during discharging process, which has also been clearly shown in **Figure 3.8**. More importantly, the evolution is repeatable even in subsequent cycles.

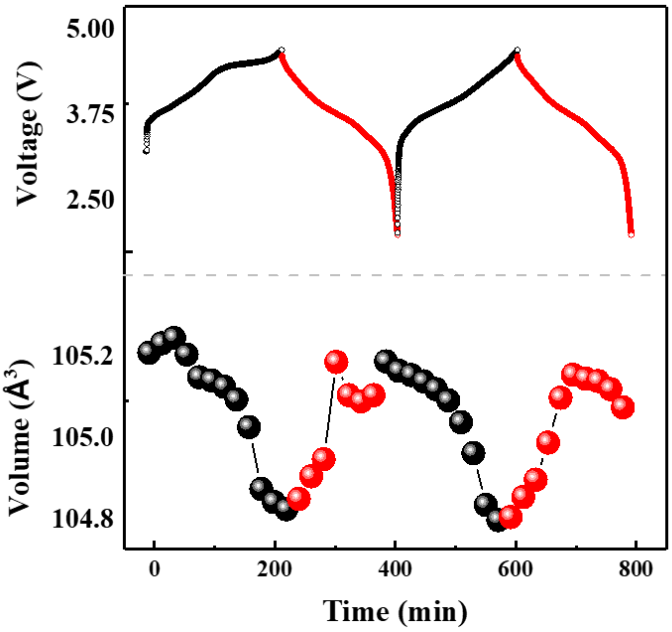

Figure 3. 9 The charging and discharging curves of the first two cycles and changes of the Rietveld refined unit cell volume for $Li_{1.2}Ni_{0.2}Mn_{0.6}O_2$. The black and red colors represent charging and discharging process respectively.

For the reason of structural similarity between Li_2MnO_3 and $LiNi_{0.5}Mn_{0.5}O_2$, a hexagonal unit cell was employed to fit in-situ XRD patterns.[59] The corresponding fitted *a* and *c* lattice parameters for the structure are exhibited in **Figure 3.8**, for the first two cycles, together with corresponding unit cell volume changing shown in **Figure 3.9**. The fitted *a*-lattice parameter decreases at the beginning of charging until the end of charging. While *c*-lattice parameter increases first and then decreases at high potential during charging, as shown in **Figure 3.8**. The change of *c*-lattice parameter

coincides well with the evolution of (003) peak. In the beginning, *a*-parameter decreases may be caused by the reduced ionic radii in TM layers.[45] The electrostatic repulsion between oxygen slabs increases while Li-ions extract from Li layered sites, accounting for an extended *c*-axis of the unit cell, corresponding to the shift of (003) to lower angles.[60] When charging to ~ 4.5 V, the plateau appears, indicating a different electrochemical process emerges, which can be also revealed by the smooth change of *c*-parameter and *a*-parameter. It is a reasonable speculate that Li-ions begin to extract from TM slabs at this region, leading to an inverse shift of (003) peak. The variation is consistent with the previous work. [61] During discharging process, (003) and (104) peak show a reversed evolution, indicating some opposite processes happens compared with charging. Note that the evolution of the peaks is reversible in the second cycle, compared to the first cycle, indicating an analogous Li-extracted/inserted mechanism, which is consistent well with the discussion above. The phenomenon at high potential is very interesting, both for the oxygen activation plateau at the first charge curve and evolution of (003) peak in in-situ XRD patterns. So, we focus our attention on this high potential.

3.4 Oxygen behavior in $Li_{1.2}Ni_{0.2}Mn_{0.6}O_2$

3.4.1 Raman spectra of $Li_{1.2}Ni_{0.2}Mn_{0.6}O_2$ during cycling

Surface-enhanced Raman spectra was employed in this test.[62, 63] The higher capacity in Li-rich oxides is reasonably ascribed to the oxygen-related anionic electrochemical process.[29, 64-65] Thus, in-situ Raman was utilized as a powerful tool to investigate the oxygen redox behaviors,[62, 66] the results are shown in **Figure 3.10**, with charge/discharge curves for the first two cycles. Moreover, wider Raman shift region is also shown in **Figure 3.11**. In this figure, there is one good reference peak (Li_2CO_3) for basically entire measurements. The peak of Li_2CO_3 appears at ~ 1080 cm^{-1} during the charging process and then exists the whole measurements without Raman shift, which can be a good reference peak.[62, 67] In addition to the overlapping stretching modes in MO_6 octahedron (below 700 cm^{-1}),[68] the variation trend of several novel

peaks become noteworthy during cycling. When charging to ~ 4.5 V, one sharp peak emerges, locating at 953 cm^{-1}, which is due to the adsorption of the anion in perchlorate salt (ClO_4^- symmetric stretching).[66] The related peak has a relationship with potential, because its intensity quickly reaches maximum value due to the saturation of adsorption and disappears in discharging process.

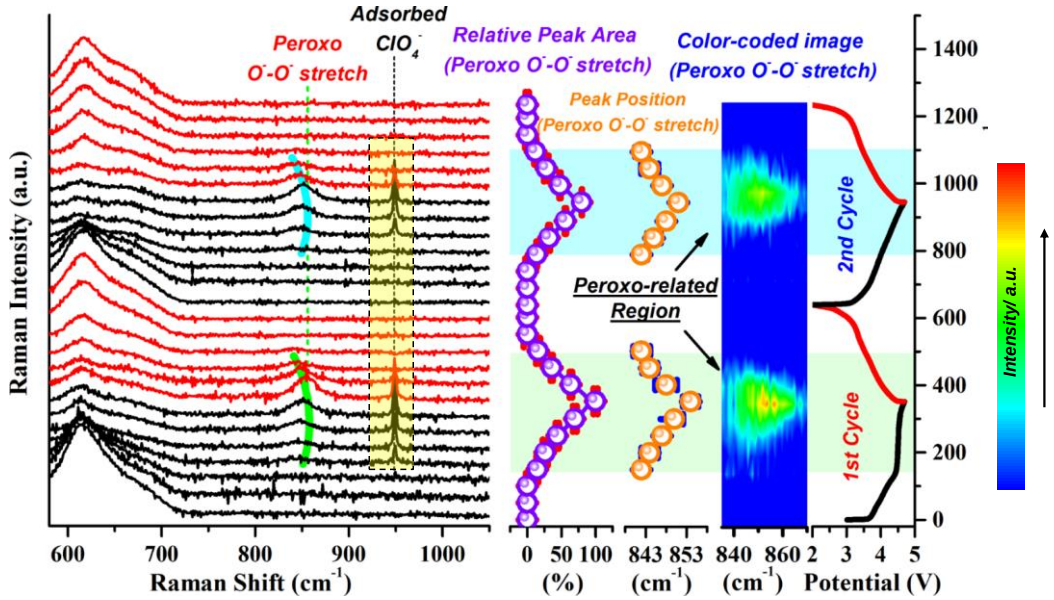

Figure 3. 10 Capacity dependent in situ Raman spectra recorded during initial two galvanostatic cycles (5 mA g^{-1}). The novel peroxo-species peak has been highlighted, and corresponding capacity dependence of peak area (purple hollow), peak position (orange hollow) and color-coded image are summarized, respectively. The range of intensity distribution plots with reference color bar is from 0 to 0.03. The related voltage profiles are shown for clarity.

Besides, the unique adsorption feature can be further proved by the potential-dependent dropping trend during discharging. The change of unique adsorbed ClO_4^- peak is a function of potential. There is no relationship between O^-–O^- peak and adsorbed ClO_4^- peak, which can be confirmed by an aging test. As shown in **Figure 3.12**, we stopped the procedure and let the cell free at the end of charging process. The variation of Raman intensity of O^-–O^- peak and ClO_4^- peak are obvious in **Figure 3.12a** and more distinct in **Figure 3.12b**. The intensity of ClO_4^- peak decreases dramatically as a function of aging time, resulting from the essential reason-decrease of the potential.

The intensity of $O^{-}-O^{-}$ peak, however, basically remain unchanged with aging time.

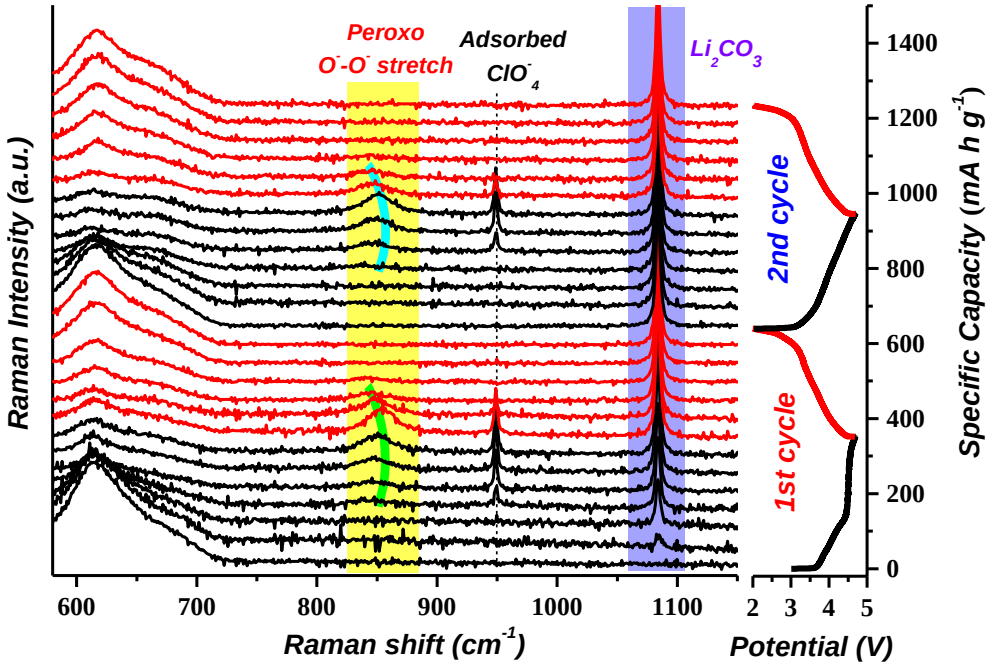

Figure 3. 11 In situ Raman spectra (SERS-signal) recorded during initial two galvanostatic cycles with extended Raman shift range, which includes Li_2CO_3-related peak (~1080 cm^{-1}) as comparison. Note that, the formation of carbonate species would be rationally ascribed to the parasitic reaction between electrolyte and other active oxygen-related species (superoxide anion radical and/or oxygen), which release from the lattice ($Li_{1.2}Ni_{0.2}Mn_{0.6}O_2$) upon charging (irreversible oxygen loss). This parasitic accumulation of Li_2CO_3 is also well coincide with previous reports.[67, 69]

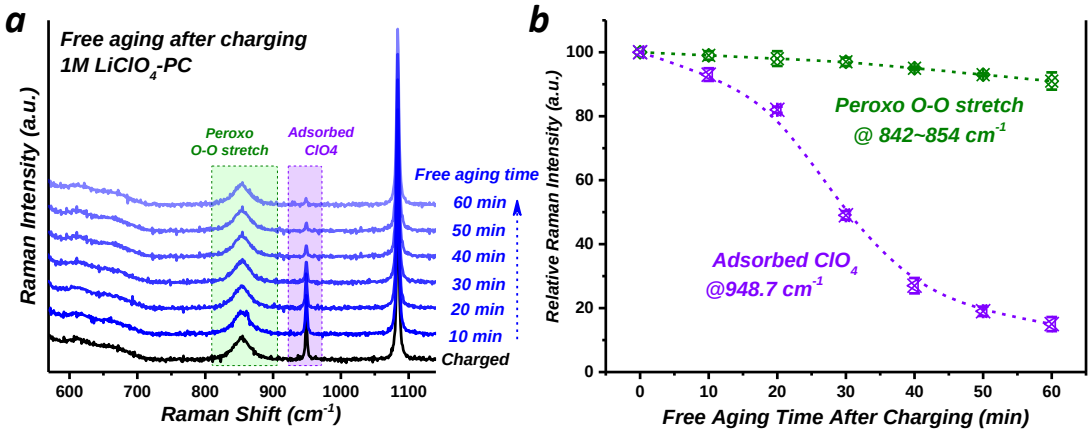

Figure 3. 12 Aging time test of $O^{-}-O^{-}$ peak and ClO_4^{-} peak after charging. a) Changes of Raman intensity with aging time and b) relative Raman intensity with aging time.

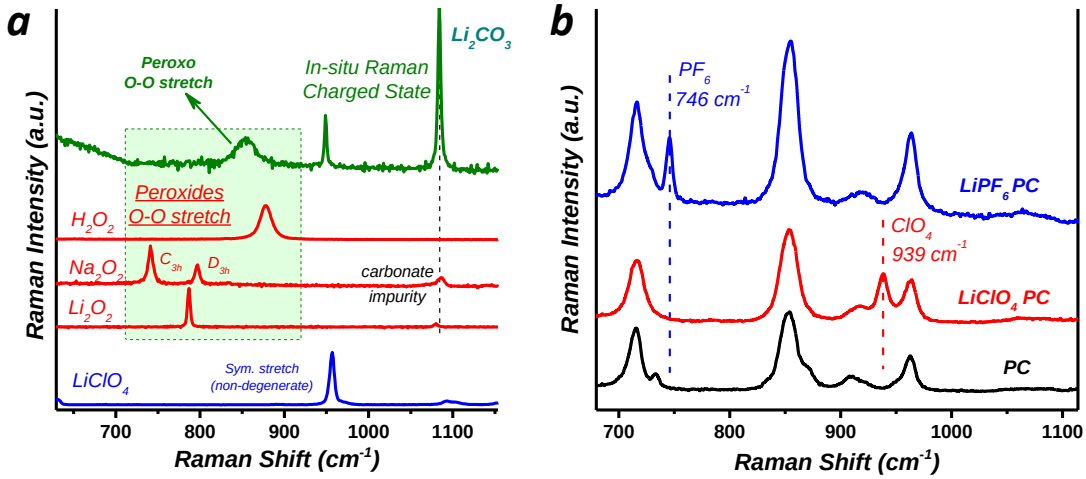

Figure 3. 13 Raman peaks of standard materials of a) $LiClO_4$, Li_2O_2, Na_2O_2, H_2O_2, and charged state electrode and b) PC, electrolyte of 1M $LiClO_4$ in PC and electrolyte of 1M $LiPF_6$ in PC.

More importantly, a new peak at ~ 850 cm^{-1} emerges when charging to ~ 4.5 V and increases at this region in **Figure 3.10**. The peak gradually disappears with the subsequent discharge process. From **Figure 3.13**, we can know that this peak locates at the typical peroxo O^{-}–O^{-} stretch region (700-900 cm^{-1}) in peroxo-species.[29, 66] The potential of O^{-}–O^{-} peroxo bond appearance (for $Li_{1.2}Ni_{0.2}Mn_{0.6}O_2$ is ~ 4.5 V) would be different in other systems arising from different thermodynamic conditions, which means the environment (such as neighboured atoms, space group) surrounding oxygen atoms.[31, 70-73] The reversible variation trend of the peroxo O^{-}–O^{-} bond can also be observed on specific high voltage plateau during the 2nd cycle. The average concentration of peroxo O^{-}–O^{-} bond can be represented by relative peak area which is also shown in **Figure 3.10**. Before the charging plateau of ~ 4.5 V, there are no peroxo O^{-}–O^{-} bond and relative peak area appears, after which the bond appears and then increases gradually to the maximum corresponding to the end of charging as a function of time. In discharge process, the area decreases to zero subsequently and exhibits a reversible evolution during the 2nd cycle. Moreover, the formation of the newly-proposed peroxo O^{-}–O^{-} bond can be resulted from the extracted-Li from Li/TM layer according to the obtained XRD results (**Figure 3.8**). During charging at 4.5 V plateau, peroxo O^{-}–O^{-} stretch appears and shifts to higher wavenumber, indicating the decrease

of peroxo $O^{-}-O^{-}$ bond length in peroxo-species.[61] As a reference of peroxo $O^{-}-O^{-}$ bond length (1.28 Å in Li_2O_2 where peroxo $O^{-}-O^{-}$ bond located at 790 cm^{-1} and 1.48 Å in H_2O_2 where peroxo $O^{-}-O^{-}$ bond located at 878 cm^{-1}), the bond length range in $Li_{1.2}Ni_{0.2}Mn_{0.6}O_2$ can be empirically considered as 1.28 Å ~ 1.48 Å.[74-75] Moreover, the peroxo $O^{-}-O^{-}$ bond tends to be formed along the *c*-axis (not in *ab* plane), combining with the decreasing trend of *c*-axis length during ~ 4.5 V plateau (**Figure 3.8**), which is also consistent well with the mechanism proposed by related DFT simulations.[76] In this case, the causality among Li extraction/insertion, the variation of *c*-axis and the formation/decomposition of peroxo $O^{-}-O^{-}$ bond can be rationally unified together. Consequently, the operando observation and assignment of real peroxo $O^{-}-O^{-}$ bond in typical layered Li-rich oxide provides new and direct evidence for the reversible anionic redox chemistry and detail pathway of oxygen behavior for understanding Li-rich cathode materials, which is essentially different from the peroxo-like $(O_2)^{n-}$-based redox process proposed by previous ex-situ XPS analysis.[51, 64, 77]

The phenomenon of adsorbed ClO_4^- peak coupled with peroxide species in **Figure 3.10**, however, made a confusion because it seems ClO_4^- may be an additional source for $O^{-}-O^{-}$ dimers. We have confirmed that the adsorbed ClO_4^- peak is potential-dependent and has no relationship with $O^{-}-O^{-}$ bonding. Furthermore, we did a similar experiment in $LiPF_6$ (1M in PC) and a similar phenomenon appears in **Figure 3.14**. A new peak ($O^{-}-O^{-}$) at ~ 850 cm^{-1} emerges and increases during the 4.5 V-related charging plateau, and gradually disappears with the subsequent discharge process, similar to the phenomenon in $LiClO_4$-salt electrolyte. Another similar phenomenon is that a new peak at ~ 1080 cm^{-1} emerges and increases during the charging process and without decrease even in discharging process, which can be assigned to Li_2CO_3. Moreover, the adsorbed PF_6^- peak appears until the end of charging process, which is also potential-dependent.

There is one more question: what is the result if we don't employ SERS? The Raman spectroscopy data without nanoparticles is also shown in **Figure 3.15**. No peaks can be seen in the peroxo $O^{-}-O^{-}$ stretch region the whole charging and discharging process if

without nanoparticles. We know that SERS is always employed by covering silver or gold on the surface of target. The laser will excite surface plasmons of silver and gold, then the electric fields surrounding the metal increase significantly. Given that Raman intensities are proportional to the electric field, there is a considerable increase in the obtained signal. [78-79] And this may be the reason why there is no Raman signal of oxygen bonds in other's paper.

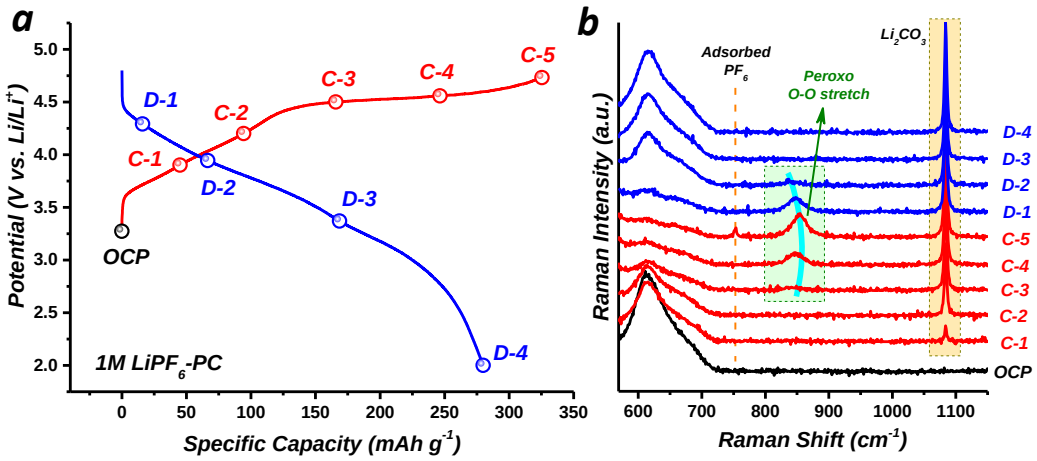

Figure 3. 14 a) Typical charge-discharge profiles between 2.0 and 4.7 V with electrolyte of 1M $LiPF_6$ in PC at 10 mA g^{-1} and b) in situ Raman spectra recorded during initial galvanostatic cycle.

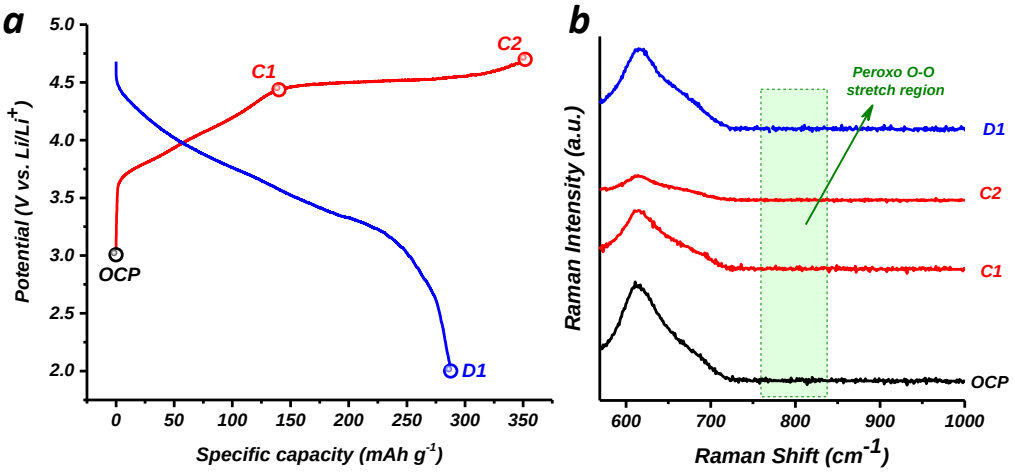

Figure 3. 15 a) Typical charge-discharge profiles between 2.0 and 4.7 V with electrolyte of 1M $LiClO_4$ in PC at 10 mA g^{-1} and b) in situ Raman spectra without nanoparticles recorded during initial galvanostatic cycle.

3.4.2 XPS analysis of $Li_{1.2}Ni_{0.2}Mn_{0.6}O_2$

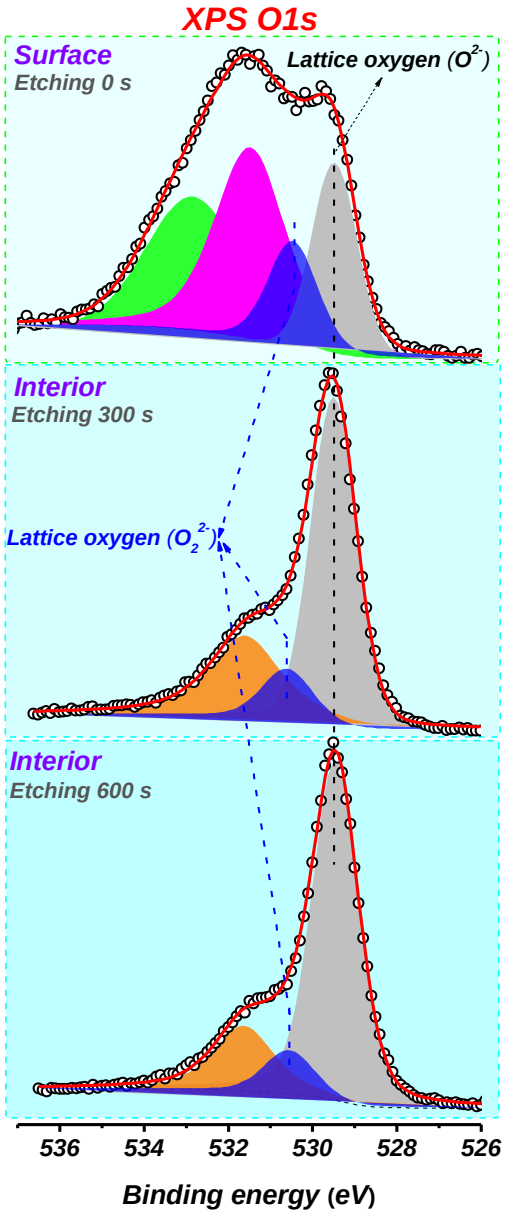

Figure 3. 16 Oxygen 1s XPS spectra of the charged $Li_{1.2}Ni_{0.2}Mn_{0.6}O_2$ electrode at 4.7 V, which were collected in the surface, after Ar^+ etching 300 s and 600 s. The grey, blue, green, and pink areas represent the lattice oxygen (O^{2-}), lattice oxygen (O_2^{2-}), surface deposited species and electrolyte oxidation, respectivily. The brown area may be caused by the oxygen deficiencies.

XPS is another powerful tool to analyze oxygen behavior. Moreover, to understand the formation of O^-–O^- dimers in the bulk or in the surface, depth analysis was employed etching experiment. Result reveals that the peroxo O^-–O^- bond exists both

in the surface and in the bulk (**Figure 3.16**). XPS spectra were obtained from the surface of the charged electrode at 4.7 V and that after different times of Ar^+-sputtering. Before etching by argon sputtering, peaks were observed at ~ 529.5 eV, 530.5 eV, 531.5 eV, and 532.8 eV which are assigned to lattice oxygen (O^{2-}), lattice oxygen (O_2^{2-}), surface deposited species and electrolyte oxidation, respectively. The peaks and their positions are consistent well with Tarascon and co-authors' works.[31, 51-52, 64] After argon sputtering, the peak assigned to electrolyte oxidation disappears. The spectrum after etching 300 s is as same as that after etching 600 s, meaning the internal structure was obtained after sputtering 300 s. Obviously, the peak located at 530.5 eV (bule area) can be clearly seen after sputtering, which is assigned to peroxy oxygen dimers (the brown area may be caused by the oxygen deficiencies[80-81]). Herein, the peroxo oxygen dimers exist both in surface and in internal. Note that, the composition of the electrode may change after sputtering, however, the result can be reliable after some concessions we made in etching time and pattern quality.[82]

3.5 DFT calculations for $Li_{1.2}Ni_{0.2}Mn_{0.6}O_2$

3.5.1 DFT calculation model

Lithium honeycomb ordering is common in many lithium-excess compounds, corresponding to the additional superlattice peaks in XRD pattern. However, the honeycomb structure is short-range order because of the non-uniform distribution of the cations (Li, Ni, Mn) in transition metal layers.[57] It means that there exist mixed ordering types such as honeycomb-type and straight-type in transition metal layers.[57, 83] Here, we present the detailed reasons why we chose the straight-type model for first principle calculation, after considering the several configurations in transition-metal layers.

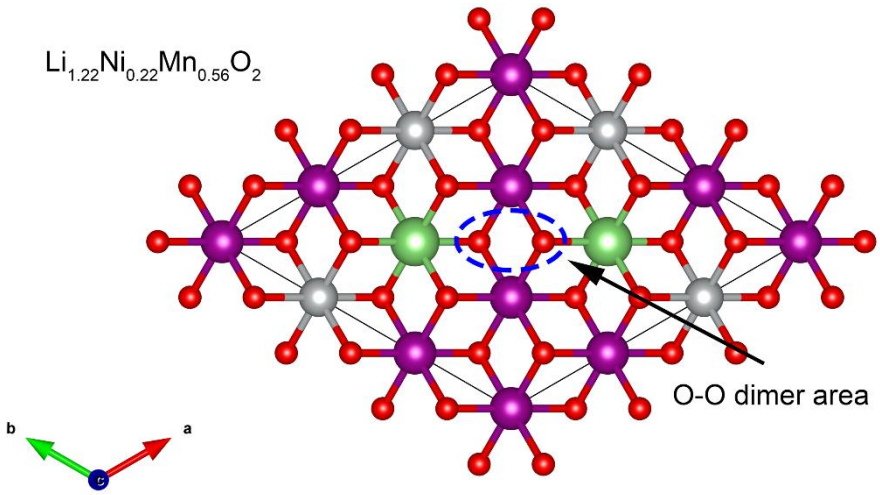

Figure 3. 17 Honeycomb ordering of Li atoms in the transition metal layer of lithium-excess $Li_{1.22}Ni_{0.22}Mn_{0.56}O_2$ compound. The white, purple, green and red spheres represent Li, Mn, Ni and O atoms, respectively.

In our calculations, the honeycomb type ordering of excess lithium atoms was studied. Considering the balance between computing workloads and the accuracy of the calculation model, a lithium honeycomb type ordering structure with the composition of $Li_{1.22}Ni_{0.22}Mn_{0.56}O_2$ is built, as shown in **Figure 3.17**. Although the composition of $Li_{1.22}Ni_{0.22}Mn_{0.56}O_2$ is slightly different from our experimental $Li_{1.2}Ni_{0.2}Mn_{0.6}O_2$, it can well represent the local honeycomb ordering of lithium atoms in $Li_{1.2}Ni_{0.2}Mn_{0.6}O_2$. Thus, we investigated the peroxo bond formation in the fully delithiated $Li_{1.22}Ni_{0.22}Mn_{0.56}O_2$ compound, whose honeycomb ordered Li atom in transition metal layer are fully extracted to represent the charging final structure. The corresponding energy barrier of the peroxo bond formation in it is depicted in **Figure 3.18**. It can be seen that forming a peroxo bond with the O^{-}–O^{-} bond length less than 1.46 Å (a typical value of peroxo bond)[84] in this lithium honeycomb type structure is endothermic, more than 1 eV ~ 96 KJ mol^{-1}, and needs to overcome a very large energy barrier of 1.44 eV. Such high energy barriers of peroxo bond formation also can be found in Li_2MnO_3 compounds, 0.6 - 1 eV.[84] Generally, the thermal vibration energy of an atom is KT, ~ 0.026 eV at 300 K, which is far less than the energy barrier for the peroxo bond

formation, so the possibility of forming peroxo bonds in the lithium-excess compounds with the local lithium honeycomb type structure in $Li_{1.2}Ni_{0.2}Mn_{0.6}O_2$ during the charging and discharging process at room environment is extremely low.

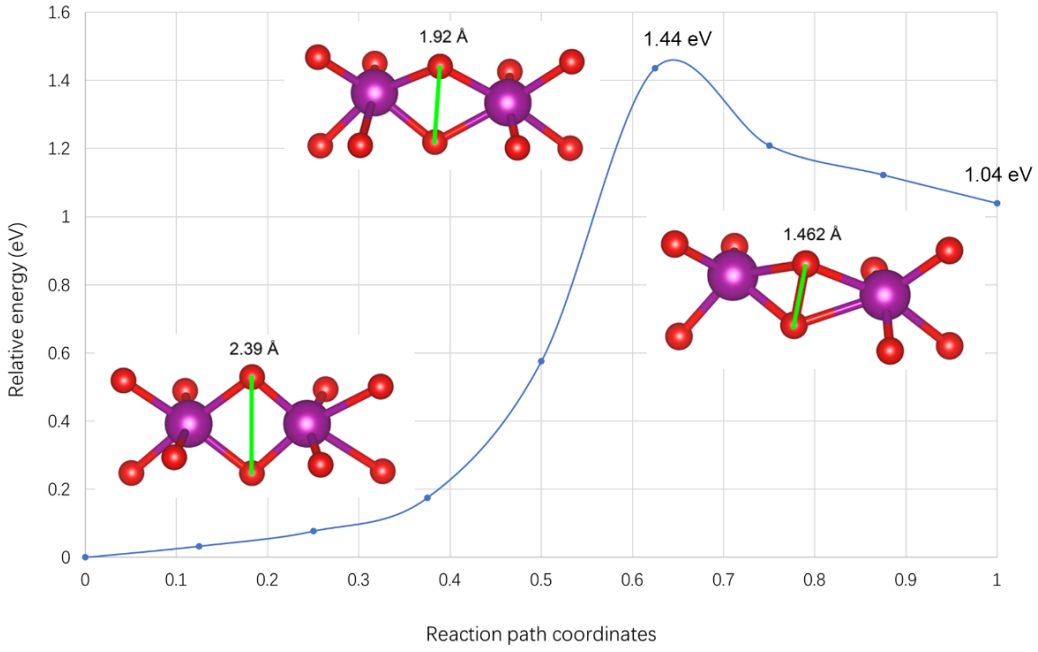

Figure 3. 18 Energy barrier (eV) of the peroxy bond formation in fully delithiated $Li_{1.22}Ni_{0.22}Mn_{0.56}O_2$ compound with honeycomb orderings of Li atoms at the end of charging (Insets are the local structures for peroxo bond formation, including initial structure, transition state structure and final structure).

We calculated the relative energy of some other $Li_{1.2}Ni_{0.2}Mn_{0.6}O_2$ structures with different lithium atom orderings in the transition metal layer, as shown in **Figure 3.19**. Refer to the case 1 with dispersive lithium atom orderings, the relative energy of case 5 structure with local lithium straight-type tripolymers is 35.45 meV $atom^{-1}$, slightly more than the room temperature atom thermal vibration energy ~26 meV $atom^{-1}$, but far less than the high temperature atom thermal vibration energy ~101.67 meV $atom^{-1}$ at the synthesizing temperature of 900 °C. Therefore, the lithium straight-type tripolymers in some local areas of our experimental case are highly possible, and they are also observed in some other lithium-excess compounds, such as $Li_{1.15}Ni_{0.47}Sb_{0.38}O_2$.[83]

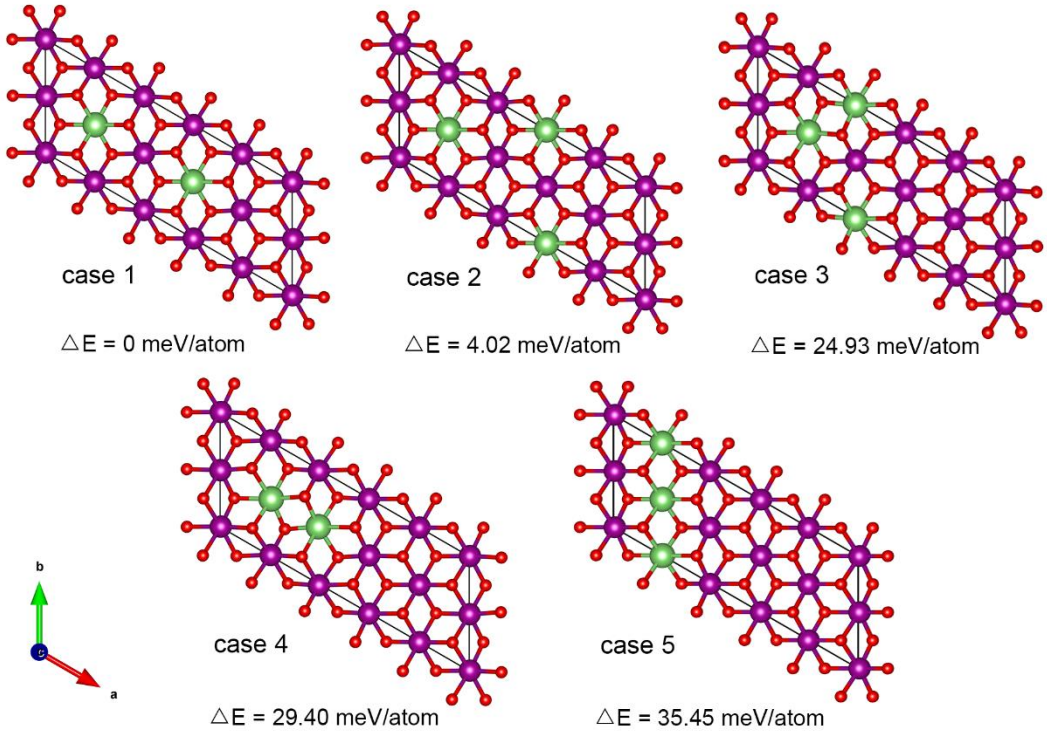

Figure 3. 19 The relative energy (in meV/atom, and referred to case 1) of $Li_{1.2}Ni_{0.2}Mn_{0.6}O_2$ compounds with different lithium atom orderings in the transition metal layer.

In addition, we have investigated the peroxo bond formation in these $Li_{1.2}Ni_{0.2}Mn_{0.6}O_2$ structures in **Figure 3.19**. Similarly, forming peroxy bonds in these structures are difficult with larger energy barriers compared to straight-type tripolymer structure. While the local lithium straight-type tripolymers model (**Figure 3.20**) is beneficial for the formation of peroxy bonds without energy barrier, which is a spontaneous exothermic process. Therefore, the local lithium straight-type tripolymers model in DFT calculations can explain the formation and evolution of peroxy bonds during the charging and discharging process of our experiment.

All calculations were carried out by using the projector augmented wave (PAW) method[85] in the framework of DFT[86], as implemented in the Vienna *ab-initio* Simulation Package (VASP). The generalized gradient approximation (GGA)[87] and Perdew–Burke–Ernzerhof (PBE) exchange functional[86] was used. The periodic boundary condition approach was used. The plane-wave energy cutoff was set to 450 eV. The Monkhorst–Pack method[88] with 1×4×1 *k*-points mesh was employed for the

Brillouin zone sampling of the structural relaxations of $Li_{1.2-x}Ni_{0.2}Mn_{0.6}O_2$. The convergence criterions of the energy and force were 10^{-4} eV/atom and 0.05 eV $Å^{-1}$, respectively.

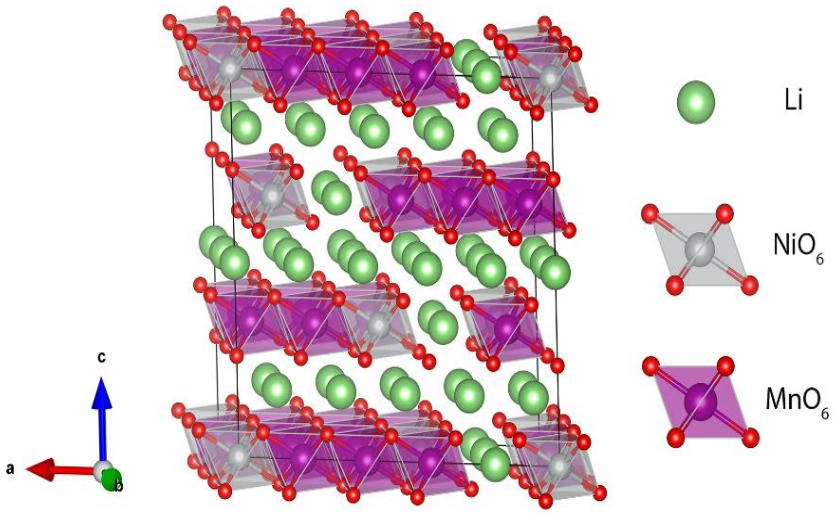

Figure 3. 20 The optimized crystal structure of $Li_{1.2}Ni_{0.2}Mn_{0.6}O_2$. The green, silver, purple and red spheres represent Li, Ni, Mn and O atoms, respectively.

3.5.2 Results of DFT calculations for $Li_{1.2}Ni_{0.2}Mn_{0.6}O_2$

There are many forms of oxygen behavior, including the typical irreversible oxygen loss in the Li-rich materials, such as the formation of O_2, O_2^-. [29-30, 67] Our observation of a reversible oxygen behavior with the generation of O_2^{2-} dimers is different. Moreover, the oxygen activation is sustainable in the subsequent cycle. Furthermore, the first-principle calculations for the $Li_{1.2-x}Ni_{0.2}Mn_{0.6}O_2$ systems have been performed to better understand the formation of the peroxo O^-–O^- bond during cycling. The excess lithium ordering in the transition metal layer of $Li_{1.2}Ni_{0.2}Mn_{0.6}O_2$ is very complicated, which mixed with other different types of local ordering.[89-91] However, the $Li_{1.2}Ni_{0.2}Mn_{0.6}O_2$ with honeycomb ordering of excess lithium atoms experiences an energy barrier of 1.4 eV for the formation of peroxo bonds, compared to 0.6-1 eV of Li_2MnO_3,[84] which is not realistic to occur during the room temperature cycling (see **Figure 3.17 - Figure 3.19** for detailed discussions). Here, we are especially interested

in $Li_{1.2}Ni_{0.2}Mn_{0.6}O_2$ with local straight-type tripolymers (**Figure 3.20**), where the formation of peroxo bonds experiences no energy barrier during charging.

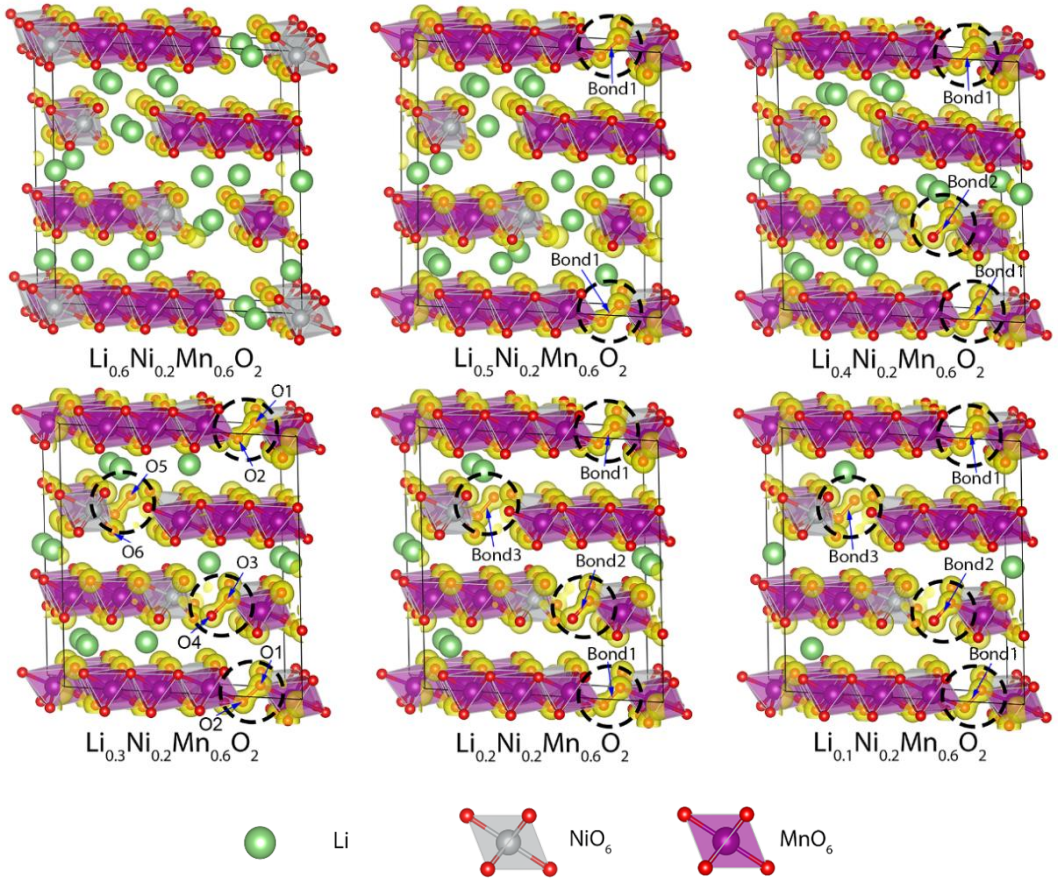

Figure 3. 21 Charge density distributions (yellow isosurfaces = 0.2 e $Å^{-3}$) of the $Li_{1.2-x}Ni_{0.2}Mn_{0.6}O_2$ systems (x = 0.6, 0.7, 0.8, 0.9, 1.0 and 1.1) with peroxo O-O bonds (in black dotting circles) during the charging and discharging processes.

Thus, the $Li_{1.2}Ni_{0.2}Mn_{0.6}O_2$ crystal structure was built using a 5×2×1 supercell of the $R\bar{3}m$ $LiMnO_2$ with local straight type. Partial Mn atoms are replaced by Ni and Li atoms (**Figure 3.20**). Firstly, the $Li_{1.2}Ni_{0.2}Mn_{0.6}O_2$ crystal structure was relaxed, and the optimized lattice parameters of $Li_{1.2}Ni_{0.2}Mn_{0.6}O_2$ unit cell are a = 14.49 Å, b = 5.81 Å and c = 14.26 Å, respectively, which coincides well with our XRD refinement results. Then, the crystal structures and atomic positions of the different charge states of $Li_{1.2-x}Ni_{0.2}Mn_{0.6}O_2$ systems (x = 0.6, 0.7, 0.8, 0.9, 1.0 and 1.1) were relaxed. The corresponding charge density distributions were also shown in **Figure 3.21**. Lithium

atoms in lithium layers are preferentially divorced from the $Li_{1.2-x}Ni_{0.2}Mn_{0.6}O_2$ cathode during the initial charging process (x from 0 to 0.6), without any observation of peroxo O-O bond. When charging to high potential of ~ 4.5 V (i.e., x = 0.7), some excess lithium atoms in the TM-layers begin to extract from the structure, and two adjacent O atoms of the MnO_6 octahedron near the excess lithium vacancies get closer to each other.

Table 3. 2 The peroxo O-O bond length (in Å) of the $Li_{1.2-x}Ni_{0.2}Mn_{0.6}O_2$ systems (x = 0.6, 0.7, 0.8, 0.9, 1.0 and 1.1) during the charging and discharging processes

	O-O bond1	O-O bond2	O-O bond3
$Li_{0.6}Ni_{0.2}Mn_{0.6}O_2$	\	\	\
$Li_{0.5}Ni_{0.2}Mn_{0.6}O_2$	1.343	\	\
$Li_{0.4}Ni_{0.2}Mn_{0.6}O_2$	1.315	1.415	\
$Li_{0.3}Ni_{0.2}Mn_{0.6}O_2$	1.314	1.348	1.350
$Li_{0.2}Ni_{0.2}Mn_{0.6}O_2$	1.306	1.308	1.341
$Li_{0.1}Ni_{0.2}Mn_{0.6}O_2$	1.305	1.307	1.310

Moreover, remarkable electrons between these two closer O atoms can be observed (yellow isosurfaces in black dotting circles), demonstrating the formation of O^{-}–O^{-} covalent bond. The corresponding bond length is calculated to be 1.343 Å (**Table 3.2**), which is much shorter than 2.6 Å of interatomic distance between adjacent O atoms in MnO_6 octahedrons, and even shorter than 1.49 Å of the peroxo O^{-}–O^{-} bond length in Li-rich Li_2MnO_3 system[84]. The Bader charge represents charges transfer of one atom, which is shown in **Figure 3.22.** The O atomic charges of the special O^{-}–O^{-} bond in $Li_{0.5}Ni_{0.2}Mn_{0.6}O_2$ cathode are larger than those in $Li_{0.6}Ni_{0.2}Mn_{0.6}O_2$ and other O atoms far from the excess lithium vacancies. All these evidence indicate the formation of the peroxo O^{-}–O^{-} bond between x = 0.6 and 0.7, corresponding to the specific capacity between 190 and 220 mA h g^{-1}, which is consistent with the in-situ Raman spectra data.

During the final charging period (x = 0.8 to 1.1), more and more peroxo O^{-}–O^{-} bonds form with smaller bond lengths and more positive O atomic charges, which is also consistent with the variation trend of Raman shift and relative peak area of O^{-}–O^{-} bonds in our in-situ Raman spectra data.

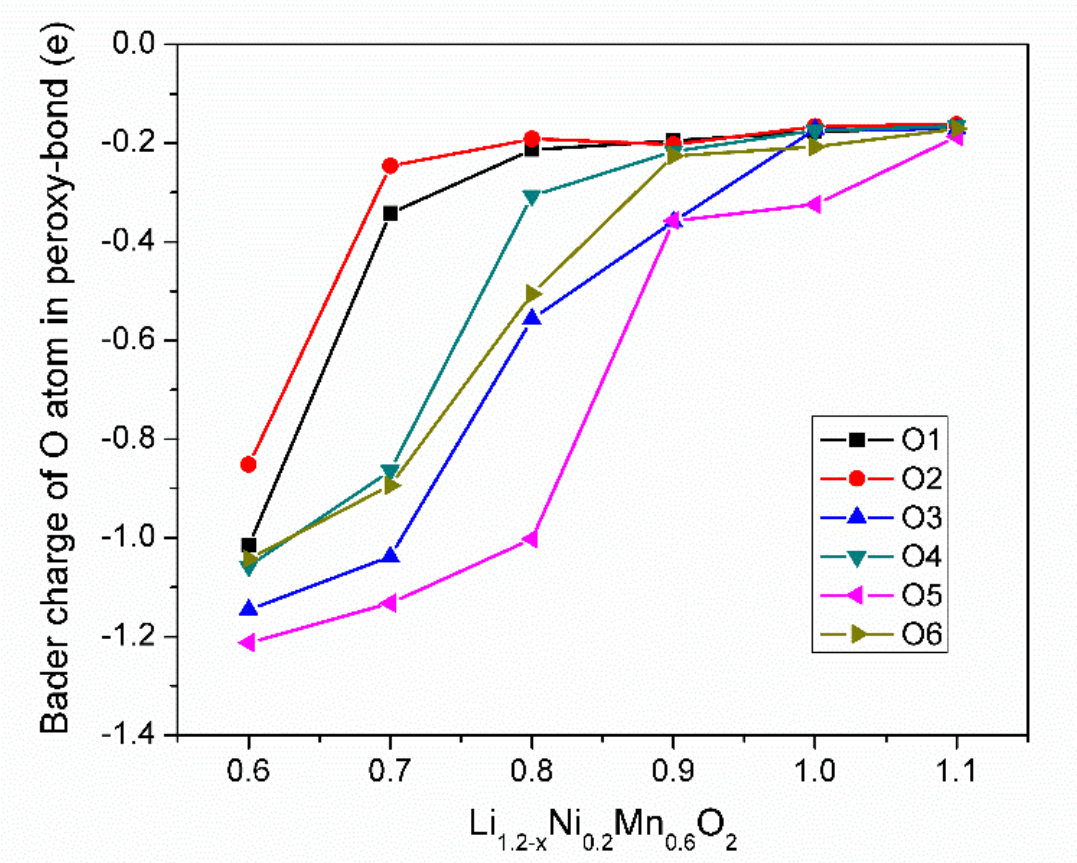

Figure 3. 22 Atomic Bader charge (e) of the peroxo O-O bonds of the $Li_{1.2-x}Ni_{0.2}Mn_{0.6}O_2$ systems (x = 0.6, 0.7, 0.8, 0.9, 1.0 and 1.1) during the charging and discharging processes

3.6 Summary and conclusions

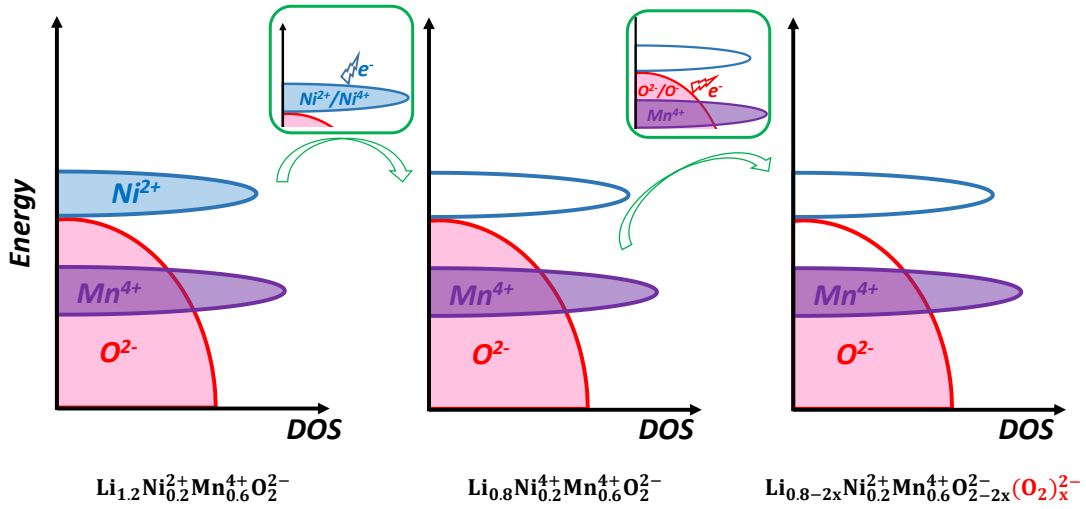

Figure 3. 23 Schematic representation of the density of states (DOS) of $Li_{1.2}Ni_{0.2}Mn_{0.6}O_2$ during charge process.

Here we can summarize some discussions as follows:

Firstly, during charging process before 4.5 V, Li-ions extract from Li-layers accompanied by the oxidization process of $Ni^{2+/4+}$, corresponding to ~ 130 mA h g^{-1}. And then, oxygen activation occurs till the end of the charging because both Ni and Mn are in their highest valence in the octahedral site.[92] Oxygen activation becomes the main resource for charge compensation at the plateau of ~ 4.5 V. There are 1.2 Li^+ per formula in $Li_{1.2}Ni_{0.2}Mn_{0.6}O_2$ and there will be 1.1 Li^+ extracted from the structure, indicating that Li+ can be extracted from both Li-layers and TM-layers. The different two processes represent the smooth shift of *c*-lattice parameter to lower value firstly and then to higher value at charging process. The participation of Ni^{2+} and oxygen involvement during the charging process are shown **Figure 3.23**. The redox of Ni and oxygen behavior also account for the charge compensation during discharging process. The changes of *c*-lattice parameter show a cooperation effect including the reinsertion of Li^+ into the structure, the reduction of Ni, and the reversible anionic (O^-/O^{2-}) redox process. Moreover, combining the changes of peroxo O^{-}–O^{-} bond length in Raman results with the variation tendency of *c*-axis length in XRD results, the formation of

peroxo $O^{-}-O^{-}$ bond is speculated along the *c*-axis, which is also confirmed by the DFT calculations.

Corresponding conclusions are shown here:

A typical layered L-rich oxide $Li_{1.2}Ni_{0.2}Mn_{0.6}O_2$ was systematically studied. We directly visualize the structural evolution and oxygen activation which as a form of peroxo $O^{-}-O^{-}$ bond. Oxygen activation has the responsible of high capacity in Li-rich oxides. The accompanied extracted Li-ions have a relationship with *c* axis and the reversible anionic redox process, which are consistent well with the DFT calculations. Moreover, both cationic and anionic redox processes are reversible even in subsequent cycles. The findings provide new direct evidence for the reversible oxygen activation process in layered Li-rich oxides and pave a new way to understand the intercalation chemistry and design Li-rich layered oxides with high performance.

Chapter 4. A new type Li-rich rock-salt oxide $Li_2Ni_{1/3}Ru_{2/3}O_3$ with reversible oxygen activation

4.1 Introduction

LIBs have been applied successfully in our daily lives.[93] They are very common in the fields of portable devices as the energy storage devices. However, the state-of-the-art positive electrodes, fail to meet our increasing demand for high capacity.[39, 94] For instance, typical layered oxides $LiTMO_2$ are restricted to relatively low energy density.[95] Layered Li-rich oxides have high capacity and property of cathodic and anionic redox mechanism, as introduced in **Chapter 3**, herein, focusing widespread attention aiming to solve the capacity issues.[27, 29, 51, 96] Li_2MnO_3, one representative, delivers a high standard of capacity (more than 400 mAh g^{-1}) in initial cycles, giving our more possibility for designing large-capacity cathodes.[97] Although Li-rich cathodes own large specific capacity, they suffer from serious capacity and voltage decay, restricting the further development of these materials.[98-99] Therefore, $xLi_2MnO_3 \cdot (1-x)LiNi_{0.5}Mn_{0.5}O_2$, as the series of derivate Li-rich material cathodes, are the promising substitutes with equivalent capacity and improved stability, drawing extensive attention of the researchers.[100-106] However, the derivate cathodes also suffer from the common failure of phase transition during cycling, as displayed in common layered oxides, degrading the electrochemical performance.[107] The proposed phase transition mechanisms in typical layered Li-rich materials are shown in **Figure 4.1**. We have identified that oxygen participates in the charge compensation with the reversible reaction of O^{2-}/O^{-} in **Chapter 3**. In this Chapter, we concern the stability of capacity and voltage of Li-rich materials.

Recently, the cation-disordered rock-salt materials are found to be the promising cathodes with stable NaCl type structure, a space group of Fm-3m, stable network and high capacity. In general, $LiTMO_2$ always show electrochemically inactive with rock-salt structure because of the low diffusion dynamics for 0-TM diffusion in stoichiometry $LiTMO_2$.[108] A percolation mechanism reported by Ceder *et al.* makes a

major breakthrough in active diffusion channels for cation-disordered materials. The authors pointed out that it is essential to generate diffusion pathways (0-TM channel in "*o-t-o*" mechanism) by adding excess Li (≥ 9%).[108] Inspiringly, a series of Li-rich cathodes with high capacity have mushroomed based on cation-disordered rock-salt structure. Yabuuchi *et al.* reported the Li_3NbO_4-based system electrodes. Chen *et al.* put the material further to investigate detailed redox chemistry in $Li_{1.3}Nb_{0.3}Mn_{0.4}O_2$.[109-111] Ceder *et al.* reported $Mn^{2+/4+}$ redox oxyfluoride based V system, Nb system ($Li_2Mn_{2/3}Nb_{1/2}O_2F$) and Ti system ($Li_2Mn_{1/2}Ti_{1/2}O_2F$).[112-113] The cathodes exhibit evident advantages of chemical and structural stability, and high capacity. However, the voltage stability, cycling stability and high rate performance are also inferior, although the cathodes possess firm structure and stable voltage output.[114] Meanwhile, the Li-rich cation-disordered rock-salt oxides usually exhibit the sluggish kinetics. Herein, a new rock-salt type cathode $Li_2Ni_{1/3}Ru_{2/3}O_3$ (hereafter denoted as LNRO) is propounded aiming to promote the cycling stability and voltage stability.

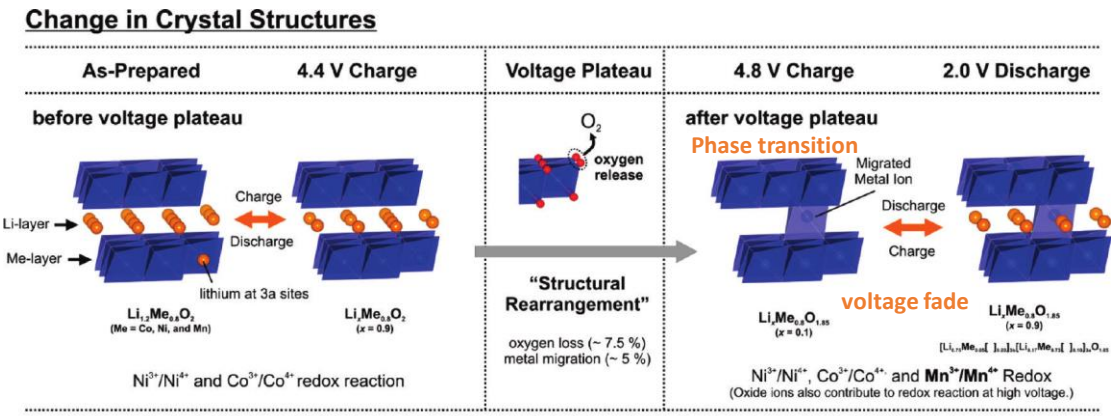

Figure 4. 1 Schemes of the proposed phase transition mechanisms in typical layered Li-rich material.[69] Copyright © 2011, American Chemical Society.

Results demonstrate that $Li_2Ni_{1/3}Ru_{2/3}O_3$ cathode delivers a large capacity, outstanding rate capability as well as good cycling performance with negligible voltage decay, which is superior compared with common cations disordered oxides with space group Fm-3m. Oxygen activation is also confirmed by first principle calculations. Moreover, the cathode owns good kinetics with more 0-TM percolation networks.

Oxygen activation still investigated by in situ Raman, as reversible O^{2-}/O^{-} evolution during cycles in this type cathode for the first time. These findings broaden the sight for developing a stable Li-rich oxide with high cycling performance including reversible oxygen activation and without voltage decay by controlling the special structure. The results also enrich the Li-rich material family and provide more possibility for the next generation of cathodes.

4.2 Crystal structure and DFT calculations of $Li_2Ni_{1/3}Ru_{2/3}O_3$

4.2.1 Morphology and structure of $Li_2Ni_{1/3}Ru_{2/3}O_3$

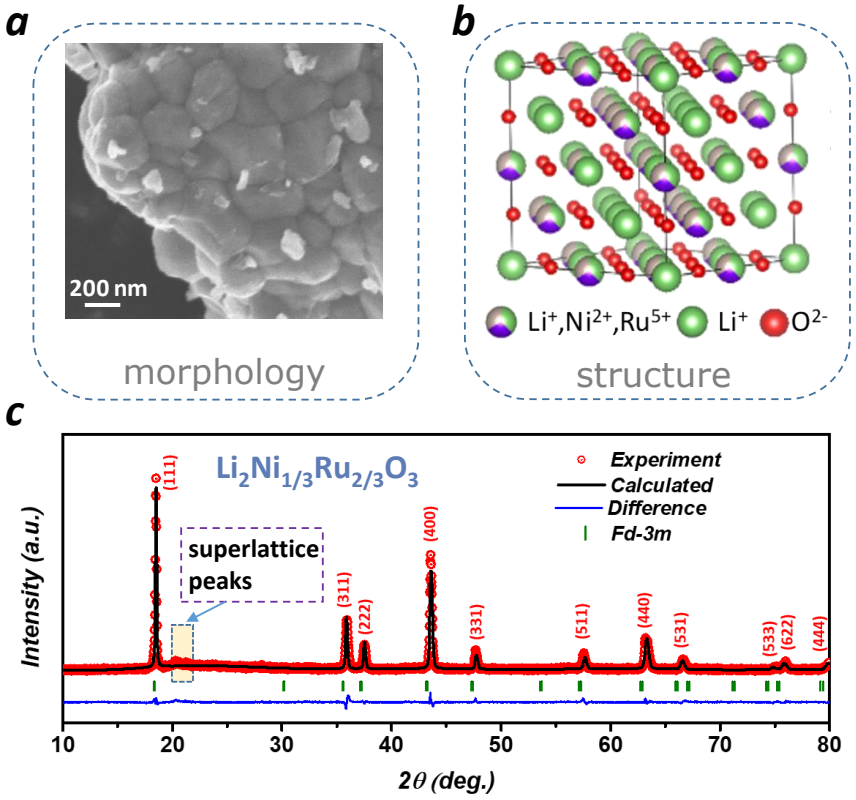

Figure 4. 2 Morphology and structure of the cathode $Li_2Ni_{1/3}Ru_{2/3}O_3$. a) SEM images. b) The diagram of the crystal $Li_2Ni_{1/3}Ru_{2/3}O_3$. c) XRD patterns of $Li_2Ni_{1/3}Ru_{2/3}O_3$ and the corresponding Rietveld refinement.

The material LNRO was then characterized by SEM (TOPCON DS-720 instrument) and powder XRD, as shown in **Figure 4.2a** and **4.2c**. The aggregates are secondary particles composed by the primary nanoparticles with a diameter of ~ 200 nm. The rapid

kinetics of LNRO is beneficial to the nanometer sized grains, which with the reduced diffusion distance of ions and electrons. The schematic diagram in **Figure 4.2b** exhibits the crystal structure, making a better understanding of this material. Note that the structure of LNRO is different from that of the cation-disordered rock-salt NaCl type oxides, in which all cations occupy the same 4b site, such as Li-Mn-V-O-F system and $Li_{1.25}Nb_{0.25}V_{0.5}O_2$ reported by Ceder *et al.* and Yabuuchi *et al.*, respectively.[110, 112] In $Li_2Ni_{1/3}Ru_{2/3}O_3$, which can be also written as $Li(Li_{1/3}Ni_{2/9}Ru_{4/9})O_2$, there is one Li occupies 16c site, Ni, Ru and residual Li occupy 16d site, isostructural with the ordered Fd-3m rock-salt $LiFeO_2$.[115] All the cations and anions occupy the center of the octahedron, coordinating eight neighbor atoms.

Table 4. 1 Refinement results of LNRO in Figure 4.2c.

Li_2MO_3 (Fd-3m) Rwp=0.10 Rp=0.07 a=b=c= 8.3767Å, α=β=γ= 90°							
Atom	site	x	y	z	$Occ._{theo}$	$Occ._{refined}$	Uiso
Li1	16c	0	0	0	1	0.885	0.290
Ni1	16c	0	0	0	0	0.115	0.037
Li2	16d	0.5	0.5	0.5	0.333	0.448	0.019
Ni2	16d	0.5	0.5	0.5	0.222	0.105	0.160
Ru	16d	0.5	0.5	0.5	0.445	0.445	0.029
O	32e	0.2558	0.2558	0.2558	1	1	0.063

Moreover, LNRO was characterized by XRD, as shown in **Figure 4.2c**. Results indicate that most diffraction peaks coincide well with a cubic structure with the space group of Fd-3m except some small peaks at ~ 21°. The additional peaks are characteristic of Li-rich materials, similar to the typical layered Li-rich cathode. GSAS + EXPGUI suite were utilized to obtain the Rietveld refinements results.[55-56] The calculated peaks are well overlapping with that of the experimental, with the lattice parameters $a = b = c = 8.38$ Å, $\alpha = \beta = \gamma = 90°$ and a rational low χ^2 (3.41) value based on Fd-3m space group (see detailed results in **Table 4.1**). $LiMn_2O_4$ also belongs to Fd-3m space group, which should be noted, presenting a similar XRD pattern with that of

LNRO. The differences are that Li in $LiMn_2O_4$ occupies 8a site which is the center of the tetrahedron, while Li occupies the center of octahedron in the rock-salt Fd-3m type LNRO.[116-117]

4.2.2 Computational methodologies

First principle density functional theory calculations are employed to better understand the advantages of this special Fd-3m structure and electrochemical characteristics of LNRO. A 6 × 6 × 2 supercell of the Fd-3m primitive cell has been constructed to capture both the position and potential cation disorder within LNRO compound.

The atomic structure of LNRO has been constructed from the Fd3-m space group. To be consistent with experimental observations, the 16c sites are set to be occupied by Li^+ or Ni^{2+} while 16d sites are set to be occupied by Li^+, Ni^{2+} or Ru^{5+}. A 6 × 6 × 2 supercell of the Fd-3m primitive cell has been constructed to capture both the position and potential cation disorder within $Li_2Ni_{1/3}Ru_{2/3}O_3$ compound. To estimate the equilibrium cation ordering of $Li^+/Ni^{2+}/Ru^{5+}$, all the possible orderings within the supercell have been enumerated and ranked by electrostatic interactions while 20 structures with the lowest electrostatic energy are selected. This framework has been adopted previously in a variety of disorder rock-salt materials with reasonable accuracy [27], so it should be able to offer a reasonable description of cation ordering in Li-Ni-Ru-O system as well.

For the identified low energy structure, first principle DFT calculations are then performed for structural optimization. The Perdew-Burke-Ernzerhof (PBE) functional and projector augmented-wave (PAW)[118] method are adopted using the Vienna ab initio simulation package (VASP). Meanwhile, a Hubbard like U of 6.0 eV [119-120] has been applied for Ni to capture the localization effect of d orbitals. In each calculation, an energy cutoff of 700 eV was adopted while higher cutoff will have and energy difference of less than 0.01 eV. When performing the structure optimizations, the system is regarded as converged when the force per atom is less than 0.01 eV/Å. After

structural optimization, the cation ordering with the lowest energy is used to analyze the potential redox mechanism.

4.2.3 DFT results of $Li_2Ni_{1/3}Ru_{2/3}O_3$

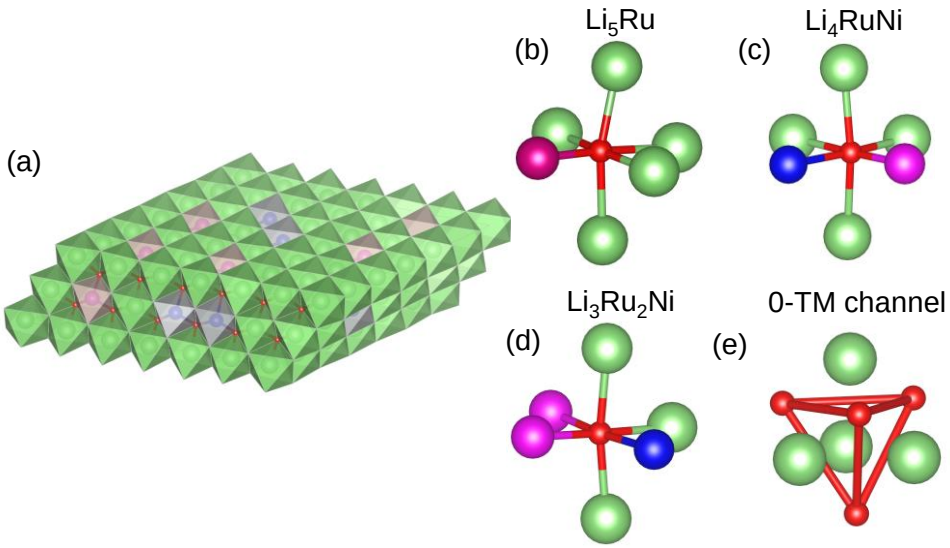

Figure 4. 3 Atomic configurations and local ordering of $Li_2Ni_{1/3}Ru_{2/3}$. a) Demonstration of cation ordering; The identified local ordering of O-M (M = Li,Ru,Ni) bonds: b) Li_5Ru; c) Li_4RuNi; d) Li_3Ru_2Ni. e): Demonstration of 0-TM channel identified.

Representatives of the cation ordering are demonstrated in **Figure 4.3**. It has been pointed out that that the energy of oxygen can be raised due to Li-O-Li configuration and then the oxygen can be easily oxidized, as reported in previous research.[27, 29, 109] Several local ordering configurations are identified and three of them are demonstrated in **Figure 4.3b - 4.3d**, with the analysis of the local ordering in the simulation cells obtained by DFT calculations. It has been found out that the Li-O-Li will not only be formed within Li rich local environment (Li_5Ru in **Figure 4.3b**) from all three types of local ordering, but can also be observed in transition metal rich environments (Li_4RuNi in **Figure 4.3c** and Li_3Ru_2Ni in **Figure 4.3d**). As is proposed in the previous report, the formation of Li-O-Li configuration will contribute to the oxygen activation by generating new Li-O-Li states that are much easier to be oxidized (structure of 0-TM

channel in **Figure 4.3e**). The fact that there are many Li-O-Li configurations in the low energy structure obtained already reveals the tendency of easier oxygen activation.

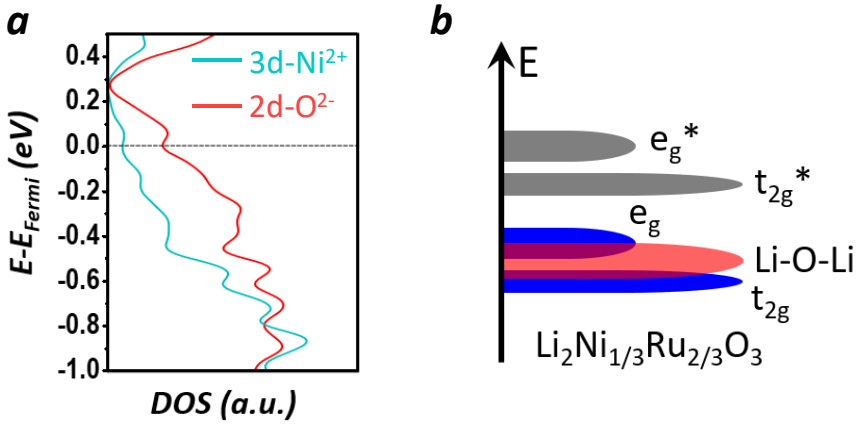

Figure 4. 4 a) Electronic structure of $Li_2Ni_{1/3}Ru_{2/3}O_3$ using orbital projected density of states (PDOS). b) Schematic demonstration of energy distributions from different orbitals.

Moreover, it can also be observed that below Fermi level, there has been a large density of O 2p states, which also overlaps strongly with the 3d-Ni^{2+} states, as shown in the projected density of states (PDOS) in **Figure 4.4a**. A schematic band alignment has been visualized in **Figure 4.4b**, which will give a better idea of the energy level distribution. The phenomenon described above indicates the fact that large amounts of oxygen states will be activated in LNRO, just as the typical layered Li-rich oxides. During charging process, oxygen activation will compete with oxidation process of transition metal. Meanwhile, the observation of 0-TM channel in such composition also reveals the fact that Li percolation will be also facilitated due to the Li-Ni-Ru cation disorder. For the typical disordered rock-salt materials, all the cations are regarded as randomly distributed so all sites are occupied with equal probability by different cations. The nearly full occupied 16c sites in LNRO indicates the short-range ordering of Li in a certain region of the lattice. This special configuration will contribute to form the percolation network with more connected 0-TM channels, resulting in a better kinetic behavior than the typical disorder rock-salt structure.

4.3 Phase transition in $Li_2Ni_{1/3}Ru_{2/3}O_3$ during cycling

4.3.1 Charge-discharge curve of $Li_2Ni_{1/3}Ru_{2/3}O_3$

The electrode was tested at the galvanostatic model with a current density of 10 mA g^{-1}. The typical first charge-discharge cycle was exhibited in **Figure 4.5**. Note that the valence of Ru here is +5 and it cannot be oxidized further.[32] According to **equation 1.8**, the theoretical capacity of $Li_2Ni_{1/3}Ru_{2/3}O_3$ can be calculated as ~ 120 mAh g^{-1} based on the cationic redox process of Ni^{2+}/Ni^{4+}, corresponding to 0.67 extracted-Li^+ from the crystal, which has marked by the green area. The theoretical capacity is apparently lower than the total charge capacity, which is ~ 312 mAh g^{-1}, corresponding to ~ 1.8 extracted-Li^+ from the crystal. The oxide demonstrates a considerable capacity and the capacity is reasonable caused by the oxygen activation, which is similar to the typical layered Li-rich oxides and will be discussed detailed later. The first discharge capacity is 260 mAh g^{-1}, indicating a better coulombic efficiency than layered Li-rich oxides.

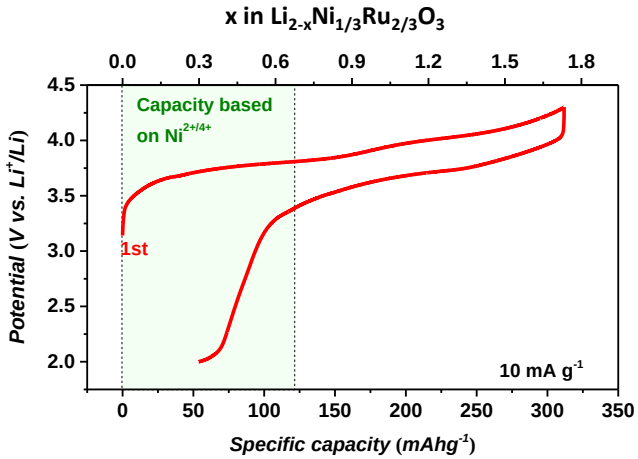

Figure 4. 5 Typical charge-discharge profile of $Li_2Ni_{1/3}Ru_{2/3}O_3$ between 2.0 and 4.3 V with the current density of 10 mA g^{-1}.

4.3.2 Structural evolution of $Li_2Ni_{1/3}Ru_{2/3}O_3$ during cycling

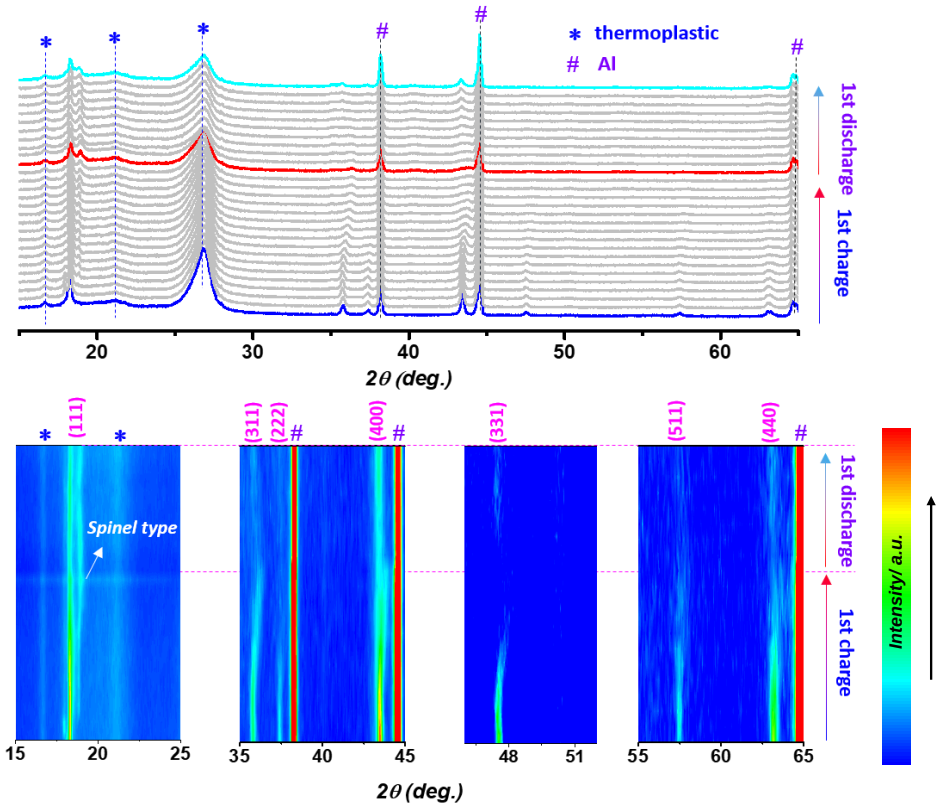

Figure 4. 6 In-situ XRD patterns of $Li_2Ni_{1/3}Ru_{2/3}O_3$ during the first charge discharge process, accompanied by the color-coded images.

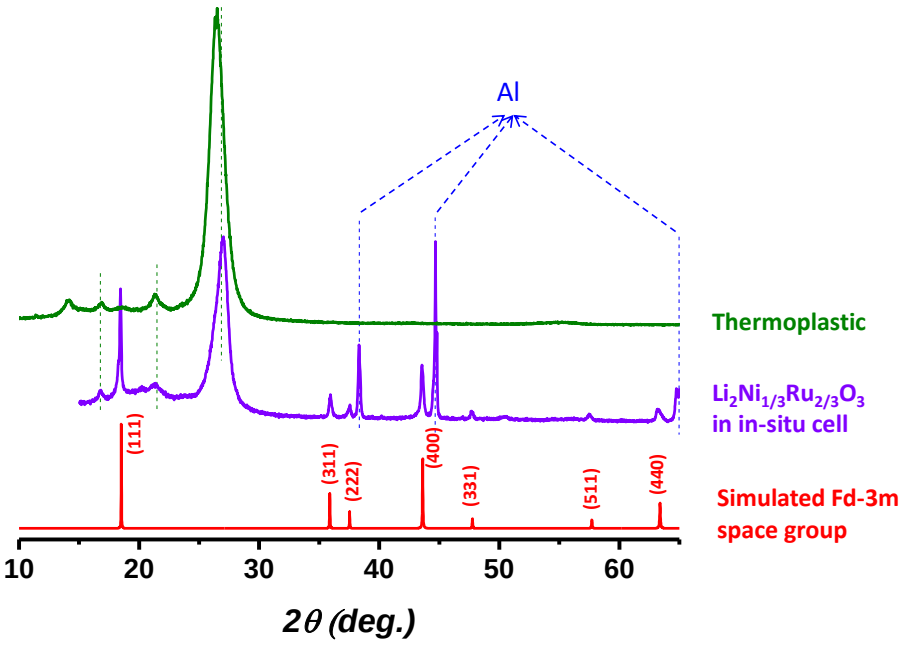

Figure 4. 7 The comparison of XRD patterns between thermoplastic and $Li_2Ni_{1/3}Ru_{2/3}O_3$ in in-situ cell.

As shown in Chapter 3, in-situ XRD is a powerful tool to investigate the structural evolution of electrode during cycling. Here, in-situ XRD was employed for LNRO, with the clearer color-coded images as displayed in **Figure 4.6**. A coin cell has been specially adapted for in-situ test, with a window sealed with a Kapton film by annealing with a thermoplastic. The symbols # and ∗ in **Figure 4.6** represent the peaks of aluminum and thermoplastic, respectively. In contrast, the separate XRD pattern of thermoplastic is also shown in **Figure 4.7**.

All the peaks shift slightly from their original positions and exist the whole process in **Figure 4.6**, demonstrating good structural stability. Most peaks shift to a higher 2θ angle during the charge process and return to the original angle during the discharge process. The electrode holds a stable rock-salt structure with the space group of Fd-3m, guaranteeing a stable migration of Li-ions and electrochemical performance. Noting that there appears one small peak near (111) peak. As is well known, the spinel Fd-3m material exhibits a similar XRD pattern with this rock-salt LNRO.

4.3.3 XPS analysis of $Li_2Ni_{1/3}Ru_{2/3}O_3$ during cycling

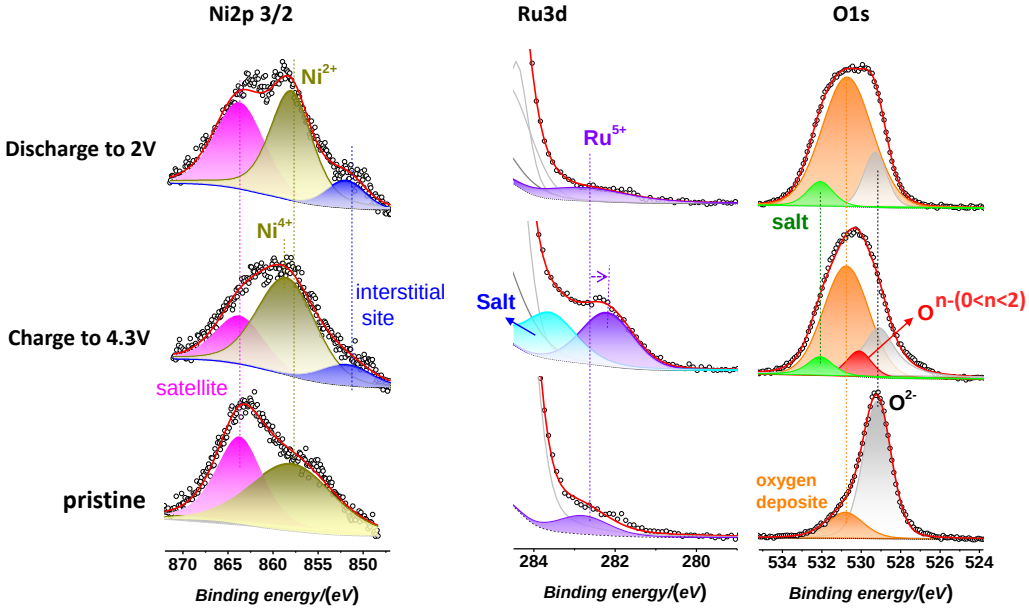

Figure 4. 8 The XPS results of Ni2p, Ru3d and O1s for the samples of pristine, charge to 4.3 V and discharge to 2 V, respectively.

XPS results show more findings and details, as displayed in **Figure 4.8**. Ni spectrum shows a pair of peaks for the pristine LNRO, which can be assigned to Ni^{2+} and satellite peak.[121-122] The peaks located at 529.3 eV and 282.5 eV belongs to lattice O^{2-} and Ru^{5+}, respectively.[123] Ni^{2+} peak shifted to a higher binding energy at ~ 4.3 V charging potential, which is assigned to Ni^{4+}. Due to the occupation of Li or Ni at tetrahedron site (due to "*o-t-o*" diffusion mechanism), there appears a new small peak at 851 eV.[122] Moreover, the interstitial site also exists in Ni spectrum accompanied by Ni^{4+} reduced to Ni^{2+} after the electrode discharging to 2 V. The results of Ni 2p indicate that there are atoms occupy the tetrahedron center (8a site) during cycling, accounting for the appearance of a new peak near (111), which can be assigned to $(111)_{spinel}$. This peak then, can be obtained the whole process, consistent well with the XRD patterns and irreversible interstitial atoms revealed by XPS data. Ru peak exhibits an unusual shift to a lower binding energy, which is well consistent with the phenomenon observed by Tarascon *et al.* in Ru-based Li-rich materials, attributing to the strong electronic redistributions along with the Ru-O bonds during charging.[51, 77] In O 1s spectrum, there is a special peak located at 530.3 eV, which is a symbol of oxygen activation, consistent well with DFT calculations and the high capacity in the initial cycles. More importantly, Ru^{5+} peak returns to its original position without any reduced process during discharging process. And the oxidized O was simultaneously reduced to O^{2-}, indicating a reversible process between charge and discharge. XPS results confirm the companied peak near (111) in XRD and the charge compensation mechanism. From these data, however, we only know that oxygen participates the redox process, while the detailed form is still unknown.

4.4 Oxygen behavior in $Li_2Ni_{1/3}Ru_{2/3}O_3$

It is well known that the oxygen activation is responsible for the higher capacity in Li-rich system.[29, 65] We showed the reversible O^{2-}/O^{-} redox process in typical Li-rich layered cathode $Li_{1.2}Ni_{0.2}Mn_{0.6}O_2$ in **Chapter 3**.[106] However, the detailed pathway of oxygen in Li-rich rock-salt oxides remains unknown. Herein, to confirm the oxygen

behavior in LNRO, in-situ Raman has been employed because it is sensitive to oxygen behaviors. [62, 124]

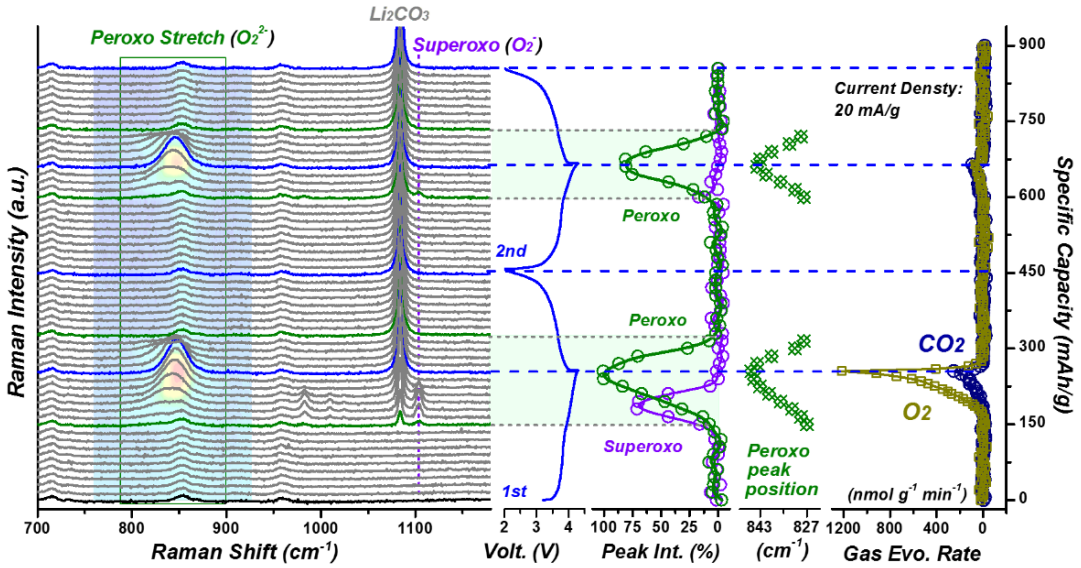

Figure 4. 9 The results of in situ Raman spectra for the initial two galvanostatic cycles (20 mA g^{-1}) corresponding to the capacity-potential curves and the in-situ GC-MS results of gas evolution rates for CO_2 and O_2. The novel peroxo-species and superoxo-species peaks have been highlighted, and corresponding peak intensity (green and purple hollow circles) and peroxo peak position are amplified, respectively.

Raman results are exhibited in **Figure 4.9** accompanied with electrochemical charge/discharge curves for the first two cycles at the current density of 20 mA g^{-1}. Some peaks change remarkably during cycling. In addition to other peaks we can't concern, the regions from 800 cm^{-1} to 900 cm^{-1} was our focus, which represent peroxo stretch as discussed in **Chapter 3**. The peak around 1100 cm^{-1} is assigned to superoxo stretch. For peroxo stretch, a peak located at 827 cm^{-1} is clear when charging to ~ 4.0 V potential, which is known as O_2^{2-} (peroxo O^-–O^- bond). The peak turns to a higher wavenumber till the end of charge process, indicating gradual shortening of the peroxo O^-–O^- bond length. Then, the peak turns back to its original position. The length range of the peroxo O^-–O^- bond, just as indicated in **Chapter 3**, can be empirically regarded as 1.28 Å ~ 1.48 Å. [74-75] Around 860 cm^{-1} there is one small peak in the whole charge/discharge process, which can be assigned as electrolyte. Note that the peak of

O_2^{2-} reemerges at a same potential during the second charging process, and then fades away during the discharging process, which is similar to the first cycle, indicating a good reversibility of oxygen activation process. The results are consistent well with the large capacity in **Figure 4.5** and the XPS analysis. For superoxo stretch (O_2^-) located at 1104 cm^{-1}, the peak appears synchronously with the peroxo O-O bond during the first cycle. However, this peak disappears in the subsequent cycles, indicating that the superoxo stretch may be ascribed from some unstable oxygen atoms. The comparison of peroxo stretch and superoxo stretch is also enlarged in **Figure 4.9**. Furthermore, the gases of O_2 and CO_2 produced during cycling are recorded by an accurate in-situ GC-MS measurement, as displayed in **Figure 4.9**. The evolution of O_2 gas is same as that of superoxo (O_2^-) in Raman spectra, which reaches its maximum at the end of charge. There also exists evolution of CO_2 gas, similar to O_2 and superoxo (O_2^-), indicating that CO_2 gas is produced by the decomposition of the electrolyte which may be attacked by O_2^-. There is almost no evolution of CO_2 and O_2 during the subsequent cycles, which is consistent with the trend of O_2^-, further demonstrating the gases are activated by O_2^-. Note that the signal of peroxo O_2^{2-} is still robust, indicating that O_2^{2-} is the main form of oxygen behavior during cycling. Consequently, in-situ Raman results provide solid evidence of the reversible oxygen activation process in Li-rich rock-salt LNRO, with the form of O_2^{2-}, which is similar to the typical layered Li-rich oxides.

4.5 Electrochemical performance of $Li_2Ni_{1/3}Ru_{2/3}O_3$

4.5.1 Charge-discharge curves of $Li_2Ni_{1/3}Ru_{2/3}O_3$ at different densities

From here, we concern the electrochemical performance exhibited by this Li-rich rock-salt cathode LNRO. **Figure 4.10a** shows the first two cycles of LNRO at low current density. The second profile shows a similar curve shape with the first cycle, indicating consistency of the redox process in LNRO, which is different from the typical layered Li-rich layered materials. There is one plateau at the high potential in the first cycle while the plateau changes to a slope in subsequent cycles in typical layered Li-rich materials. **Figure 4.10b** presents the electrochemical curves at different

current densities. The capacities at 20, 50, 100, 200, 500 mA g^{-1} are 227, 179, 150, 115, and 84 mAh g^{-1}, respectively. **Figure 4.10c** exhibits the corresponding cycling performance. The capacity decreases when the current increases, then recovers to a high level when the current density return to 20 mA g^{-1}, demonstrating LNRO a robust ability of capacity recovery.

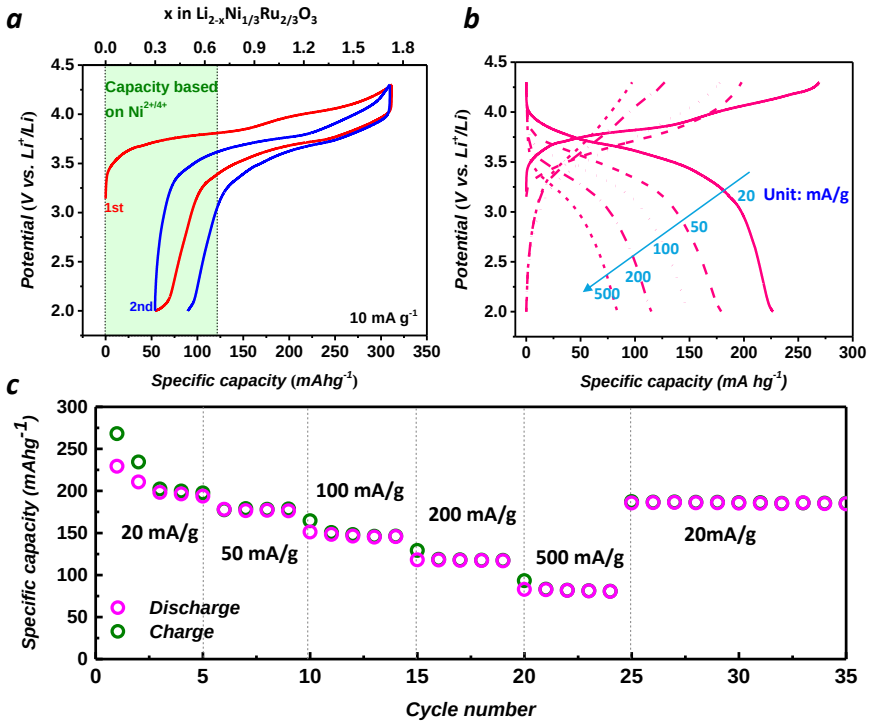

Figure 4. 10 Electrochemical performances of $Li_2Ni_{1/3}Ru_{2/3}O_3$ as the positive electrodes. a) Typical initial two charge-discharge profiles between 2.0 and 4.3 V with the current density of 10 mA g^{-1}. b) Rates performance of the electrode with the current density of 20, 50, 100, 200 and 500 mA g^{-1}, respectively. c) Cycling performance of the electrode at the different current density.

4.5.2 Improvements of $Li_2Ni_{1/3}Ru_{2/3}O_3$ on suppressing capacity fade and voltage fade

As displayed in the introduction part (**Chapter 4.1**), layered Li-rich materials always suffer from phase transition during charging process, leading to severe capacity fade and voltage fade. We have identified that cubic rock-salt type LNRO has robust

structural stability and characteristic of oxygen redox. Naturally, we want to know whether LNRO suffers from similar problems.

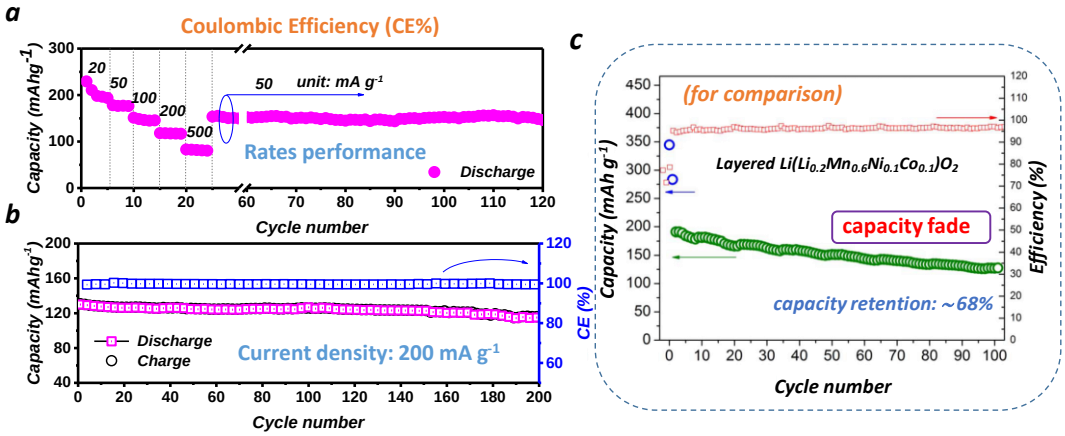

Figure 4. 11 Electrochemical performances of $Li_2Ni_{1/3}Ru_{2/3}O_3$ as the positive electrodes. a) Rates performance of the electrode at different current densities. b) Cycling performance of the electrode at a high current density of 200 mA g^{-1}. c) Cycling performance of typical layered Li-rich cathode for comparison, with serious capacity decay. [35] Copyright 2019 Copyright Clearance Center.

Figure 4.11a exhibits rates performance for every 5 cycles at the current densities of 20, 50, 100, 200 and 500 mA g^{-1}, corresponding to **Figure 4.10c**. Then, the current density recovers to 50 mA g^{-1} until the end of 120 cycles. The capacity holds well at this current density, with an excellent capacity retention of ~ 97 %. Moreover, cycling performance of LNRO are also shown in **Figure 4.11b** at 200 mA g^{-1} (the current density of the first two cycles is 10 mA g^{-1} for activation process). The material maintains excellent capacity retention of ~ 91 % after 200 cycles, with an initial and last capacity of 130.8 and 119.6 mAh g^{-1} at 200 mA g^{-1}, respectively. In contrast, layered Li-rich cathode $Li(Li_{0.2}Mn_{0.6}Ni_{0.1}Co_{0.1})O_2$ shows inferior capacity retention, with a value of ~ 68 % only after 100 cycles, as shown in **Figure 4.11c**. The severe capacity fade exhibits a tremendous difference compared with LNRO, indicating a good capability of suppressing capacity decay in LNRO. And the purpose of improving capacity stability is achieved!

LNRO shows good capacity retention, we also concern about the problem of voltage decay. Then, the normalized charge-discharge profiles are tested at the current density

of 200 mA g^{-1} for the first 200 cycles, as shown in **Figure 4.12a**. The trend of voltage decay is unnoticeable with the overlapping profiles, revealing the outstanding stability of LNRO at high current density. In contrast, layered Li-rich cathode shows a serious voltage decay, as shown in **Figure 4.12b**. And the purpose of improving voltage stability is achieved!

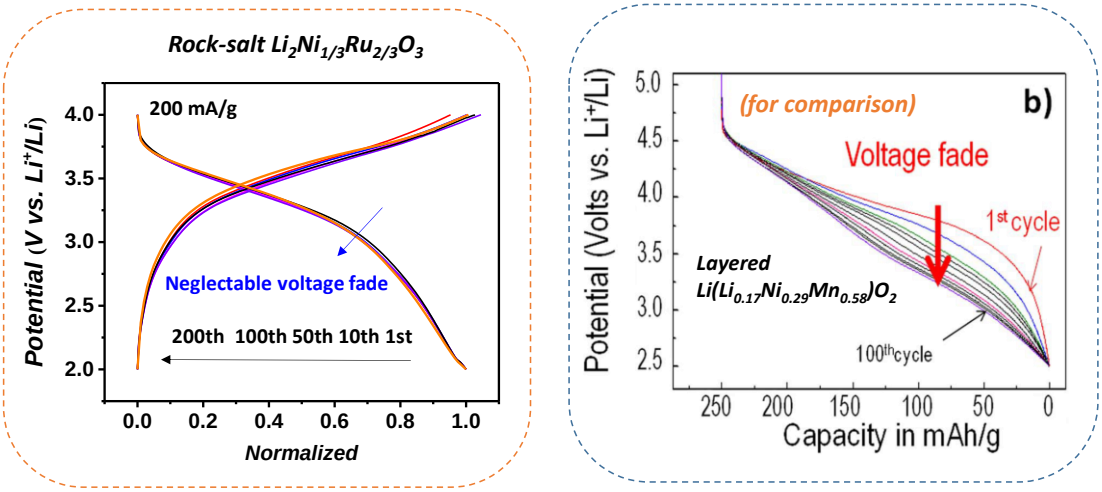

Figure 4. 12 a) The charge/discharge profiles of $Li_2Ni_{1/3}Ru_{2/3}O_3$ with normalized capacity for the first 200 cycles at the current density of 200 mA g^{-1}. b) Normalized capacity of typical layered Li-rich cathode for comparison, with serious voltage decay. [34] Copyright 2019 Copyright Clearance Center.

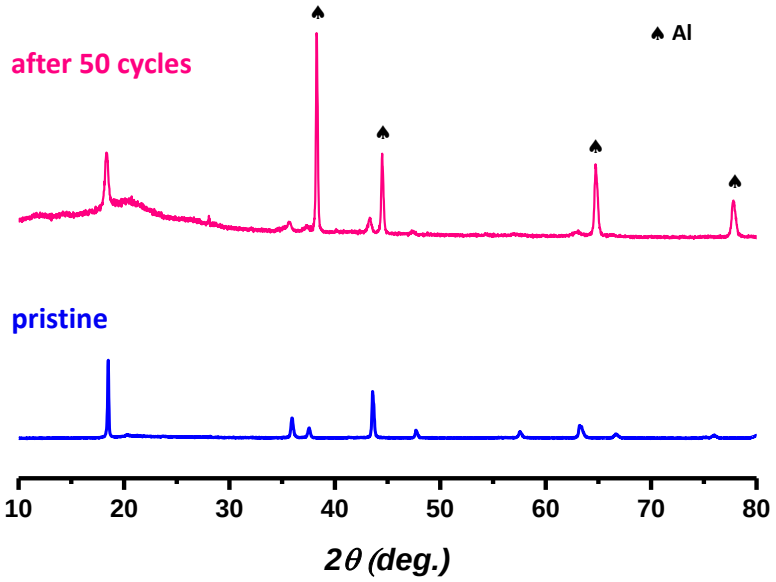

Figure 4. 13 The comparison of XRD patterns for the pristine $Li_2Ni_{1/3}Ru_{2/3}O_3$ and cycled electrode after 50 cycles.

Furthermore, the XRD patterns of the pristine and the electrode after 50 cycles are displayed in **Figure 4.13** for comparison. All peaks of the cycled electrode are indexed to the cubic Fd-3m space group, coinciding well with the pristine oxide, further demonstrating LNRO a structural stability.

4.5.3 GITT test of $Li_2Ni_{1/3}Ru_{2/3}O_3$

Galvanostatic intermittent titration technique (GITT) was utilized to analyze the kinetics of LNRO during cycles and reveal the reason of excellent cycling stability presented by LNRO. The diffusion coefficient (D_{Li}) can be determined by inducing Fick's second law of diffusion based on some reasonable assumptions, as shown in **equation 4.1** after simplifying:

$$D_{Li} = \frac{4}{\pi\tau}\left(\frac{n_m V_m}{S}\right)^2 \left(\frac{\Delta E_s}{\Delta E_t}\right)^2 \quad (4.1)$$

Where V_m is the molar volume of the LNRO, n_m is the mole number of the reactive electrode, S is the area of electrode, τ is the limited time period, ΔE_t and ΔE_s are the total change and the change in the steady state potential during the current flux by subtracting the IR drop, respectively.[125] The parameters were labeled in **Figure 4.15** for both charge and discharge process.

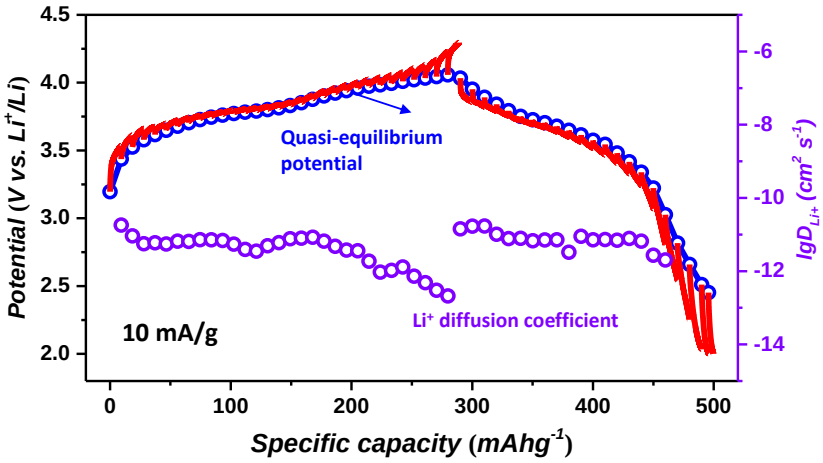

Figure 4. 14 GITT results of $Li_2Ni_{1/3}Ru_{2/3}O_3$ for the first cycle with the variation of quasi-equilibrium potentials and the calculated Li^+ diffusion coefficient.

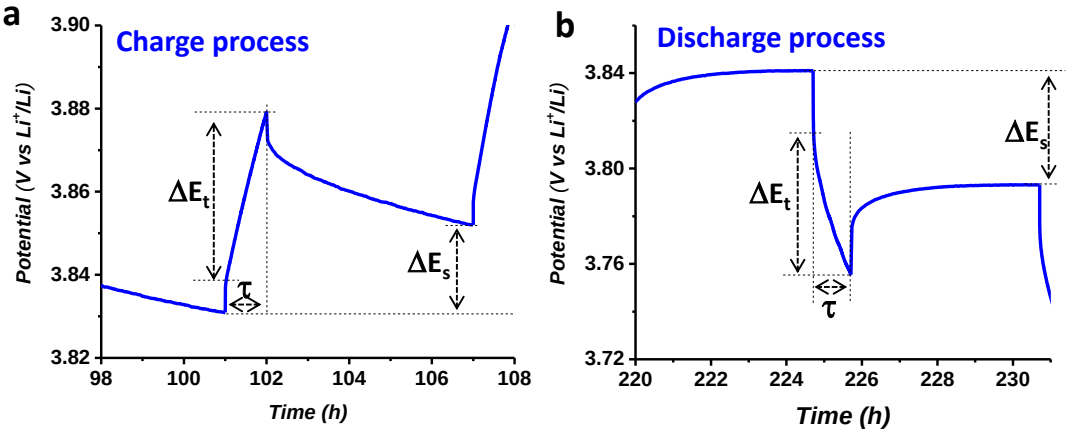

Figure 4. 15 a) The potential profile for a single titration at 3.84 V during charge process with labelling the different parameters. b) The potential profile for a single titration at 3.83 V during discharge process with labelling the different parameters.

The cell was charged/discharged at the potential window of 2-4.3 V with a current density of 10 mA g^{-1}. For the GITT test, the cell was performed with current flux for 1 hour and then rest for 5 h to obtain a quasi-equilibrium potential. The process was repeated until after the first cycle. As shown in **Figure 4.14**, the red line represents the derived potential curve, and the blue line represents the corresponding quasi-equilibrium potential curve. Meanwhile, the calculated D_{Li} is also represented by the purple circle, according to the **equation 4.1**. D_{Li} ranges from 10^{-13} to 10^{-11} cm^2 s^{-1} vary with the potential. The values are much larger than the reported cation-disordered Fm-3m rock-salt oxides and typical layered Li-rich oxides.[121, 126-128] The kinetics of Fd-3m rock-salt LNRO is in close proximity to Fd-3m spinel $LiMn_2O_4$, indicating that LNRO has the capability of high rate electrochemical performance.[129] A dramatic advantage of LNRO is high D_{Li}, which ensures its prospective high rate performance.

4.6 Conclusions

In summary, a rock-salt type oxide $Li_2Ni_{1/3}Ru_{2/3}O_3$ with a space group of Fd-3m is successfully synthesized. Both cathodic and anionic redox processes are observed in this oxide, resulting in a more than 300 mAh g^{-1} at the current density of 10 mA g^{-1}. In-situ Raman spectra confirms the oxygen activation in this rock-salt Li-rich oxide for

the first time, as a form of O^{2-}/O^{-} redox process. Moreover, the oxide exhibits an excellent rate performance with a high capacity retention of ~ 97 % and ~ 91% after 100 cycles at 50 mA g^{-1} and 200 cycles at 200 mA g^{-1}, respectively. Due to a better kinetic process and structural stability, the oxide displays not only a high capacity but also a better rate performance with negligible voltage decay compared with cations-disordered rock-salt Li-rich oxides and layered Li-rich oxides. Furthermore, DFT results demonstrate that LNRO possesses the short-range ordering of Li in a certain region, leading to a better kinetic behavior. The findings extend the sight of Li-excess based oxides and pave a new way to design the stable high cycling performance materials with high capacity and neglectable voltage decay for the next generation of Li-ion batteries.

Chapter 5. General conclusions and perspectives

5.1 General conclusions

In this dissertation, we have systematically introduced Li-rich oxides as the high-power density cathodes for Li-ion battery. Layered Li-rich oxides have two main problems: the one is about the unclear mechanism of oxygen activation, the other is severe capacity fade and voltage fade. For the first problem, we employ in-situ Raman spectroscopy to directly visualize detailed pathways of oxygen activation because it is a powerful tool to detect oxygen behaviors. However, the signal of covalent oxygen bonds is too weak to detect. Thus, surface-enhanced Raman spectroscopy is applied to increase the signal. For the second problem, we design a cubic rock-salt Li-rich oxide with a stable structure to alleviate the capacity fade and voltage fade because structural stability is important to maintain the capacity stability and voltage stability and cubic rock-salt oxides always own stable structure with firm oxygen network. The main conclusions are shown as follows:

In **Chapter 3**, the purpose of the direct observation of oxygen behavior is implemented. Oxygen participates the redox process for charge compensation in layered Li-rich cathodes, as a type of peroxo bonds. And the peroxo bonds reversibly appear during subsequent cycles, although the shape of charge-discharge curve for the first cycle is different from subsequent cycles. (**Chapter 3.4**). The peroxo bonds tend to form along c axis, which is confirmed by DFT calculations. (**Chapter 3.4** and **3.5**) The DFT calculations are well consistent with in-situ Raman and in-situ XRD results. (**Chapter 3.5**)

In **Chapter 4**, the purpose of alleviating the capacity decay and voltage decay is achieved. Cubic rock-salt Li-rich oxide $Li_2Ni_{1/3}Ru_{2/3}O_3$ possesses stable lattice networks with high structural stability. Both cathodic and anionic redox processes participate the charge compensation in $Li_2Ni_{1/3}Ru_{2/3}O_3$, as well as the typical layered Li-rich oxides. (**Chapter 4.3** and **4.4**) The oxygen behavior is confirmed as O^{2-}/O^{-} redox process by employing surface-enhanced Raman spectroscopy. (**Chapter 4.4**) And this

pathway of oxygen behavior is reported in cubic rock-salt Li-rich oxides for the first time. the material maintains an excellent rate performance with a high capacity retention of ~ 97% and ~ 91% after 100 cycles at 50 mA g^{-1} and 200 cycles at 200 mA g^{-1}, respectively. Meanwhile, the voltage decay is negligible in $Li_2Ni_{1/3}Ru_{2/3}O_3$. (**Chapter 4.5**) The special structure helps to open more 0-TM percolation networks, leading to better kinetic behavior. (**Chapter 4.2** and **4.5**)

In general, the proposed mechanism of the detailed pathway of oxygen behavior gives a better understanding of Li-rich oxides. And of course, there exist other types of oxygen behavior, resulting in irreversible oxygen loss such as forming O_2 and/or Li_2CO_3. We need to stabilize the reversible peroxo bonds and inhibit other types of oxygen. Structural design is an effective method to improve the reversibility of oxygen such as cubic rock-salt Li-rich oxide $Li_2Ni_{1/3}Ru_{2/3}O_3$, stemming from its robust structural stability. And in this research, we just provide one access to improve the electrochemical performance of Li-rich oxides. Our proposes are put forth in the hope that they would attract more proposes. And we hope the results will contribute to the development of Li-ion battery technology for towards high power density, long cycling life and low cost for large scale storage systems.

5.2 Perspectives

Oxygen activation in Li-rich oxides greatly increases the capacity. The energy of O 2p state is raised due to the special Li-O-Li configuration, making a possibility for oxygen to participate oxidation process. And the concept can be adopted in sodium-ion batteries because of the similarity between Li and Na. There are two configurations when replacing Li by Na, namely Na-O-Na and Na-O-Li configuration, as shown in **Figure 5.1a** and **5.1b**. Furthermore, $Na_{2/3}[Mg_{0.28}Mn_{0.72}]O_2$ also has a similar feature with Li-rich oxides, exhibiting an excess capacity based on oxygen redox, which indicates excess alkali-metal is not necessary to active oxygen redox, as shown in **Figure 5.1c**. Thus, the oxygen activation possesses a great scope to develop high power

density battery technologies, which would reach far beyond Li-ion battery, Na-ion battery, etc.

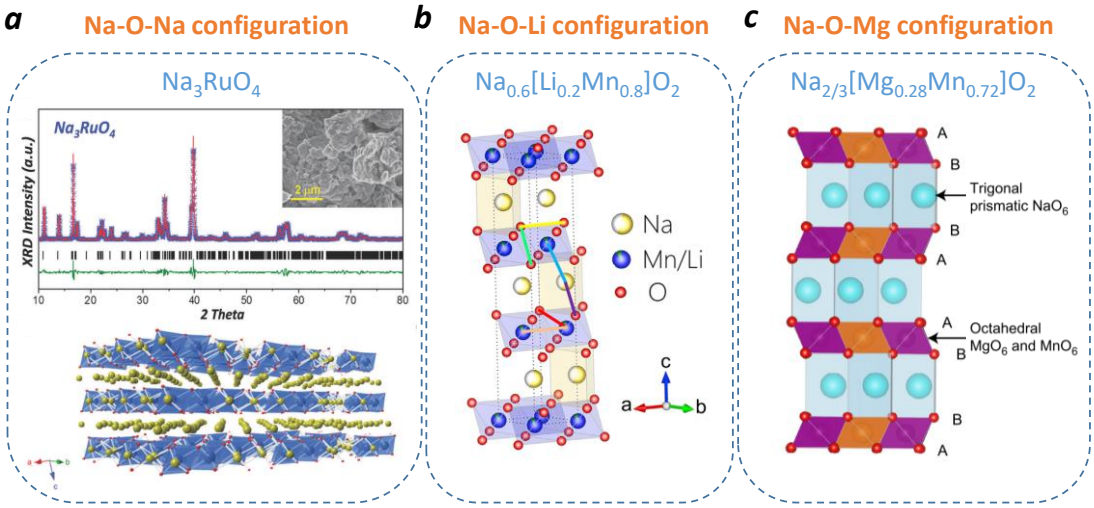

Figure 5. 1 Oxygen activation in sodium-ion batteries due to a) Na-O-Na configuration, [123] b) Na-O-Li configuration, [130] and c) Na-O-Mg configuration. [131] Copyright © 2017 Elsevier Inc. Copyright © 2018, Springer Nature.

List of Publications

First author:

1. **Li Xiang**, Qiao Yu, Guo Shaohua, Xu Zhenming, Zhu Hong, Zhang Xiaoyu, Yuan Yang, He Ping, Ishida Masayoshi and Zhou Haoshen. Direct visualization of the reversible O^{2-}/O^{-} redox process in Li-rich cathode materials. *Advanced Materials*. 2018, 30, 14, 1705197.
2. **Li Xiang**, Qiao Yu, Guo Shaohua, Jiang Kezhu, Ishida Masayoshi and Zhou Haoshen. A new type of Li-rich rock-salt oxide $Li_2Ni_{1/3}Ru_{2/3}O_3$ with reversible anionic redox chemistry. *Advanced Materials*. 2018, 1807825.

(The first two papers are related to this Ph.D. thesis.)

3. **Li Xiang**, Guo Shaohua, Jiang Kezhu, Qiao Yu, Ishida Masayoshi and Zhou Haoshen. Amorphous P_2S_5/C composite as high-performance anode materials for sodium-ion batteries. *ACS applied materials & interfaces*. 2017, 10, 1, 16-20.
4. **Li Xiang**, Guo Shaohua, Deng Han, Jiang Kezhu, Qiao Yu, Ishida Masayoshi and Zhou Haoshen. An ultrafast rechargeable lithium metal battery. *Journal of Materials Chemistry A*. 2018, 6 (32), 15517-15522.
5. **Li Xiang**, Guo Shaohua, Qiu Feilong, Wang Linlin, Ishida Masayoshi and Zhou Haoshen. $Na_2Ru_{1-x}Mn_xO_3$ as the cathodes for sodium-ion batteries. *Journal of Materials Chemistry A*. 2019, 7, 4395-4399.
6. **Li Xiang**, Xu Jialiang, Xi Kaiying, Zhang Haoyang, Jiang Kezhu, Qiao Yu, Zhu Hong, Guo Shaohua, and Zhou Haoshen. Lithium cooperation in sodium-ion battery layered cathode enabling both anionic activity and structural stability, **In preparation.**

Acknowledgements

Time passes quickly. I am lucky enough to study at University of Tsukuba as a doctoral candidate. At the end of my three-year course of PhD, I am enormously grateful for those who have offered help and support on my studying and living.

First of all, I would like to extend my heartfelt gratitude to my supervisor Professor Haoshen Zhou (University of Tsukuba, National Institute of Advanced Industrial Science and Technology (AIST)) for his continued support and patient guidance during my doctoral research. He is a man of wisdom and good sense, always with inspiration which guides me into an in-depth understanding of my research. So I have acquired many skills in these few years. He is very rigorous to our learning attitude and always tells us “one man must be grown to manhood before becoming a useful person”. And he used to discuss some cases in history with us because we can learn a lot from history. I know indeed that I have learnt a lot from him.

Secondly, I would like to express my gratitude to my three vice-supervisors at University of Tsukuba, Prof. Masayoshi Ishida, Associate Prof. Hirohisa Aki and Associate Prof. Nobuko Hanada. When I first came to Japan, they offered help to me selflessly and I could have a quick adaptation to the new environment. Particularly, thanks to the suggestions of Prof. Masayoshi Ishida, Prof. Keiichi Okajima, Associate Prof. Hirohisa Aki and Dr. Hirokazu Kitaura on my graduation presentation, it makes my presentation improved significantly.

Thirdly, I want to express my sincere gratitude to Dr. Shaohua Guo. He guided me step by step into depth analysis and put forward many suggestions on my research work. With his help, encouragement and guidance, I began learning about sodium-ion batteries and oxygen activation and then I could make a progress in my research work. I have learned a lot from him.

Fourth, many thanks to all my group numbers in AIST. Dr. Hirofumi Matsuda who always care about our safety while we are in the lab, Dr. Eunjoo Yoo, Dr. Hirokazu Kitaura and Mr. Jun Okagaki gave a hand to me when I am in difficulty. I also benefit from Dr. Yu Qiao, Dr. Yang Sun, Dr. Jin Yi, Dr. Yarong Wang, Dr. Shichao Wu, Dr.

Songyan Bai, Dr. Qi Li, Dr. Yang Liu, Mr. Han Deng, Mr. Zhi Chang, Ms. Min Jia, Dr. Feilong Qiu, Dr. Linlin Wang, Dr. Yijie Liu, Prof. Jianan Zhang, they gave suggestions and assistance on my life and study. Furthermore, I want to thank my classmate Ms. Yibo He. We came to Japan together. We help each other and I am really happy that we achieved improvements in our research work.

Then, I want to appreciate Mr. Yufeng Bao, Mr. Chenzhu Yin, Ms. Xingyi Zhang and Ms. Jing Cui for their help with my poor Japanese. And I also want to thank Dr. Shichao Wu, Dr. Feilong Qiu, Dr. Linlin Wang, Mr. Xin Cao and Mr. Huijun Yang, we always play badminton together. Sports can reduce fatigue and make me active and energetic. Thus, I can plunge into study full of spirits.

Furthermore, I owe many thanks to the financial support provided by the China Scholarship Council. And I can focus my attention on my research work.

Lastly, I am deeply indebted to my family. My father Huiping Li, my mother Meixiang Li, and my brother Kai Li support me for my entire doctoral program. Especially, thanks to my wife Meng Li, your love and encouragements make me better. Let us work together for a shared future.

REFERENCE

[1] Scharber, M. C.; Mühlbacher, D.; Koppe, M.; Denk, P.; Waldauf, C.; Heeger, A. J.; Brabec, C. J., Design rules for donors in bulk-heterojunction solar cells—Towards 10% energy-conversion efficiency. *Adv. Mater.* **2006,** *18* (6), 789-794.

[2] Koutroulis, E.; Kalaitzakis, K., Design of a maximum power tracking system for wind-energy-conversion applications. *Ieee Trans. Ind. Electron.* **2006,** *53* (2), 486-494.

[3] Nitta, N.; Wu, F.; Lee, J. T.; Yushin, G., Li-ion battery materials: present and future. *Mater. Today* **2015,** *18* (5), 252-264.

[4] http://www.pasticheenergysolutions.com/applications/.

[5] Aqeel, A.; Butt, M. S., The relationship between energy consumption and economic growth in Pakistan. *Asia Pac. Dev. J.* **2001,** *8* (2), 101-110.

[6] Casals, L. C.; García, B. A., A review of the complexities of applying second life electric car batteries on energy businesses, *Energy Syst. Conf.* **2014**.

[7] Du, K.; Xie, H.; Hu, G.; Peng, Z.; Cao, Y.; Yu, F., Enhancing the thermal and upper voltage performance of Ni-rich cathode material by a homogeneous and facile coating method: Spray-drying coating with nano-Al_2O_3. *ACS Appl. Mater. Interfaces* **2016,** *8* (27), 17713-17720.

[8] Ogan, T. L.; Chen, X., The rise of Shenzhen and BYD--How a Chinese corporate pioneer is leading greener and more sustainable urban transportation and development. *Eur. Financ. Rev.* **2016**, 32-39.

[9] Du, W. B.; Zhou, X. L.; Lordan, O.; Wang, Z.; Zhao, C.; Zhu, Y. B., Analysis of the Chinese airline network as multi-layer networks. *Transp. Res. Part E: Logist. Transp. Rev.* **2016,** *89*, 108-116.

[10] Tsujikawa, T.; Yabuta, K.; Arakawa, M.; Hayashi, K., Safety of large-capacity lithium-ion battery and evaluation of battery system for telecommunications. *J. Power Sources* **2013,** *244* (15), 11-16.

[11] Tabisz, W. A.; Jovanovic, M. M.; Lee, F. C., Present and future of distributed power systems. *[Proceedings] APEC'92 Seventh Annual Applied Power Electronics Conference and Exposition, IEEE*. **1992**, 11-18.

[12] Kurzweil, P., Gaston Planté and his invention of the lead–acid battery—The genesis of the first practical rechargeable battery. *J. Power Sources* **2010,** *195* (14), 4424-4434.

[13] Fernandes, A.; Afonso, J. C.; Dutra, A. J. B., Hydrometallurgical route to recover nickel, cobalt and cadmium from spent Ni–Cd batteries. *J. Power Sources* **2012,** *220* (15), 286-291.

[14] Ovshinsky, S.; Fetcenko, M.; Ross, J., A nickel metal hydride battery for electric vehicles. *Science* **1993,** *260* (5105), 176-181.

[15] Etacheri, V.; Marom, R.; Elazari, R.; Salitra, G.; Aurbach, D., Challenges in the development of advanced Li-ion batteries: a review. *Energy Environ. Sci.* **2011,** *4* (9), 3243-3262.

[16] Zhu, G. N.; Chen, L.; Wang, Y. G.; Wang, C. X.; Che, R. C.; Xia, Y. Y., Binary $Li_4Ti_5O_{12}$-$Li_2Ti_3O_7$ nanocomposite as an anode material for Li-ion batteries. *Adv. Funct. Mater.* **2013,** *23* (5), 640-647.

[17] Xu, Y. H.; Zhu, Y. J.; Liu, Y. H.; Wang, C. S., Electrochemical performance of porous carbon/tin composite anodes for sodium-ion and lithium-ion batteries. *Adv. Energy Mater.* **2013,** *3* (1), 128-133.

[18] Mao, J.; Fan, X.; Luo, C.; Wang, C., Building self-healing alloy architecture for stable sodium-ion battery anodes: A case study of tin anode materials. *ACS Appl. Mater. Interfaces* **2016,** *8* (11), 7147-7155.

[19] Wu, L.; Hu, X. H.; Qian, J. F.; Pei, F.; Wu, F. Y.; Mao, R. J.; Ai, X. P.; Yang, H. X.; Cao, Y. L., Sb-C nanofibers with long cycle life as an anode material for high-performance sodium-ion batteries. *Energy Environ. Sci.* **2014,** *7* (1), 323-328.

[20] Abel, P. R.; Lin, Y. M.; de Souza, T.; Chou, C. Y.; Gupta, A.; Goodenough, J. B.; Hwang, G. S.; Heller, A.; Mullins, C. B., Nanocolumnar germanium thin films as a high-rate sodium-ion battery anode material. *J. Phys. Chem. C* **2013,** *117* (37), 18885-18890.

[21] McDowell, M. T.; Lee, S. W.; Nix, W. D.; Cui, Y., 25th anniversary article: understanding the lithiation of silicon and other alloying anodes for lithium-ion batteries. *Adv. Mater.* **2013,** *25* (36), 4966-4985.

[22] Raccichini, R.; Amores, M.; Hinds, G., Critical review of the use of reference electrodes in Li-ion batteries: A diagnostic perspective. *Batteries* **2019,** *5* (12), 1-24.

[23] Kyerematen, N. A.; Hahn, R., Attainable energy density of microbatteries. *ACS Energy Lett.* **2018,** *3* (5), 1172-1175.

[24] Qiu, B.; Zhang, M.; Xia, Y.; Liu, Z.; Meng, Y. S., Understanding and controlling anionic electrochemical activity in high-capacity oxides for next generation Li-ion batteries. *Chem. Mater.* **2017,** *29* (3), 908-915.

[25] Park, S. M.; Cho, T. H.; Yoshio, M., Novel synthesis method for preparing layered Li $[Mn_{1/2}Ni_{1/2}]O_2$ as a cathode material for lithium ion secondary battery. *Chem. Lett.* **2004,** *33* (6), 748-749.

[26] Momma, K.; Izumi, F., VESTA 3 for three-dimensional visualization of crystal, volumetric and morphology data. *J. Appl. Crystallogr.* **2011,** *44* (6), 1272-1276.

[27] Seo, D. H.; Lee, J.; Urban, A.; Malik, R.; Kang, S.; Ceder, G., The structural and chemical origin of the oxygen redox activity in layered and cation-disordered Li-excess cathode materials. *Nat. Chem.* **2016,** *8* (7), 692-697.

[28] Xu, J.; Sun, M.; Qiao, R.; Renfrew, S. E.; Ma, L.; Wu, T.; Hwang, S.; Nordlund, D.; Su, D.; Amine, K., Elucidating anionic oxygen activity in lithium-rich layered oxides. *Nat. Commun.* **2018,** *9* (947), 1-10.

[29] Luo, K.; Roberts, M. R.; Hao, R.; Guerrini, N.; Pickup, D. M.; Liu, Y. S.; Edstrom, K.; Guo, J. H.; Chadwick, A. V.; Duda, L. C.; Bruce, P. G., Charge-compensation in 3d-transition-metal-oxide intercalation cathodes through the generation of localized electron holes on oxygen. *Nat. Chem.* **2016,** *8* (7), 684-691.

[30] Armstrong, A. R.; Holzapfel, M.; Novak, P.; Johnson, C. S.; Kang, S. H.; Thackeray, M. M.; Bruce, P. G., Demonstrating oxygen loss and associated structural reorganization in the lithium battery cathode $Li[Ni_{0.2}Li_{0.2}Mn_{0.6}]O_2$. *J. Am. Chem. Soc.* **2006,** *128* (26), 8694-8698.

[31] Sathiya, M.; Abakumov, A. M.; Foix, D.; Rousse, G.; Ramesha, K.; Saubanere, M.; Doublet, M. L.; Vezin, H.; Laisa, C. P.; Prakash, A. S.; Gonbeau, D.; VanTendeloo, G.; Tarascon, J. M., Origin of voltage decay in high-capacity layered oxide electrodes. *Nat. Mater.* **2015,** *14* (2), 230-238.

[32] Sathiya, M.; Ramesha, K.; Rousse, G.; Foix, D.; Gonbeau, D.; Prakash, A. S.; Doublet, M. L.; Hemalatha, K.; Tarascon, J. M., High performance $Li_2Ru_{1-y}Mn_yO_3$ ($0.2 \leq y \leq 0.8$) cathode materials for rechargeable lithium-ion batteries: Their understanding. *Chem. Mater.* **2013,** *25* (7), 1121-1131.

[33] Yang, W.; Devereaux, T. P., Anionic and cationic redox and interfaces in batteries: Advances from soft X-ray absorption spectroscopy to resonant inelastic scattering. *J. Power Sources* **2018,** *389* (15), 188-197.

[34] Rozier, P.; Tarascon, J. M., Li-rich layered oxide cathodes for next-generation Li-ion batteries: chances and challenges. *J. Electrochem. Soc.* **2015,** *162* (14), A2490-A2499.

[35] Redel, K.; Kulka, A.; Plewa, A.; Molenda, J., High-performance Li-rich layered transition metal oxide cathode materials for Li-ion batteries. *J. Electrochem. Soc.* **2019,** *166* (3), A5333-A5342.

[36] Goodenough, J. B.; Kim, Y., Challenges for rechargeable Li batteries. *Chem. Mater.* **2010,** *22* (3), 587-603.

[37] Whittingham, M. S., Lithium batteries and cathode materials. *Chem. Rev.* **2004,** *104* (10), 4271-4301.

[38] Arico, A. S.; Bruce, P.; Scrosati, B.; Tarascon, J. M.; Van Schalkwijk, W., Nanostructured materials for advanced energy conversion and storage devices. *Nat. Mater.* **2005,** *4* (5), 366-377.

[39] Tarascon, J. M.; Armand, M., Issues and challenges facing rechargeable lithium batteries. *Nature* **2001,** *414* (6861), 359-367.

[40] He, P.; Yu, H. J.; Li, D.; Zhou, H. S., Layered lithium transition metal oxide cathodes towards high energy lithium-ion batteries. *J. Mater. Chem.* **2012,** *22* (9), 3680-3695.

[41] Huang, Z. D.; Liu, X. M.; Zhang, B. A.; Oh, S. W.; Ma, P. C.; Kim, J. K., $LiNi_{1/3}Co_{1/3}Mn_{1/3}O_2$ with a novel one-dimensional porous structure: A high-power cathode material for rechargeable Li-ion batteries. *Scripta Mater.* **2011,** *64* (2), 122-125.

[42] Jiang, Y.; Zhuang, H.; Ma, Q. L.; Jiao, Z.; Zhang, H. J.; Liu, R. Z.; Chu, Y. L.; Zhao, B., Synthesis of porous Li_2MnO_3-$LiNi_{1/3}Co_{1/3}Mn_{1/3}O_2$ nanoplates via colloidal crystal template. *J. Mater. Res.* **2013,** *28* (11), 1505-1511.

[43] Yang, S. Y.; Wang, X. Y.; Yang, X. K.; Liu, L.; Liu, Z. L.; Bai, Y. S.; Wang, Y. P., Influence of Li source on tap density and high rate cycling performance of spherical $Li[Ni_{1/3}Co_{1/3}Mn_{1/3}]O_2$ for advanced lithium-ion batteries. *J. Solid State Electrochem.* **2012,** *16* (3), 1229-1237.

[44] Xi, L. J.; Cao, C. W.; Ma, R. G.; Wang, Y.; Yang, S. L.; Deng, J. Q.; Gao, M.; Lian, F.; Lu, Z. G.; Chung, C. Y., Layered Li_2MnO_3 center dot $3LiNi_{(0.5-x)}Mn_{(0.5-x)}Co_{(2x)}O_2$ microspheres with Mn-rich cores as high performance cathode materials for lithium ion batteries. *Phys. Chem. Chem. Phys.* **2013,** *15* (39), 16579-16585.

[45] Ye, D. L.; Zeng, G.; Nogita, K.; Ozawa, K.; Hankel, M.; Searles, D. J.; Wang, L. Z., Understanding the origin of Li_2MnO_3 activation in Li-rich cathode materials for lithium-ion batteries. *Adv. Funct. Mater.* **2015,** *25* (48), 7488-7496.

[46] Wang, Y. D.; Jiang, J. W.; Dahn, J. R., The reactivity of delithiated $Li(Ni_{1/3}Co_{1/3}Mn_{1/3})O_2$, $Li(Ni_{0.8}Co_{0.15}Al_{0.05})O_2$ or $LiCoO_2$ with non-aqueous electrolyte. *Electrochem. Commun.* **2007,** *9* (10), 2534-2540.

[47] Yu, H. J.; So, Y. G.; Kuwabara, A.; Tochigi, E.; Shibata, N.; Kudo, T.; Zhou, H. S.; Ikuhara, Y., Crystalline grain interior configuration affects lithium migration kinetics in Li-rich layered oxide. *Nano Lett.* **2016,** *16* (5), 2907-2915.

[48] Thackeray, M. M.; Johnson, C. S.; Vaughey, J. T.; Li, N.; Hackney, S. A., Advances in manganese-oxide 'composite' electrodes for lithium-ion batteries. *J. Mater. Chem.* **2005,** *15* (23), 2257-2267.

[49] Lu, Z. H.; MacNeil, D. D.; Dahn, J. R., Layered cathode materials $Li[Ni_xLi_{(1/3-2x/3)}Mn_{(2/3-x/3)}]O_2$ for lithium-ion batteries. *Electrochem. Solid State Lett.* **2001,** *4* (11), A191-A194.

[50] Johnson, C. S.; Kim, J. S.; Lefief, C.; Li, N.; Vaughey, J. T.; Thackeray, M. M., The significance of the Li_2MnO_3 component in 'composite' xLi_2MnO_3 center dot $(1-x)LiMn_{0.5}Ni_{0.5}O_2$ electrodes. *Electrochem. Commun.* **2004,** *6* (10), 1085-1091.

[51] Sathiya, M.; Rousse, G.; Ramesha, K.; Laisa, C. P.; Vezin, H.; Sougrati, M. T.; Doublet, M. L.; Foix, D.; Gonbeau, D.; Walker, W.; Prakash, A. S.; Ben Hassine, M.; Dupont, L.; Tarascon, J. M., Reversible anionic redox chemistry in high-capacity layered-oxide electrodes. *Nat. Mater.* **2013,** *12* (9), 827-835.

[52] McCalla, E.; Abakumov, A. M.; Saubanere, M.; Foix, D.; Berg, E. J.; Rousse, G.; Doublet, M. L.; Gonbeau, D.; Novak, P.; Van Tendeloo, G.; Dominko, R.; Tarascon, J. M., Visualization of O-O peroxo-like dimers in high-capacity layered oxides for Li-ion batteries. *Science* **2015,** *350* (6267), 1516-1521.

[53] Ye, J.; Li, Y. X.; Zhang, L.; Zhang, X. P.; Han, M.; He, P.; Zhou, H. S., Fabrication and performance of high energy Li-ion battery based on the spherical $Li[Li_{0.2}Ni_{0.16}Co_{0.1}Mn_{0.54}]O_2$ cathode and Si anode. *ACS Appl. Mater. Interfaces* **2016,** *8* (1), 208-214.

[54] Jarvis, K. A.; Deng, Z. Q.; Allard, L. F.; Manthiram, A.; Ferreira, P. J., Atomic structure of a lithium-rich layered oxide material for lithium-ion batteries: Evidence of a solid solution. *Chem. Mater.* **2011,** *23* (16), 3614-3621.

[55] Larson, A. C.; Von Dreele, R. B., General structure analysis system (GSAS). *Los Alamos National Laboratory Report LAUR* **1994**, 86-748.

[56] Toby, B. H., EXPGUI, a graphical user interface for GSAS. *J. Appl. Crystallogr.* **2001,** *34*, 210-213.

[57] Kim, J. S.; Johnson, C. S.; Vaughey, J. T.; Thackeray, M. M.; Hackney, S. A., Electrochemical and structural properties of $xLi_2M'O_3$ center dot$(1-x)LiMn_{0.5}Ni_{0.5}O_2$ eIectrodes for lithium batteries (M' = Ti, Mn, Zr; $0 \leq x \leq 0.3$). *Chem. Mater.* **2004,** *16* (10), 1996-2006.

[58] Lu, Z. H.; Dahn, J. R., Structure and electrochemistry of layered $Li[Cr_xLi_{(1/3-x3)}Mn_{(2/3-2x/3)}]O_2$. *J. Electrochem. Soc.* **2002,** *149* (11), A1454-A1459.

[59] Lu, Z. H.; Beaulieu, L. Y.; Donaberger, R. A.; Thomas, C. L.; Dahn, J. R., Synthesis, structure, and electrochemical behavior of $Li[Ni_xLi_{1/3-2x/3}Mn_{2/3-x/3}]O_2$. *J. Electrochem. Soc.* **2002,** *149* (6), A778-A791.

[60] Mohanty, D.; Kalnaus, S.; Meisner, R. A.; Rhodes, K. J.; Li, J. L.; Payzant, E. A.; Wood, D. L.; Daniel, C., Structural transformation of a lithium-rich $Li_{1.2}Co_{0.1}Mn_{0.55}Ni_{0.15}O_2$ cathode during high voltage cycling resolved by in situ X-ray diffraction. *J. Power Sources* **2013,** *229* (1), 239-248.

[61] Tarascon, J. M.; Vaughan, G.; Chabre, Y.; Seguin, L.; Anne, M.; Strobel, P.; Amatucci, G., In situ structural and electrochemical study of $Ni_{1-x}Co_xO_2$ metastable oxides prepared by soft chemistry. *J. Solid State Chem.* **1999,** *147* (1), 410-420.

[62] Qiao, Y.; Wu, S. C.; Yi, J.; Sun, Y.; Guo, S. H.; Yang, S. X.; He, P.; Zhou, H. S., From O_2^- to HO_2^- : Reducing by-products and overpotential in Li-O_2 batteries by water addition. *Angew. Chem. Int. Ed.* **2017,** *56* (18), 4960-4964.

[63] Li, J. F.; Huang, Y. F.; Ding, Y.; Yang, Z. L.; Li, S. B.; Zhou, X. S.; Fan, F. R.; Zhang, W.; Zhou, Z. Y.; Wu, D. Y.; Ren, B.; Wang, Z. L.; Tian, Z. Q., Shell-isolated nanoparticle-enhanced Raman spectroscopy. *Nature* **2010,** *464* (7287), 392-395.

[64] Pearce, P. E.; Perez, A. J.; Rousse, G.; Saubanère, M.; Batuk, D.; Foix, D.; McCalla, E.; Abakumov, A. M.; Van Tendeloo, G.; Doublet, M.-L.; Tarascon, J.-M., Evidence for anionic redox activity in a tridimensional-ordered Li-rich positive electrode β-Li_2IrO_3. *Nat. Mater.* **2017,** *16* (5), 580-586.

[65] Qiu, B.; Zhang, M. H.; Xia, Y. G.; Liu, Z. P.; Meng, Y. S., Understanding and controlling anionic electrochemical activity in high-capacity oxides for next generation Li-ion batteries. *Chem. Mater.* **2017,** *29* (3), 908-915.

[66] Qiao, Y.; Ye, S., In situ study of oxygen reduction in dimethyl sulfoxide (DMSO) solution: A fundamental study for development of the lithium–oxygen battery. *J. Phys. Chem. C* **2015,** *119* (22), 12236-12250.

[67] Hy, S.; Felix, F.; Rick, J.; Su, W. N.; Hwang, B. J., Direct in situ observation of Li_2O evolution on Li-rich high-capacity cathode material, $Li[Ni_xLi_{(1-2x)/3}Mn_{(2-x)/3}]O_2$ ($0 \leq x \leq 0.5$). *J. Am. Chem. Soc.* **2014,** *136* (3), 999-1007.

[68] Lanz, P.; Villevieille, C.; Novak, P., Ex situ and in situ Raman microscopic investigation of the differences between stoichiometric $LiMO_2$ and high-energy $xLi_2MnO_3.(1-x)LiMO_2$ (M = Ni, Co, Mn). *Electrochim. Acta* **2014,** *130* (1), 206-212.

[69] Yabuuchi, N.; Yoshii, K.; Myung, S. T.; Nakai, I.; Komaba, S., Detailed studies of a high-capacity electrode material for rechargeable batteries, Li_2MnO_3-$LiCo_{1/3}Ni_{1/3}Mn_{1/3}O_2$. *J. Am. Chem. Soc.* **2011,** *133* (12), 4404-4419.

[70] Ohzuku, T.; Ueda, A.; Nagayama, M., Electrochemistry and structural chemistry of $LiNiO_2$ (R-3m) for 4 volt secondary lithium cells. *J. Electrochem. Soc.* **1993,** *140* (7), 1862-1870.

[71] Park, S. H.; Oh, S. W.; Kang, S. H.; Belharouak, I.; Amine, K.; Sun, Y. K., Comparative study of different crystallographic structure of $LiNi_{0.5}Mn_{1.5}O_4$-delta cathodes with wide operation voltage (2.0 - 5.0 V). *Electrochim. Acta* **2007,** *52* (25), 7226-7230.

[72] Yabuuchi, N.; Kubota, K.; Dahbi, M.; Komaba, S., Research development on sodium-ion batteries. *Chem. Rev.* **2014,** *114* (23), 11636-82.

[73] Guignard, M.; Didier, C.; Darriet, J.; Bordet, P.; Elkaïm, E.; Delmas, C., P2-Na_xVO_2 system as electrodes for batteries and electron-correlated materials. *Nat. Mater.* **2013,** *12* (1), 74-80.

[74] Bridgeman, A. J.; Rothery, J., Bonding in mixed halogen and hydrogen peroxides. *J. Chem. Soc. Dalton Trans.* **1999**, (22), 4077-4082.

[75] Liu, Z. X.; De Jesus, L. R.; Banerjee, S.; Mukherjee, P. P., Mechanistic evaluation of Li_xO_y formation on delta-MnO_2 in nonaqueous Li-air batteries. *ACS Appl. Mater. Interfaces* **2016,** *8* (35), 23028-23036.

[76] Saubanère, M.; McCalla, E.; Tarascon, J. M.; Doublet, M. L., The intriguing question of anionic redox in high-energy density cathodes for Li-ion batteries. *Energy Environ. Sci.* **2016,** *9* (3), 984-991.

[77] Foix, D.; Sathiya, M.; McCalla, E.; Tarascon, J. M.; Gonbeau, D., X-ray photoemission spectroscopy study of cationic and anionic redox processes in high-capacity Li-ion battery layered-oxide electrodes. *J. Phys. Chem. C* **2016,** *120* (2), 862-874.

[78] Jeanmaire, D. L.; Van Duyne, R. P., Surface raman spectroelectrochemistry: Part I. Heterocyclic, aromatic, and aliphatic amines adsorbed on the anodized silver electrode. *J. Electroanal. Chem. Interfacial Electrochem.* **1977,** *84* (1), 1-20.

[79] Lombardi, J. R.; Birke, R. L., A unified approach to surface-enhanced Raman spectroscopy. *J. Phys. Chem. C* **2008,** *112* (14), 5605-5617.

[80] Dupin, J. C.; Gonbeau, D.; Vinatier, P.; Levasseur, A., Systematic XPS studies of metal oxides, hydroxides and peroxides. *Phys. Chem. Chem. Phys.* **2000,** *2* (6), 1319-1324.

[81] Dahéron, L.; Dedryvere, R.; Martinez, H.; Ménétrier, M.; Denage, C.; Delmas, C.; Gonbeau, D., Electron transfer mechanisms upon lithium deintercalation from $LiCoO_2$ to CoO_2 investigated by XPS. *Chem. Mater.* **2007,** *20* (2), 583-590.

[82] Aurbach, D.; Weissman, I.; Schechter, A.; Cohen, H., X-ray photoelectron spectroscopy studies of lithium surfaces prepared in several important electrolyte solutions. A comparison with previous studies by Fourier transform infrared spectroscopy. *Langmuir* **1996,** *12* (16), 3991-4007.

[83] Twu, N.; Li, X.; Urban, A.; Balasubramanian, M.; Lee, J.; Liu, L.; Ceder, G., Designing new lithium-excess cathode materials from percolation theory: Nanohighways in $Li_xNi_{2-4x/3}Sb_{x/3}O_2$. *Nano Lett.* **2014,** *15* (1), 596-602.

[84] Chen, H. R.; Islam, M. S., Lithium extraction mechanism in Li-rich Li_2MnO_3 involving oxygen hole formation and dimerization. *Chem. Mater.* **2016,** *28* (18), 6656-6663.

[85] Blöchl, P. E., Projector augmented-wave method. *Phys. Rev. B* **1994,** *50* (24), 17953-17979.

[86] Kohn, W.; Sham, L. J., Self-consistent equations including exchange and correlation effects. *Phys. Rev.* **1965,** *140* (4A), A1133-A1138.

[87] Perdew, J. P.; Burke, K.; Ernzerhof, M., Generalized gradient approximation made simple. *Phys. Rev. Lett.* **1996,** *77* (18), 3865-3868.

[88] Monkhorst, H. J.; Pack, J. D., Special points for Brillouin-zone integrations. *Phys. Rev. B* **1976,** *13* (12), 5188-5192.

[89] Luo, K.; Roberts, M. R.; Guerrini, N.; Tapia-Ruiz, N.; Hao, R.; Massel, F.; Pickup, D. M.; Ramos, S.; Liu, Y. S.; Guo, J., Anion redox chemistry in the cobalt free 3d transition metal oxide intercalation electrode $Li[Li_{0.2}Ni_{0.2}Mn_{0.6}]O_2$. *J. Am. Chem. Soc* **2016,** *138* (35), 11211-11218.

[90] Gu, M.; Belharouak, I.; Genc, A.; Wang, Z.; Wang, D.; Amine, K.; Gao, F.; Zhou, G.; Thevuthasan, S.; Baer, D. R., Conflicting roles of nickel in controlling cathode performance in lithium ion batteries. *Nano Lett.* **2012,** *12* (10), 5186-5191.

[91] Thackeray, M. M.; Kang, S. H.; Johnson, C. S.; Vaughey, J. T.; Benedek, R.; Hackney, S., Li_2MnO_3-stabilized $LiMO_2$ (M = Mn, Ni, Co) electrodes for lithium-ion batteries. *J. Mater. Chem.* **2007,** *17* (30), 3112-3125.

[92] Roos, J.; Eames, C.; Wood, S. M.; Whiteside, A.; Saiful Islam, M., Unusual Mn coordination and redox chemistry in the high capacity borate cathode $Li_7Mn(BO_3)_3$. *Phys. Chem. Chem. Phys.* **2015,** *17* (34), 22259-22265.

[93] Armand, M.; Tarascon, J. M., Building better batteries. *Nature* **2008,** *451* (7179), 652-657.

[94] Li, M.; Lu, J.; Chen, Z.; Amine, K., 30 years of lithium-ion batteries. *Adv. Mater.* **2018,** *30* (33), 1800561.

[95] Ohzuku, T.; Ueda, A.; Nagayama, M.; Iwakoshi, Y.; Komori, H., Comparative study of $LiCoO_2$, $LiNi_{1/2}Co_{1/2}O_2$ and $LiNiO_2$ for 4 volt secondary lithium cells. *Electrochim. Acta* **1993,** *38* (9), 1159-1167.

[96] Li, B.; Xia, D., Anionic redox in rechargeable lithium batteries. *Adv. Mater.* **2017,** *29* (48), 1701054.

[97] Rossouw, M.; Thackeray, M., Lithium manganese oxides from Li_2MnO_3 for rechargeable lithium battery applications. *Mater. Res. Bull.* **1991,** *26* (6), 463-473.

[98] Amalraj, S. F.; Burlaka, L.; Julien, C. M.; Mauger, A.; Kovacheva, D.; Talianker, M.; Markovsky, B.; Aurbach, D., Phase transitions in Li_2MnO_3 electrodes at various states-of-charge. *Electrochim. Acta* **2014,** *123*, 395-404.

[99] Shimoda, K.; Oishi, M.; Matsunaga, T.; Murakami, M.; Yamanaka, K.; Arai, H.; Ukyo, Y.; Uchimoto, Y.; Ohta, T.; Matsubara, E.; Ogumi, Z., Direct observation of layered-to-spinel phase transformation in Li_2MnO_3 and the spinel structure stabilised after the activation process. *J. Mater. Chem. A* **2017,** *5* (14), 6695-6707.

[100] Yu, H.; Zhou, H., High-energy cathode materials (Li_2MnO_3–$LiMO_2$) for lithium-ion batteries. *J. Phys. Chem. Lett.* **2013,** *4* (8), 1268-1280.

[101] Xiao, Z.; Meng, J.; Li, Q.; Wang, X.; Huang, M.; Liu, Z.; Han, C.; Mai, L., Novel MOF shell-derived surface modification of Li-rich layered oxide cathode for enhanced lithium storage. *Sci. Bull.* **2018,** *63* (1), 46-53.

[102] Zuo, Y.; Li, B.; Jiang, N.; Chu, W.; Zhang, H.; Zou, R.; Xia, D., A high-capacity O2-type Li-rich cathode material with a single-layer Li_2MnO_3 superstructure. *Adv. Mater.* **2018,** *30* (16), 1707255.

[103] Wang, Y.; Yang, Z.; Qian, Y.; Gu, L.; Zhou, H., New insights into improving rate performance of lithium-rich cathode material. *Adv. Mater.* **2015,** *27* (26), 3915-3920.

[104] Zhang, X. D.; Shi, J. L.; Liang, J. Y.; Yin, Y. X.; Zhang, J. N.; Yu, X. Q.; Guo, Y. G., Suppressing surface lattice oxygen release of Li-rich cathode materials via heterostructured spinel $Li_4Mn_5O_{12}$ coating. *Adv. Mater.* **2018,** *30* (29), 1801751.

[105] Sun, Y. K.; Lee, M. J.; Yoon, C. S.; Hassoun, J.; Amine, K.; Scrosati, B., The role of AlF_3 coatings in improving electrochemical cycling of Li-enriched nickel-manganese oxide electrodes for Li-ion batteries. *Adv. Mater.* **2012,** *24* (9), 1192-1196.

[106] Li, X.; Qiao, Y.; Guo, S.; Xu, Z.; Zhu, H.; Zhang, X.; Yuan, Y.; He, P.; Ishida, M.; Zhou, H., Direct visualization of the reversible O^{2-}/O^{-} redox process in Li-rich cathode materials. *Adv. Mater.* **2018,** *30* (14), 1705197.

[107] Song, B.; Liu, Z.; Lai, M. O.; Lu, L., Structural evolution and the capacity fade mechanism upon long-term cycling in Li-rich cathode material. *Phys. Chem. Chem. Phys.* **2012,** *14* (37), 12875-12883.

[108] Lee, J.; Urban, A.; Li, X.; Su, D.; Hautier, G.; Ceder, G., Unlocking the potential of cation-disordered oxides for rechargeable lithium batteries. *Science* **2014,** *343* (6170), 519-522.

[109] Yabuuchi, N.; Takeuchi, M.; Nakayama, M.; Shiiba, H.; Ogawa, M.; Nakayama, K.; Ohta, T.; Endo, D.; Ozaki, T.; Inamasu, T., High-capacity electrode materials for rechargeable lithium batteries: Li_3NbO_4-based system with cation-disordered rocksalt structure. *Proc. Natl. Acad. Sci.* **2015,** *112* (25), 7650-7655.

[110] Nakajima, M.; Yabuuchi, N., Lithium-excess cation-disordered rocksalt-type oxide with nanoscale phase segregation: $Li_{1.25}Nb_{0.25}V_{0.5}O_2$. *Chem. Mater.* **2017,** *29* (16), 6927-6935.

[111] Kan, W. H.; Chen, D.; Papp, J. K.; Shukla, A. K.; Huq, A.; Brown, C. M.; McCloskey, B. D.; Chen, G., Unravelling solid-state redox chemistry in $Li_{1.3}Nb_{0.3}Mn_{0.4}O_2$ single-crystal cathode material. *Chem. Mater.* **2018,** *30* (5), 1655-1666.

[112] Lee, J.; Kitchaev, D. A.; Kwon, D. H.; Lee, C. W.; Papp, J. K.; Liu, Y. S.; Lun, Z.; Clément, R. J.; Shi, T.; McCloskey, B. D., Reversible Mn^{2+}/Mn^{4+} double redox in lithium-excess cathode materials. *Nature* **2018,** *556* (7700), 185-190.

[113] Kitchaev, D. A.; Lun, Z.; Richards, W. D.; Ji, H.; Clément, R. J.; Balasubramanian, M.; Kwon, D. H.; Dai, K.; Papp, J. K.; Lei, T., Design principles for high transition metal capacity in disordered rocksalt Li-ion cathodes. *Energy Environ. Sci.* **2018,** *11* (8), 2159-2171.

[114] Zhao, E.; He, L.; Wang, B.; Li, X.; Zhang, J.; Wu, Y.; Chen, J.; Zhang, S.; Liang, T.; Chen, Y., Structural and mechanistic revelations on high capacity cation-disordered Li-rich oxides for rechargeable Li-ion batteries. *Energy Storage Mater.* **2019,** *16*, 354-363.

[115] Shirane, T.; Kanno, R.; Kawamoto, Y.; Takeda, Y.; Takano, M.; Kamiyama, T.; Izumi, F., Structure and physical properties of lithium iron oxide, $LiFeO_2$, synthesized by ionic exchange reaction. *Solid State Ionics* **1995,** *79*, 227-233.

[116] Thackeray, M.; Johnson, P.; De Picciotto, L.; Bruce, P.; Goodenough, J., Electrochemical extraction of lithium from $LiMn_2O_4$. *Mater. Res. Bull.* **1984,** *19* (2), 179-187.

[117] Yi, T. F.; Li, Y. M.; Li, X. Y.; Pan, J. J.; Zhang, Q.; Zhu, Y. R., Enhanced electrochemical property of $FePO_4$-coated $LiNi_{0.5}Mn_{1.5}O_4$ as cathode materials for Li-ion battery. *Sci. Bull.* **2017,** *62* (14), 1004-1010.

[118] Hohenberg, P.; Kohn, W., Inhomogeneous electron gas. *Phys. Rev.* **1964,** *136* (3B), B864-B871.

[119] Jain, A.; Hautier, G.; Ong, S. P.; Moore, C. J.; Fischer, C. C.; Persson, K. A.; Ceder, G., Formation enthalpies by mixing GGA and GGA+ U calculations. *Phys. Rev. B* **2011,** *84* (4), 045115(1-10).

[120] Wang, L.; Maxisch, T.; Ceder, G., Oxidation energies of transition metal oxides within the GGA+ U framework. *Phys. Rev. B* **2006,** *73* (19), 195107(1-6).

[121] Zhang, X.; Luo, D.; Li, G.; Zheng, J.; Yu, C.; Guan, X.; Fu, C.; Huang, X.; Li, L., Self-adjusted oxygen-partial-pressure approach to the improved electrochemical performance of electrode $Li[Li_{0.14}Mn_{0.47}Ni_{0.25}Co_{0.14}]O_2$ for lithium-ion batteries. *J. Mater. Chem. A* **2013,** *1* (34), 9721-9729.

[122] Shi, J. L.; Zhang, J. N.; He, M.; Zhang, X. D.; Yin, Y. X.; Li, H.; Guo, Y. G.; Gu, L.; Wan, L. J., Mitigating voltage decay of Li-rich cathode material via increasing Ni content for lithium-ion batteries. *ACS Appl. Mater. Interfaces* **2016,** *8* (31), 20138-20146.

[123] Qiao, Y.; Guo, S.; Zhu, K.; Liu, P.; Li, X.; Jiang, K.; Sun, C. J.; Chen, M.; Zhou, H., Reversible anionic redox activity in Na_3RuO_4 cathodes: a prototype Na-rich layered oxide. *Energy Environ. Sci.* **2018,** *11* (2), 299-305.

[124] Yang, Y.; Liu, X.; Dai, Z.; Yuan, F.; Bando, Y.; Golberg, D.; Wang, X., In situ electrochemistry of rechargeable battery materials: status report and perspectives. *Adv. Mater.* **2017,** *29* (31), 1606922.

[125] Shaju, K.; Rao, G. S.; Chowdari, B., Li ion kinetic studies on spinel cathodes, $Li(M_{1/6}Mn_{11/6})O_4$ (M = Mn, Co, CoAl) by GITT and EIS. *J. Mater. Chem.* **2003,** *13* (1), 106-113.

[126] Cambaz, M. A.; Vinayan, B. P.; Euchner, H.; Johnsen, R. E.; Guda, A. A.; Mazilkin, A.; Rusalev, Y. V.; Trigub, A. L.; Gross, A.; Fichtner, M., Design of Nickel-based cation-disordered rock-salt oxides: The effect of transition metal (M = V, Ti, Zr) substitution in $LiNi_{0.5}M_{0.5}O_2$ binary systems. *ACS Appl. Mater. Interfaces* **2018,** *10* (26), 21957-21964.

[127] Li, Z.; Du, F.; Bie, X.; Zhang, D.; Cai, Y.; Cui, X.; Wang, C.; Chen, G.; Wei, Y., Electrochemical Kinetics of the $Li[Li_{0.23}Co_{0.3}Mn_{0.47}]O_2$ Cathode Material Studied by GITT and EIS. *J. Phys. Chem. C* **2010,** *114* (51), 22751-22757.

[128] Lin, J.; Mu, D.; Jin, Y.; Wu, B.; Ma, Y.; Wu, F., Li-rich layered composite $Li[Li_{0.2}Ni_{0.2}Mn_{0.6}]O_2$ synthesized by a novel approach as cathode material for lithium ion battery. *J. Power Sources* **2013,** *230* (15), 76-80.

[129] Tang, S. B.; Lai, M. O.; Lu, L., Study on Li^+-ion diffusion in nano-crystalline $LiMn_2O_4$ thin film cathode grown by pulsed laser deposition using CV, EIS and PITT techniques. *Mater. Chem. Phys.* **2008,** *111* (1), 149-153.

[130] Rong, X.; Liu, J.; Hu, E.; Liu, Y.; Wang, Y.; Wu, J.; Yu, X.; Page, K.; Hu, Y. S.; Yang, W., Structure-induced reversible anionic redox activity in Na layered oxide cathode. *Joule* **2018,** *2* (1), 125-140.

[131] Maitra, U.; House, R. A.; Somerville, J. W.; Tapia-Ruiz, N.; Lozano, J. G.; Guerrini, N.; Hao, R.; Luo, K.; Jin, L.; Pérez-Osorio, M. A., Oxygen redox chemistry without excess alkali-metal ions in $Na_{2/3}[Mg_{0.28}Mn_{0.72}]O_2$. *Nat. Chem.* **2018,** *10* (3), 288-295.